University of Stavanger

Faculty of Science and Technology

MASTER'S THESIS

Study program/Specialization:	Spring semester, 2021
Engineering Structures & Materials / Civil Engineering Structures	Open

Writer: Simen Mundal Dyrkolbotn	*Simen Dyrkolbotn*
	(Writer's signature)

Faculty supervisor:
Yanyan Sha

Thesis title:
Shipping Container Impact with Bridge Girders

Credits (ECTS): 30

Key words:	Pages:79
Collision analysis Bjørnafjorden Floating Bridge FE-Modelling Local and Global analysis LS-DYNA Orcaflex	+ enclosure:18
	Stavanger, 15th June/2021 Date/year

Abstract

Aluminium bridge decks have been proposed as alternatives to traditional steel bridge decks. These girders can meet all design criteria for bridges and have the advantages of low density and high corrosion resistance. Regardless of girder material, one critical issue in bridge design is to ensure the safety of bridge girders under accidental ship collisions. Such collision accidents can occur in earthquake or tsunami inundation, due to ship maneuvering errors or mechanical failures. The bridge girder strength against ship collision load should be carefully checked to avoid large local damage in the impacted region and further degradation of global bridge safety. Some studies have been conducted for ship deckhouse and forecastle impacts with bridge girders. However, bridge decks are also under the impact of stacked shipping containers from cargo ships. Considering the lower elastic modulus and ductility of aluminium material compared with steel, aluminium bridge girders may be more vulnerable to collision loads.

The thesis work is divided into two parts. The first aims to numerically investigate the local structural response of bridge girders under shipping container impacts for steel and aluminium girders. FE- Models of a bridge section and a 20 ft standard shipping container are developed in LS-DYNA. The strain rate effect of the aluminium girder is investigated. The impact force, structural damage, and energy dissipation during the collision are compared for both materials. The effects of impact angle and vertical location are also discussed. The second part of the work aims to numerically investigate the global response of the bridge by using the obtained force-displacement relationship from the shipping container impact. A global model has been built in Orcaflex. Eigenmodes, moments about the strong and weak axis as well as bridge motions have been discussed. The conclusions from the local analysis (published as an article) were that strain rate had a minor effect on the investigated aluminium alloy. In addition, a significant reduction of contact force was observed for the aluminium girder due to local fracture leading to larger dissipation of strain energy. For some head-on collision scenarios, the girder material seemingly plays a lesser role as long as the stiffness is sufficient to redistribute the impact force over a larger area. The majority of energy dissipation was observed in the shipping containers. For the global analysis, there was significant development of strong axis bending moment and the dynamic displacement was less than expected. The period of the motions post-impact was close to one of the eigen-periods. It should be stated that the modal analysis did not correlate satisfactorily with the NPRA's existing reports, which would question the validity of results in this part.

Preface and Acknowledgements

This thesis marks the final work of the master program Engineering Structures and Materials with specialization in Civil Engineering Structures at the University of Stavanger. The work was conducted spring of 2021. The scope of work includes building and modifying two Finite Element Models, firstly a local model in LS-DYNA with shipping container impacts on bridge girders in steel and aluminium. A scientific article has been written and published from this part of the work and is included in the appendix. Secondly, a global analysis in Orcaflex assessing the global response due to several shipping containers impacting the floating bridge is conducted. In addition, familiarization with floating bridge concepts and bridge construction is done.

Guidance and supervision have been provided by Professor Yanyan Sha at UiS. I would like to thank my supervisor for his guidance, flexibility, and dedication to my work and the field. I am also grateful for the opportunity and collaboration in writing and publishing the article Response of aluminium bridge girders subjected to shipping container impacts for the Marstruct 8th International Conference on Marine Structures in Trondheim. Unfortunately, due to the Covid-19 pandemic, the conference was held digitally and Trondheim could not be visited. Initial knowledge in LS-DYNA or Orcaflex was nonexistent. A complex and large task, but also very interesting to work and learn about. I have gained a lot of knowledge in FE-modelling and bridge engineering and I am grateful for the opportunity to work on the topic.

Additional gratitude is directed to my girlfriend, Anna, who supported and motivated me unconditionally in these difficult times.

Contents

Abbreviations

NPRA	**N**orwegian Public Road Administration (Statens Vegvesen)
NTP	**N**ational Transportation Plan
TLP	**T**ension Leg Platform
FE	**F**inite Element
FEM	**F**inite Element Method
FEA	**F**inite Element Analysis
SFT	**S**ubmerged Floating Tunnels
DOF	**D**egree Off Freedom
w.r.t.	**w**ith respect too
ALS	**A**ccident Llimit State
ULS	**U**ltimate Llimit State
CEMT	**C**onference of European Ministers of Ttransport
DIF	**D**ynamic Increase Factor or strain-rate scaling effect
HAZ	**H**eat Affected Zone (w.r.t. welding)

Symbols

symbol	name	unit
Δt	Time step in numerical modelling	s
α	Coefficient for rayleigh damping	
β	Coefficient for rayleigh damping	
ω	Natural frequency	rads^{-1}
ξ	Damping ratio	
ρ	Density	kg/m^3
E	Modulus of Elasticity	GPa
ν	Poisson's Ratio	
σ	Stress	N/mm^2
ϵ	Strain	

Chapter 1

Introduction

The investigated bridge is planned to be built on E39, across Bjørnafjorden. In the following chapter, there is an introduction to the Ferry free E39 project, different concepts for floating bridges as well as the objective and problem statement of the thesis.

1.1 Ferry Free E39

The European road E39, stretching from Trondheim in the north to Kristiansand in the south, with a distance of 1100 km and 21 hours traveling time connects the cities of western Norway. It passes through Stavanger, Bergen, Ålesund, and Molde [1], and does today consist of 7 ferry connections, shown in Figure 1.1 The NPRA is set to improve this coastal highway, guided by the NTP (Nasjonal transportplan) issued in 2017 for 2018–2029. The overlying objective is to produce a ferry-free E39, reducing the travel time to 11 hours. This will be done by substituting ferries with underwater tunnels and bridges as well as upgrading the existing road. The goal for the stretch is also to tie together business regions, housing, and labor markets, and provide better conditions for Norway's largest export market.

In order to succeed, the development of new technology and more knowledge is required, especially related to crossing the deepest fjords and taking coastal weather conditions into account. Technological breakthroughs are expected, and offshore methods are being investigated to determine the feasibility of floating bridge and tunnel proposals, as well as to measure currents, wind and waves [2]. The findings and results are also expected to be valuable knowledge that is in demand throughout the world.

Environmental impact

The NPRA [2] expects increased traffic as the road standard improves, but emissions over a 40-year perspective are estimated to be the same as today, assuming the same vehicle park as of 2018. Reasons being the removal of ferries, steady speed, and low incline. However, these conditions are in constant change, and electric, bio-, and hydrogen-powered vehicles are likely to impact the estimated environmental impact.

Figure 1.1: Overview of E39 [2]

Cost of the project

The finished total upgraded ferry-free E39 is estimated to cost 340 billion NOK and the potential for road toll is set to 110 billion NOK. In this thesis, an end-anchored floating bridge is considered, which is considered possible on 3 different fjord crossings, Halsafjorden, Vartdalsfjorden, and Bjørnafjorden, according to NPRA [2] and is the chosen solution for the Bjørnafjord crossing.

Crossing the Bjørnafjord is one of the most challenging projects. The floating bridge will be five kilometers long, deeming the longest floating bridge in the world [3]. The investigation of possible design methods begun in 2009 and submerged floating bridge, cable-stayed bridge with TLP foundations and the mentioned floating bridge have all been proposed and investigated. The floating bridge was chosen with respect to safety

and cost. [3]. The design consists of a ship fairway with a free height of 45 meters at the south end, provided by a cable-stayed bridge with a span of 400 meters, the bridge then continues to stretch over floating pontoons with approximately 125-meter spacing shown in Figure 1.2. This will be described in further detail in Chapter 3.

Figure 1.2: Bjørnafjorden Crossing [2]

In 2019 NPRA appointed several consulting companies to further investigate the current designs in order to further pinpoint the final design. It is beneficial to reduce the weight, and different materials such as aluminium will be investigated. Previously, extensive studies on collision with bridge substructures like pylons, piers, and pontoons have been performed. Unfortunately, impact with bridge superstructures has not been well studied, and recently, an aluminum bridge girder concept was proposed. The impact capacity and response should be carefully evaluated and is the background of this thesis project.

1.2 Floating bridges

This subchapter will focus on familiarization with the floating bridge concept and different kinds of floating bridges related to the project. Various large floating structures have been constructed in the past decades. This includes floating airports, pontoon bridges, and floating oil platforms as well as other structures. However, behavior of large and long-spanned bridges like on Bjørnafjorden has until now only been researched and not constructed yet. The current longest floating bridge in the world is the Evergreen Point floating bridge in Seattle USA [4], with a length of 2350 meters, which is around half the length of the Bjørnafjord crossing of five kilometers [3]. During the past years NPRA has funded research among UiS, NTNU, and Chalmers Universe of Technology [2], in order to obtain the required knowledge to execute these projects.

Floating bridges are generally used when the spans are too long for cable-stayed bridges, deep waters, and when geotechnical conditions in the seabed are unsatisfactory.

1.2.1 Pontoon Bridge

Pontoon bridges are generally constructed using floating concrete pontoons to support the bridge deck, that is anchored to the ground [5]. Pontoon bridges are the most common type of floating bridges and Bjørnafjorden crossing is a part cable-stayed and part pontoon bridge, referring Figure 1.2

Pontoons are subjected to various loading, including hydrostatic and hydrodynamic forces[6] :

- Permanent loads

- Traffic and environmental load

- Thrust due to heave and roll

- Drag force due to currents

- Anchor reactions

- Buoyancy

Pontoons can be installed in protected sea states such as fjords, rivers, or behinds breakwaters to protect from large waves and swells. The mooring lines comprise chains or ropes and sinkers, anchors, and tethering to anchor them [5].

1.2.2 TLP-supported Floating Bridge

The TLP-supported floating bridges stem from semi-submersible floating offshore platforms and more specifically the tension leg platforms. They consist of large columns or watertight ballast compartments that are partly submerged in water. This compensates for large wavelengths and heights compared to pontoons. Similar to a pontoon, the TLP has a positive net buoyancy such that the tethers anchoring it to the seabed are tensioned. The cables are dimensioned to withstand longitudinal and transverse forces. The TLP concept allows for a reduction in the number of pontoons as towers can be placed on the foundation, making the superstructure a cable-stayed bridge. The TLP-supported bridge has previously been proposed for the Bjørnafjorden crossing, and Figure 1.3 shows the proposed construction.


Figure 1.3: TLP-supported floating bridge on the Bjørnafjord crossing

Floating suspension bridges represent new challenges when it comes to prediction of the dynamic behavior. There is a complex interaction between the moorings and the floating towers, and the towers and the bridge deck. Hydrodynamic and aerodynamic modeling is a crucial issue [7].

1.2.3 Submerged Floating Tunnels (SFT)

Submerged floating tunnels are an innovative way of crossing when water is too deep or there is solid rock causing excavation difficulties. It also allows for free water traffic above the tunnel, and because it is completely submerged, it is largely protected from environmental loads. SFT's are also referred to as Archimedes Bridge and is in essence a buoyant tunnel that floats at a certain water depth [8]. A submerged floating tunnel has not been built yet and there are challenges related to operations and installation.
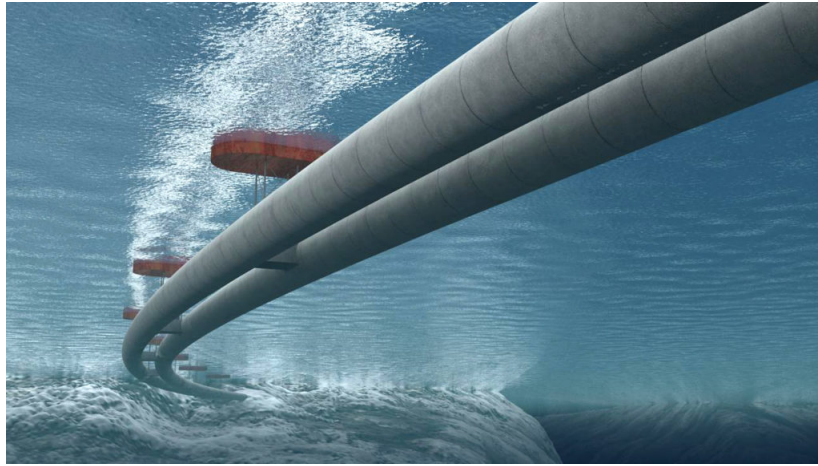
Figure 1.4: SFT proposed on E39 [9]

SFT's can either be supported by floating pontoons, or they can be anchored to the seabed, similarly to the TLP-foundations, the two types are shown in figure 1.5 below.
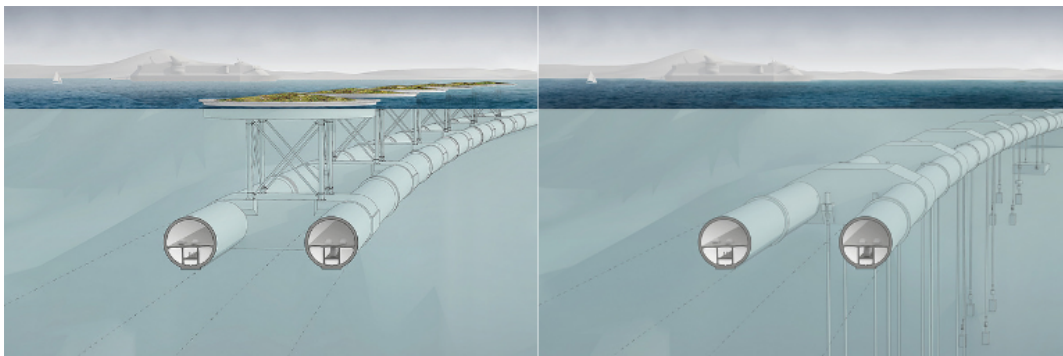

Figure 1.5: Cross-section of SFT with pontoons (leftmost picture) and vertical tethers (rightmost picture) [8]

1.3   Objective and Motivation

The objective of the thesis is to be able to build and modify an FE-model in LS-DYNA and Orcaflex and simulate an impact where a shipping container collides into the bridge deck at various scenarios. The principle is shown in figure 1.6. Then impact response and capacity between a steel and aluminium bridge girder will be reviewed. The goal is to obtain a force-displacement relationship from the local analysis and apply this relationship to the global model. Several impact scenarios are considered, with different angles and vertical positions. Two models are used in the analysis. First, one detailed LS-DYNA local FE-model analyzing the local damage and energy absorption of the cross-section of the bridge girder. This is mentioned carried out in LS-DYNA as a non-linear analysis. Second, a global Orcaflex FE-model to assess impact response for the entire bridge carried out as a linear analysis.

The thesis is organized in 6 chapters in the following manner:

- Chapter 1: Introduction to the project

- Chapter 2: Literature review and methodology

- Chapter 3: Bridge parameters and materials

- Chapter 4: FEM-Model setup

- Chapter 5: Analysis Results

- Chapter 6: Discussions and Conclusions
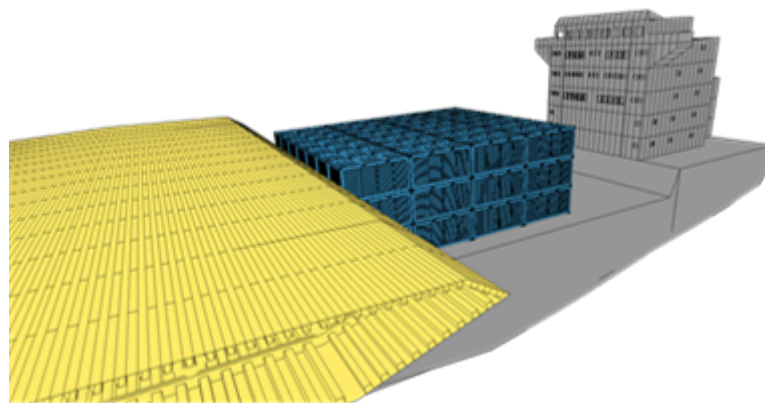
Figure 1.6: Shipping container impact with bridge girder

The motivation of the study is being able to participate in the research of finding the most beneficial way of constructing long floating bridges and contribute to reducing costs

while maintaining safety, which is important in large infrastructure projects. This can also be considered contributing to the innovation and development of new technology and knowledge, which is the reason NPRA is collaborating with academic institutions and other consulting firms on the E39 project. The Bjørnafjorden floating bridge will be the first of its kind with respect to scale when constructed.

1.4   Problem Statement

Compare impact response and capacity of a steel and aluminium bridge girder, at various collision scenarios by building and modifying an FE-model in LS-DYNA and Orcaflex. In addition, become familiar with floating bridge design. The analysis will comprise of two tasks, firstly assessment of the local damage consisting of a detailed non-linear finite element model. Secondly, the global response analysis by building a global FE-model from scratch and using dynamic time domain analysis in Orcaflex to assess global deformation, forces, and moments due to collision. A summary of the results, discussion, and conclusion on the further recommendation will follow. The various collision scenarios involve investigation on the effect of impact height and direction. Relevant theory as a background for the analysis is also included.

1.5   Limitations

- Simulations are limited to ALS and does not take into account traffic loads or environmental loads.

- Global analysis of shipping container impact conducted as linear analysis.

- Abutments and their geometry has not been considered.

- Strength reducing phenomenons such as reduction of strength in Heat Affected Zones (HAZ) where welding is relevant has not been considered.

Chapter 2

Literature Review and Methodology

2.1 Literature Review

In the past years, numbers of impact accidents due to over-height ship superstructures and cargos have been reported. Several studies have been performed on ship superstructure and shipping container collision with steel and reinforced concrete bridge decks and piers with LS-DYNA non-linear FE-package. Many by Sha and Amdahl [10], [11], [12] also Guo et al. [13] and Li et al. [14] have investigated impact on bridge piers. Verification of obtained results from impact loading is commonly sought by performing impact testing on plates and stiffened panels. Jung et al. [15], Kim et al. [16], Alsos et al. [17] have performed experimental testing with various steel plates and compared response in LS-DYNA and concluded that the non-linear behaviour in the software matches closely the experimental values, given adequate modeling. Moreover, several studies on high-speed ballistic impact on steel plates with LS-DYNA has also been performed. Deb et al. [18] as well as Dey et al. [19] found that with proper choice of contact algorithms, element size, and strain-rate dependant material properties, computed projectile impacts in LS-DYNA match closely test-based impacts. From these articles, it is evident that LS-DYNA is properly verified to have realistic results during analysis with steel materials, given that the modeling is done properly.

Similar experiments have also been conducted in order to verify the behavior of aluminium plates in LS-DYNA. Liu et al. [20], Villavicencio et al [21], Mohotti et al. [22] investigated the response of stiffened aluminium plates subjected to rigid indenter impacts. The conclusion was that the chosen material model could accurately predict the response of deflections, forces, and absorbed energies. It also deems that aluminum plates usually are insensitive to strain rate effects, and thereby the scale of the yield stress can be omitted in the material definition [20]. Liu et al. [20] also conducted similar experiments

9

on aluminum plates, in this study the automatic surface to surface contact definition deems satisfactory accuracy as well as the material model mentioned above. In both experiments, fine mesh in the area of impact is especially important in order to obtain accurate results.

2.2 Methodology

2.2.1 Finite Element Method

FEM is used for numerical simulations of field problems. Mathematically, field problems are described by differential equations or integral expressions in matrix form. Individual finite elements can be visualized as small pieces of a structure. The word "finite" distinguishes these pieces from infinitesimal elements used in calculus. Each element has a field quantity with simple spatial variation in form of polynomials. Definition of elements is usually described by their degree of freedom (DOF), which will define the degree of the polynomials. With increasing DOF, the field quantity polynomial will increase, increasing the accuracy. Increasing DOF and number of elements are referred to as discretization of the finite element mesh, and to obtain an economically computational model, correct discretization must be sought. There are examples where too discretized or non-discretized models converge or diverge to the wrong solution. Finite element (FE) formulations, in ready-to-use form, are contained in general-purpose FEA programs. It is possible to use FEA programs while having little knowledge of the analysis method or the problem to which it is applied, inviting consequences that may range from embarrassing to disastrous [23]. FEA and FEM can be summarized with the following:

- FEA has advantages over most other numerical analysis methods, including versatility and physical appeal.

- There is no geometric restriction. The body or region analyzed may have any shape.

- Boundary conditions and loading are not restricted. For example, in stress analysis, any portion of a body may be supported, while distributed or concentrated forces may be applied to any other portion.

- Material properties are not restricted to isotropy and may change from one element to another or even within an element.

- Components that have different behaviors, and different mathematical descriptions, can be combined: Thus a single FE model might contain bar, beam, plate, cable, and friction elements.

- An FE structure closely resembles the actual body or region to be analyzed.

- The approximation is easily improved by grading the mesh so that more elements appear where field gradients are high and more resolution is required.

2.2.2 A Finite Element System

A FEM system consists of several elements connected at nodes. Each node has DOF depending on the element type. The arrangement of elements and nodes is called the FE mesh and is defined by a set of equations in matrix form, where the unknown is the displacement or temperature at the nodal degrees of freedom. The system is generally defined by a global stiffness matrix, nodal displacement, and the vector of external loads.

$$[k][D] = [R] \tag{2.1}$$

2.2.3 Non-Linear Finite Element Analysis

From Cook et al.[23], computer power and FEA allows accounting for non-linear behavior in problems. This admits a variety of phenomena that can interact with each other. Fortunately, linear models provide satisfactory approximations for many problems of practical interest. However, a substantial departure from linearity is common, for example, material may yield or creep; local buckling may arise; gaps may open or close. Nonlinear problems pose the difficulty of describing phenomena by realistic mathematical and numerical models and the difficulty of solving nonlinear equations. In structural mechanics, non-linearity include the following:

- Material non-linearity. Material properties like elasticity, plasticity and creep changes with stress and strain.

- Contact non-linearity. Contact areas and thus contact forces are allowed to change, or there is frictional forces.

- Geometric non-linearity. Deformation is large enough that equilibrium equations must be written w.r.t. the deformed geometry. This includes that load directions will change as well.

In application of non-linear theory, the assumption of a constant stiffness matrix as proposed in equation 2.1 is no longer valid. Stiffness, and perhaps loads become functions of displacement or deformation. Then, [K] and [R] become functions of [D]. [D] can't be

directly solved because information about [K] and [R] is unknown. An iterative process is required to obtain [D] and it's associated [K] and [R] such that the product [K][D] is in equilibrium with [R] at the current time step. Types of non-linearity models are usually documented in software documentation for the relevant FE software.

2.2.4 Plasticity theory in FEA

Plasticity is shortly described as deformation that does not recover after load removal, involving stress above the yield stress of the material. The plastic strain consists of one recoverable elastic part and one non-recoverable plastic part. When yielding occurs, load, deformation and stress are both non-linearly related and history-dependant. This means that the load history is directly related to the final results. For an arbitrary load history, the final state of stress and deformation can be determined only by accounting for the history of stress and strain. In calculation, history is taken into account by formulations that relate increments of stress to increments of strain [23]. Plasticity also involves strain-hardening, which involves hardening of the material due to movement and generation of dislocations in the crystal lattice. This will increase the yield stress of the material for the next load cycle, but compromises ductility.

When modelling plasticity, isotropic or kinematic hardening is the most common hardening rules.
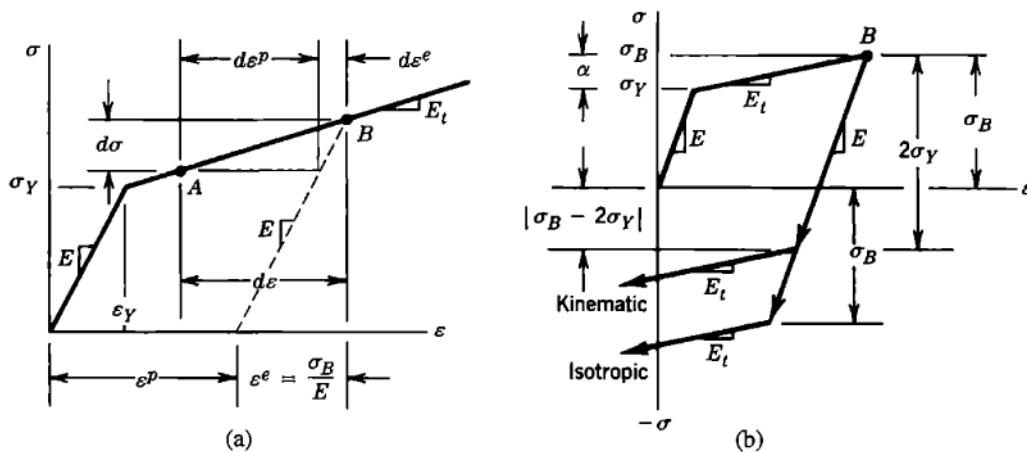
Figure 2.1: Kinematic and isotropic hardening rules [23] a) Stress-strain relation for uniaxial stress, idealized as bilinear (two straight lines), where uy is the stress at first onset of yielding. b) Isotropic and kinematic hardening rules.

Isotropic Hardening

Isotropic hardening involves that the yield surface remains the same shape but expands with increasing stress [24]. Upon reaching uniaxial stress σ_B in the plastic range in figure 2.1, according to the isotropic hardening rule, the elastic range has expanded from the initial value $2\sigma_y$ to the value $2\sigma_B$ ·

Kinematic Hardening

Kinematic hardening involves that the yield surface remains the same shape and size but translates in space. Then yield surface is shifted through space, utilizing a so-called back-space tensor. The kinematic hardening rule accounts for the Bauschinger effect by preserving an elastic range of $2\sigma_y$ if we look at figure 2.1, but ignores the possibility that the elastic range might increase. In practice, the two rules may be used in combination [23].

2.2.5 Element types

In this section, the element types utilized in the FEA will be defined.

Beam elements

Euler Bernoulli beam elements are commonly used. These beam elements do not allow for transverse shear deformation and plane sections remain plane and normal to the beam axis. A 3D-oriented beam element generally has 6 DOF's at the end nodes, as illustrated in figure 2.2. These beam elements are commonly modeled for slender beams. Interpolation is done using cubic interpolation functions, which allow for accurate results for distributed loading. Therefore they are well suited for dynamic vibration studies. In dynamic vibration studies, the inertia forces cause distributed loading [23].

Timoschenko beam elements are also commonly used, these allow for transverse shear deformations and are applicable for both thick and slender beams. They are interpolated with linear functions and require less computational power. They may be subjected to large axial strains, and caution must be exerted when applied in torsion. This is because torsional strains only are applicable when axial strains are not high [23].
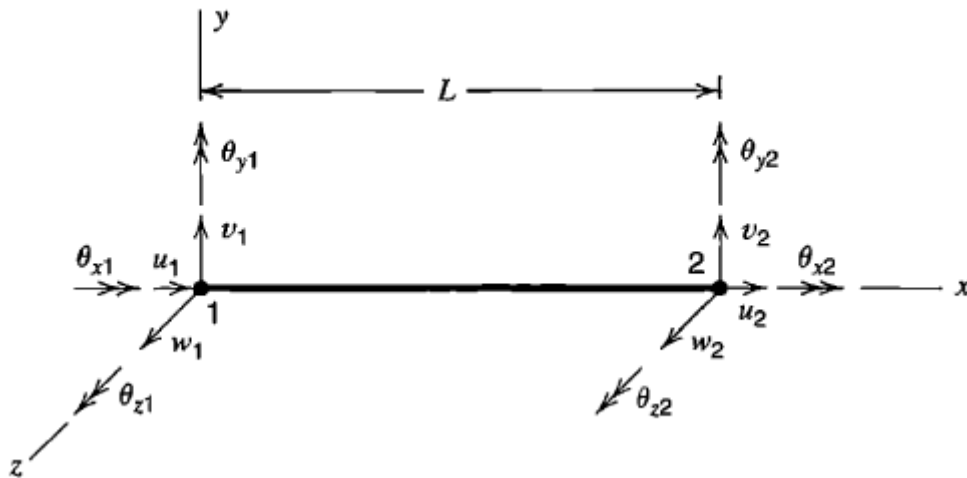
Figure 2.2: Euler Bernoulli beam element [23]

Beam elements in LS-DYNA is shown in figure 2.3 and has 11-66 active degrees of freedom at node 1 and node 2 in the local system. This might be to account for additional conditions, that can be accounted for during modelling. This could for example be warping conditions, as well as transverse shear. They are based on the Hughes-Liu beam formulation, allowing for transverse shear strain. In addition to this, a third node is introduced, that serves as a reference node indicating the initial orientation of the cross section in the local system [25].
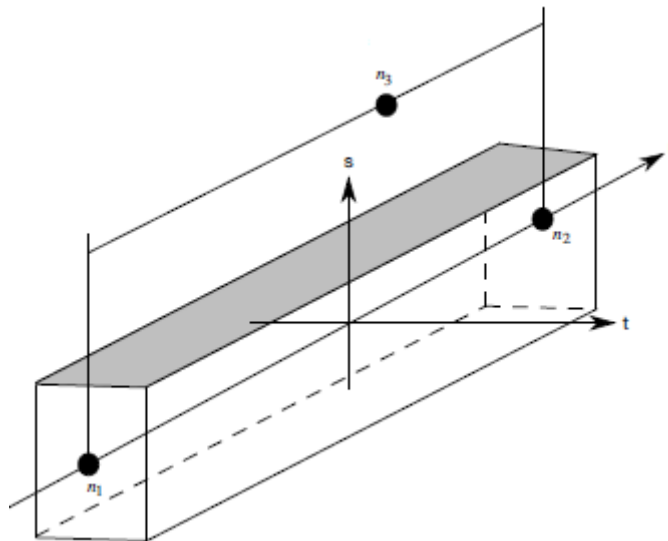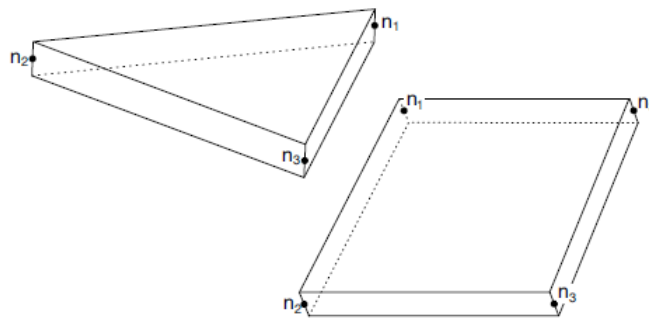

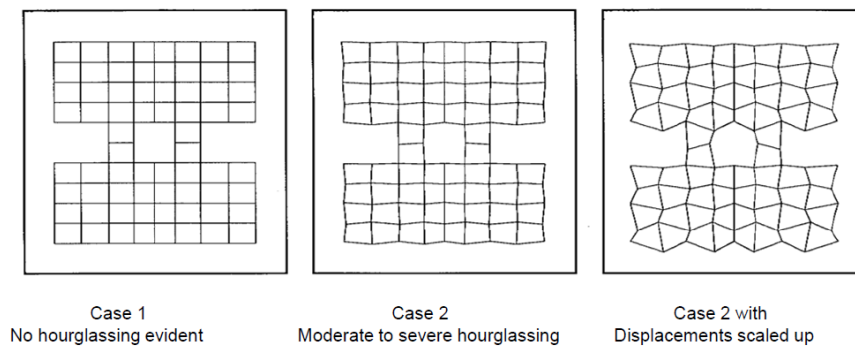**Figure 2.3:** Beam element defined in LS-DYNA [25]

Shell Elements

Shell elements are curved isoparametric elements. If geometry is flat, it can be utilized to solve plane stress and plate bending problems that are where thickness is considerably smaller than other dimensions. Shells are commonly used due to their ability to model membranes, plates, and surfaces. Stresses in shells generate membrane stresses in addition to bending. They generally have 6 DOF per node, rotation, and translational in 3D-space. General shell elements normally have three (triangle) or four nodes (quadrilateral) [23]. LS-DYNA allows for defining three, four, six, and eight-node shell elements [25]. And node numbering is done counterclockwise as represented in figure 2.4.

Figure 2.4: Shell element defined in LS-DYNA [25]

Hourglassing

Hourglass modes are non-physical modes of deformation, that might occur during FE-modelling, they do not generate stress but takes away energy from the system [26]. Hour-glass mode is relevant for shell elements with a single in-plane integration point or solid elements with a single integration point. Because one-point integration is computationally cheaper, hourglassing should be minimized. (Fully integrated shells or solids do not hourglass). This is prevented by applying internal forces to resist hourglass modes in LS-DYNA using the keyword *HOURGLASS.

Case 1
No hourglassing evident

Case 2
Moderate to severe hourglassing

Case 2 with
Displacements scaled up

**Figure 2.5:** Hourglass modes [27].

Mass scaling

Mass scaling means adding non-physical mass to elements to achieve a larger timestep. This is usually done to increase timesteps for small elements in order to reduce computational time. If the amount of scaled elements is relatively low, the added amount of mass is justifiable. It is up to the analyst to gauge the effects of mass scaling. The keyword *CONTROL TIMESTEP in LS-DYNA employs automatic mass scaling by artificially increasing the density of elements in the selected time-step range [28]. If a negative value is entered, all elements with a smaller timestep than the absolute value will be mass scaled.

For the local analysis, mass scaling for timesteps below 2.0^{-6} was executed which gave an added mass percentage of 0.06. This was assumed to be negligible on the results, and reduced the computational time by several hours.

2.2.6 Contact Formulation in FEM

Contact is referred to as boundary non-linearity in the contact area between two elements. For the purpose of modeling a collision, the correct formulation of contact is important. When two arbitrary bodies contact, contact forces arise, these can cause large stresses because the contact area can be rather small.

In FEM, a so-called slave-master contact formulation is normally used. The condition is that the slave body cannot penetrate the master body, but the master body can penetrate the slave body. When contact occurs, a node to node or surface to surface search is carried out for every time step [29]. If some segments violate the constraint, that is the slave body penetrates the master body, contact forces are applied and ultimately eliminates the penetration [30]. Figure 2.6 and 2.7 display this consecutively.
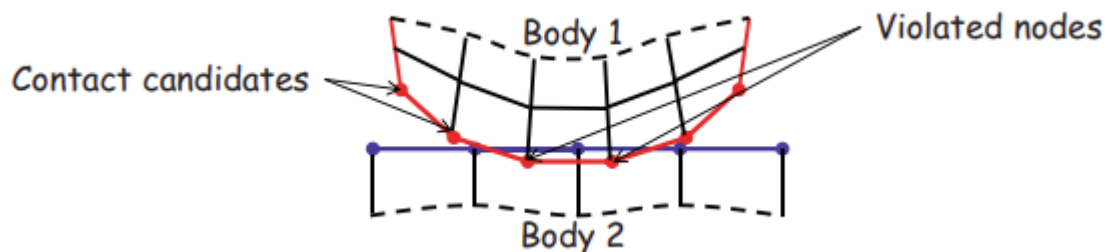
Figure 2.6: Principle of surface search and violation of contact restraints [30]
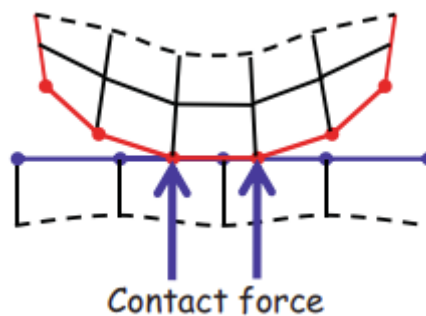
Figure 2.7: Principle of applied contact forces [30]

From Dynasupport [31]: In crash analysis, the deformations can be very large and predetermination of where and how contact will take place may be difficult or impossible. For this reason, the automatic contact options are recommended in LS-DYNA as these contacts are non-oriented, meaning they can detect penetration coming from either side of a shell element. Automatic contact types determine the contact surfaces by projecting normally from the shell mid-plane a distance equal to one-half the 'contact thickness'. Further, at the exterior edge of a shell surface, the contact surface wraps around the shell edge with a radius equal to one-half the contact thickness thus forming a continuous contact surface. Most contact types in LS-DYNA place a limit on the

maximum penetration depth that is allowed before the slave node is released and its contact forces are set to zero.

During modeling, the following contact types have been utilized:

Automatic single surface

Automatic single surface is the most used contact option in LS-DYNA, especially for crashworthiness applications. In this type of contact formulation, the slave surface is defined as a list of part ID's and no master surface needs to be defined. Contact is considered between all parts in the slave list, including the self-contact of each part. These contact types are very reliable and accurate if the model is defined accurately. There is a slight concern, energy balances may show either growth or decay of energy as calculation proceeds if there are a lot of interpretations in the initial configuration [31].

Automatic surface to surface

Automatic surface to surface contact works in the same manner as automatic single surface contact, except that the subroutines of checking slave nodes for penetration are done an extra time to check the master nodes for penetration through the slave segments. This means that the treatment is symmetric, and defining master and slave surfaces become arbitrary because the results will be the same. The extra subroutine increases the computational effort approximately by a factor of two [31].

Automatic surface to surface contact is recommended in crash simulations. This is because the orientation of parts relative to each other is hard to anticipate when there are large deformations and this formulation automatically checks for penetration at either side of a shell element [31].

Contact formulations can be used simultaneously with plasticity/hardening models.

2.2.7 Dynamic response in FEA from short duration loading

Collisions can generally be considered as short-duration loads, also called impact loads. These loads usually have a large magnitude that varies with time and acts for a specified period before the disappearance. From dynamics, it is commonly known that impulse can be measured by finding the change in momentum of the system. There are various methods available to find the response of a system subjected to an impulse load, Fourier transformations, method of convolution integral, Laplace transformation and numerical integration of the equation of motion [32]. In LS-DYNA, the response is determined through numerical integration of the equation of motion with the central difference method when the analysis is non-linear [27].

Central Difference Method

According to Rao [32] the central difference method is the most accurate method amongst the finite difference methods of numerical integration. The solution domain is replaced with a finite number of points, referred to as mesh or grid points. The main idea is to use a numerical approximation to the derivatives, and substitute them into the equation of motion. The central difference approximation can be derived from Taylor series expansions and relates the velocity at a certain time step to the displacement at both the previous(x_{i-1}) and continuous (x_{i+1}) time step.
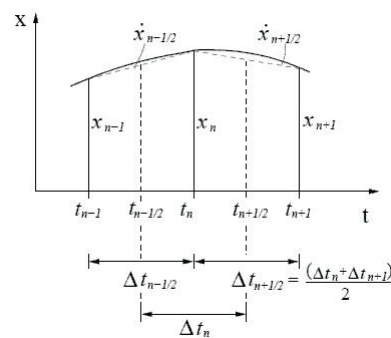

Figure 2.8: Central difference method [27].

The central difference approximation to the first derivative is;

$$\dot{x}_i = \left.\frac{dx}{dt}\right|_{t_i} = \frac{1}{2h}(x_{i+1} - x_{i-1}) \tag{2.2}$$

For the second derivative, the approximation is;

$$\ddot{x}_i = \left.\frac{d^2x}{d^2t}\right|_{t_i} = \frac{1}{h^2}(x_{i+1} - 2x_i - x_{i-1}) \tag{2.3}$$

From equation 2.3 and 2.4 the equation of motion becomes;

$$[m]\frac{1}{h^2}(x_{i+1} - 2x_i - x_{i-1}) + [c]\frac{1}{2h^2}(x_{i+1} - x_{i-1}) + [k]x_i = F_i \tag{2.4}$$

The derivation of the various steps of $\dot{x}_0$ $\dot{x}_i$, $\dot{x}_{i+1}$ and $\dot{x}_{i-1}$ are shown in Rao [32] p. 948 and the numerical procedure to evaluate the equation of motion is then;

1. From known initial conditions, $x(t = 0) = x_0$ and $\dot{x}(t = 0) = \dot{x}_0$ compute $\ddot{x}(t = 0) = \ddot{x}_0$

2. Select a time step where $\Delta t < \Delta t_{crit}$ (Critical time step to avoid truncation error. $\Delta t_{crit} = \frac{\tau}{\pi}$)

3. Compute $\dot{x}_{i-1}$

4. Find $\dot{x}_{i+1}$ starting with i=0

Equation of motion for FEA

As indirectly shown in equation 2.4 the equation of motion for a finite element system with several DOF consists of mass, damping, and stiffness matrices. It is thus an extension of equation 2.1 and the static stiffness matrix is also applicable to the global analysis.

$$[M][\ddot{D}] + [C][\dot{D}] + [k][D] = [R_{ext}] \tag{2.5}$$

Equation 2.5 is a system of coupled, second-order differential equations in time. Each differential equation constitutes a semi discretization where nodal DOF [D] are discrete functions in space but continuous over time. By applying numerical integration, the solution is discretized in time.
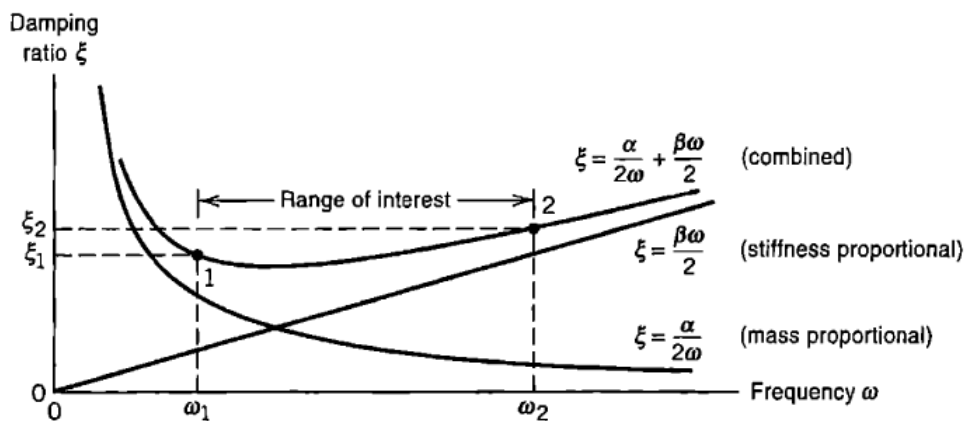
Damping

Damping is the mechanism where vibrational energy is gradually converted into heat and sound. Every vibrating system is subjected to damping, if not, the free vibration amplitudes will never decrease. Although the amount of energy dissipated is relatively small, considering damping is important to obtain accurate predictions of a systems vibration response [32]. Several damping models are available such as viscous-, hysteresis-, coulomb- and radiation damping. Viscous damping is the most commonly used damping mechanism utilized and is also referred to as Rayleigh damping. This is also available in LS-DYNA.

Rayleigh Damping

Rayleigh damping considers the damping of vibrations surrounded by gas, liquid, or viscous dampers added to the structure. The energy dissipated per vibration cycle is proportional to frequency and to the square of the amplitude, [23]. There are two ways of representing Rayleigh damping, proportional damping, and modal damping. Either is conveniently computational unless damping characteristics vary throughout the structure [23]. Proportional Rayleigh damping defines a global damping matrix [C] as a linear combination of the global mass and stiffness matrix.

$$[C] = \alpha[M] + \beta[K] \tag{2.6}$$

α and β are numerical values that limit the modal damping ratio and can also be expressed as weight factors. This makes damping frequency-dependent shown in the figure 2.9 below.

Figure 2.9: Fraction of critical damping for the proportional-damping scheme [23]

The damping ratio is a fraction of critical damping and presented in equation 2.7 below: c damping coefficient, c_c is critical damping coefficient, m is the mass and ω is the natural frequency. Damping of structures are often small, typical $\xi < 0.15$ [23].

$$\xi = \frac{c}{c_c} = \frac{c}{2m\omega} \tag{2.7}$$

The vibration mode for the nth mode of a system is described in equation 2.8 and the coefficients α and β are determined based on targeted values of damping ratios at two relevant eigenfrequencies. Because several eigenvalues exist for a system with several DOF, the damping ratio will also vary.

$$\xi_n = \frac{\alpha}{2\omega_n} = \frac{1}{2m\omega_n}\alpha + \frac{\omega_n}{2}\beta \tag{2.8}$$

To calculate α and β , two reference damping ratios ξ_i and ξ_j to the ith and j^{th} mode with frequencies ω_i and ω_j are chosen, then equation 2.8 is solved for α and β. The α[M] contribution damps lowest modes most heavily, while the β[K] contribution damps highest modes most heavily [23].

2.2.8 Material modelling

Steel

Steel is one of the most common building materials worldwide. The most characteristic behavior for steel is that it is ductile, as well as strong compared to its weight. Steel is suitable for both tension and compression. In maritime environments, but also most in other environments, steel should be coated or have a corrosion protection system in order to prevent degradation.

From Figure 2.10 , one can see a linear relation between stress and strain, until the point f_y. This means that when the stress increases, there is a proportional increase in strain. The slope of the curve is E, which is the modulus of elasticity. The value represents deformation resistance in the elastic spectrum. E normally varies between 200.000 - 210.000 $\frac{N}{mm^2}$.
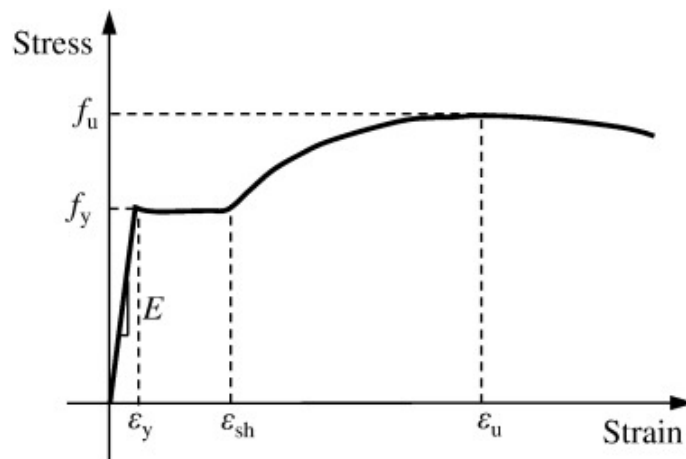
Figure 2.10: Typical stress vs strain diagram

When stress is in the linear part of the curve, the steel remains elastic, meaning that it recovers perfectly after unloading. The limit for elastic behavior is the yield stress f_y. When stress exceeds the yield point, the steel starts to flow plastic. This means that strain increases while the stress remains constant. This behavior remains until the strain-hardening phase starts. The strain-hardening is briefly explained by that the plastic deformation increases the dislocation density. Deformation changes the crystal structure, and for steel, this change results in a higher strength [33]. This phenomenon is referred to as strain-hardening. The strain-hardening accounts for the ductility of steel, and allowance to let stress exceed f_y, or yield point. This goes on until the stress increases to the ultimate f_u. At this point, the cross-sectional area will reduce, necking, before the member fractures, at f_u, ultimate stress. This behavior is common for all isotropic metals.

Aluminium

Aluminum is the second most used metal in the construction industry after steel. Aluminium alloys are beneficial due to light weight and non-corrosive properties. The density of aluminium is normally around 2700 kg/m^3 and under normal conditions, aluminium develops an oxide layer on the surface, preventing corrosion. Compared to steel, the aluminium stress-strain curve has the same shape as shown in figure 2.10. This indicates that aluminium also allows for plastic deformation in the same manner as explained in chapter 2.2.8 above. Another benefit is that the energy absorption per unit density is high compared to conventional steel. This characteristic allows it to be used laminated with other high strength steels for armor structures like a girder, allowing for better collision design when exposed to plastic deformation [22].

2.2.9 Material Models in LS-DYNA

In this section, common LS-DYNA material models, as well as utilized material models for this project, will be presented. Since steel and aluminium behave similarly, the same models have been used by changing input parameters as density, E-modulus, Poisson's ratio, yield stress, etc. Well-defined and robust material models are essential in order to have robust model behavior. A robust model means that it is insensitive to small changes in simulation set-up [34].

MAT003 PLASTIC KINEMATIC

From [35]: This is Material Type 3. This model is suited to model isotropic and kinematic hardening plasticity with the option of including strain rate effects to account for sudden brittle failure. It is a very cost-effective model and is available for beam (Hughes-Liu and Truss), shell, and solid elements.
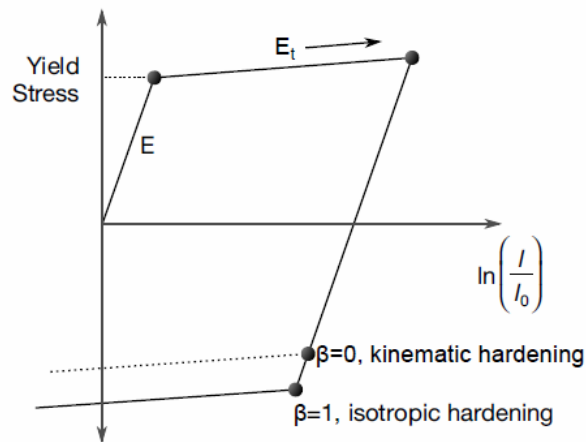
Figure 2.11: Elastic-plastic behavior with kinematic and isotropic hardening where l_0 and l are undeformed and deformed lengths of uniaxial tension specimen. E is the slope of the bilinear stress strain curve [35]

MAT024 Piecewise Linear Plasticity

From [35]: This is Material Type 24, which is an elastoplastic material with arbitrary stress versus strain curve and arbitrary strain rate dependency can be defined. Also, failure based on a plastic strain or a minimum time step size can be defined. In this material model, 8 points on the stress-strain curve beyond the yield point are defined, allowing for elastoplastic material behavior.
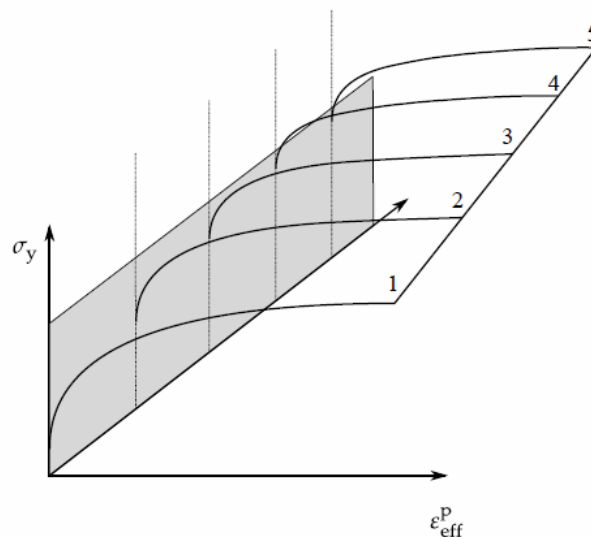
Figure 2.12: Rate effects may be accounted for by defining a table of curves. If a table ID is specified a curve ID is given for each strain rate, see *DEFINE TABLE. Intermediate values are found by interpolating between curves. Effective plastic strain versus yield stress is expected. If the strain rate values fall out of range, extrapolation is not used; rather, either the first or last curve determines the yield stress depending on whether the rate is low or high, respectively [35]

Strain rate is defined as the velocity of deformation. Strain rates increase initial yield stress and work hardening and consequently increases the flow stress and resistance to further deformation. Strains localize when a diffuse necking starts, and the strain rates in the localization zone increase. Strain-rate hardening then stabilizes the strain localization, and thereby the necking process. Thus the ductility of the material can be extended. On the other hand, an increase in strain rate is often believed to decrease the ductility [36]. LS-DYNA MAT024 allows for different ways of accounting for strain-rate effects. Load curves for the material can be inserted, a curve for the dynamic increase factor (DIF) for yield stress under certain strain rates can be added. In addition, there is an option to use the Cowper and Symonds model for strain-rate dependence which scales static stress with a dynamic hardening factor defined as the ratio between response at elevated strain rates compared to the response at $0.001s^{-1}$. This method often requires calibration against material tests. However, some strain rate parameters are suggested in [36]:

Factor for yield-stress scaling:

$$1 + (\frac{\dot{\epsilon}}{C})^{\frac{1}{p}} \tag{2.9}$$

where

- $\dot{\epsilon}$ is strain rate

- C and p are calibration parameters

For lack of data DNV RP-C208 recommends C= $4000s^{-1}$ and p=5 for common offshore materials [36].

MAT103 ANISOTROPIC VISCOPLASTIC

From [35]: This is Material Type 103. This anisotropic-viscoplastic material model applies to shell and brick elements. The material constants may be fit directly or, if desired, stress versus strain data may be input and a least-squares fit will be performed by LS-DYNA to determine the constants. Kinematic or isotopic or a combination of kinematic and isotropic hardening may be used. This model properly treats rate effects. The viscoplastic rate formulation is an option in other plasticity models in LS-DYNA, e.g., mat003 and mat024. This model also includes linear thermoelasticity, the Von Mises yield criterion, the associated flow rule, non-linear isotropic strain hardening, strain-rate hardening, temperature softening due to adiabatic heating, isotropic ductile damage, and failure but is not explained in detail in LS-DYNA documentation.

MAT041 USER DEFINED MATERIAL MODELS

The user must provide a material subroutine. This keyword input is used to define material properties for the subroutine. Isotopic, anisotropic, thermal, and hyperelastic material models with failure can be handled. This model is used for defining welds, orthotropic materials, or cohesive materials [35].

MAT020 RIGID

From [35]: This is Material 20. Parts made from this material are considered to belong to a rigid body (for each part ID). Also, global and local constraints on the mass center can be optionally defined. The rigid material type 20 provides a convenient way of turning one or more parts comprised of beams, shells, or solid elements into a rigid body. Approximating a deformable body as rigid is a preferred modeling technique in many real-world applications. For example, in sheet metal forming problems the tooling can properly and accurately be treated as rigid. In the design of restraint systems, the occupant can, for the purposes of early design studies, also be treated as rigid. Elements that are rigid are bypassed in the element processing and no storage is allocated for storing history variables; consequently, the rigid material type is very cost-efficient.

Young's modulus, E, and Poisson's ratio, are used for determining sliding interface parameters if the rigid body interacts in a contact definition

Constraint directions for rigid materials (CMO equal to +1 or -1) are fixed, that is, not updated, with time. To impose a constraint on a rigid body such that the constraint direction is updated as the rigid body rotates, use *BOUNDARY PRESCRIBED MOTION RIGID LOCAL.

2.2.10 Energy calculation and local analysis

When studying impact and impulse loads, the kinetic energy of the moving ship will transfer into displacement, deformation, vibrations, sound, noise, and heat. A common way to measure the local response of a structure after impact is plotting force vs. displacement by considering the conservation of energy, the energy will be dissipated into two parts. One kinetic part in turns generates free vibrations in the bridge and a second part consisting of the strain energy that leads to deformation. The strain energy will deform both the ship and the bridge.

The goal when simulating the local response is to evaluate the force-displacement curves, in order to obtain the loading for the global response analysis. This can also be compared to the loads given in NORSOK and Eurocode 1 presented in subchapter 2.2.11. When the local damage is known, reduced stiffness and capacities (reduced section modulus or second moment of inertia) can also be given as input to evaluate the damaged condition with a 100-year environmental loading applied to the bridge [34]. However, that is outside the scope of this thesis.
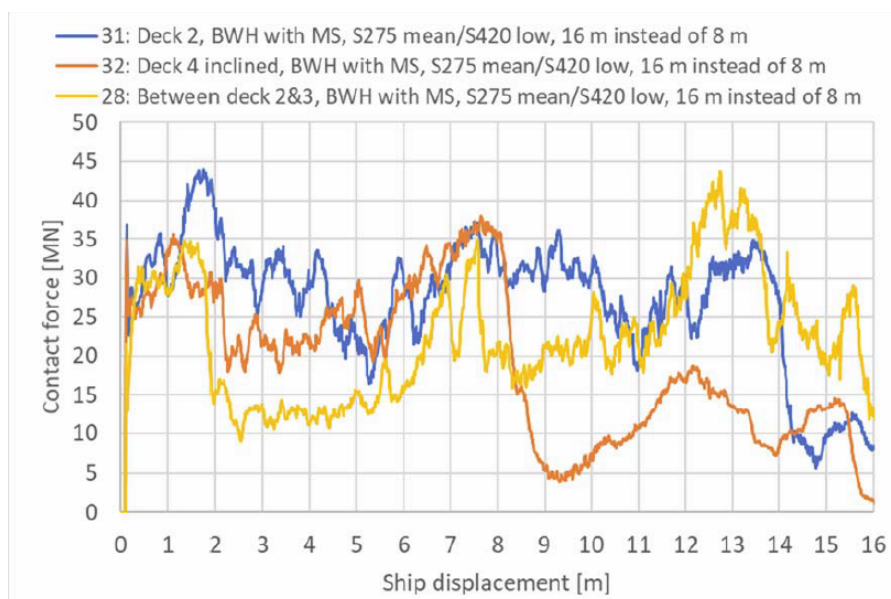

Figure 2.13: Example of load - displacement curve for different impact scenarios [34]

2.2.11   ALS and relevant standards

The accidental limit state (ALS) evaluation is one of the key aspects in the design of floating bridges. Common accidental loads to floating bridges include ship collisions, vehicle impacts, explosions, and earthquakes. Accidental impacts on bridges can pose a significant threat to the bridge structure. Extensive studies have been reported on ship collisions with bridge substructures, i.e. pylons, piers, and pontoons. Unfortunately, impact with bridge superstructures has not been well studied [10], and is to be further investigated in this thesis.

Ship impacts are defined as accidental load conditions related to a recurrence period of 10 000 years. NPRA has in handbook N400 set this as the limit where less likely events are disregarded. In the ALS all loads have a partial safety factor of 1.0. Local collapse is acceptable, provided the global stability can be maintained to prevent total collapse. For the bridge girder, this means that the bridge girder can be damaged causing a reduced stiffness, as long as the bridge can sustain a post-impact phase according to NS-EN 1991-1-7 [34].

According to Sha et al. [11] accidental ship collision is an important consideration in designing bridge structures across trafficked waterways. Ship impacts impose high kinetic energy and are therefore a threat to the structure. It is important to perform advanced analysis to assess the resistance. In large fjords, like Bjørnafjorden, ship traffic is more common due to the size of the fjord, and in these waterways, they normally have greater speed and displacement. (i.e. the weight of the ship and the cargo). This increases the risk related to a collision considerably as speed is higher and there are more ships passing. Therefore, bridges must resist collision loads without excessive deformation and collapse. Eurocode, NORSOK, and also ASSHTO contain simplified guidelines to estimate the impact force from ship collision. More recently, nonlinear FE models in LS-DYNA and ABAQUS are widely used for ship collision analysis This has offered better insight into structural behavior during ship collision, but ship to bridge collisions have limited literature [11]. In the following section, the content of Eurocode 1 and NORSOK N-003 will be briefly represented as they are the relevant standards to use in Norway.

Relevant Standards

Eurocode 1 - Actions on structures

Eurocode 1 - Actions on Structures, clause 4.6 contains a simplified guideline for estimating the impact force on a bridge deck from a ship collision. The type of ship should be taken into account using the CEMT classification system. On inland waterways, the collision should be considered as hard impact, with kinetic energy being dissipated by elastic or plastic deformation of the ship itself [37]. The analysis is recommended to be carried out as a dynamic analysis but conversion to an equivalent static force is also ok. In this thesis, an advanced dynamic analysis using LS-DYNA will be performed.
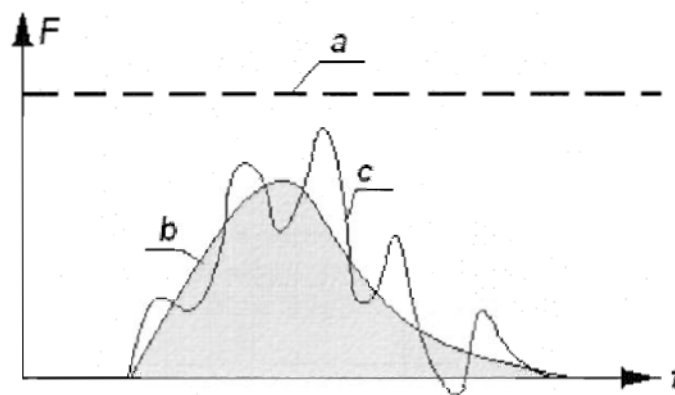
Figure 2.14: a) Equivalent static force b) Dynamic force c) Structural response from EC1 [37].

NORSOK N-003:2016 Actions and effects

According to NORSOK N-003 Actions and Effects [38], impact actions are characterized by kinetic energy, impact geometry relationship between action and indentation. From clause 9.3.2.1 Collision energy can be determined on basis of relevant masses, velocities, and direction of ships that may collide with the structure. All traffic shall be mapped, and impact should be based on an overall evaluation of possible events.

From NORSOK N-003: Type of ship is determined using table 5, and is categorizing impact energy for different vessels. ALS design checks should be made with impact events corresponding to a minimum exceedance probability of 10^{-4}.

When the duration of the collision is short compared with the periods governing the motion and the rate of loading is relatively small, the damage caused in the collision in structures with free modes may be determined in two steps.

1. First the distribution of impact energy between kinetic rotation and translation energy and deformation energy, can be determined by momentum and energy considerations.

2. Then local damage to vessel and facility can be determined so that the energy absorbed by the two structures corresponds to the energy that is to be absorbed as deformation energy.

If the impact duration is long compared with the relevant local or global periods of structural vibration, structural analysis to determine the energy absorption and damage can be done by a quasi-static method of analysis. This analysis can be based on load-indentation curves obtained by laboratory tests and analysis, as outlined in NORSOK N-004 or DNVGL-RP-C204. Otherwise, a dynamic structural analysis should be carried out.

2.2.12   Software validation

Software validation for FE software is comparing numerical solutions to experimental data or analytical solutions to quantify the accuracy of the results. In addition to validation, there is also verification. Software verification means ensuring that the model does not contain numerical or computational problems related to convergence, element types, geometry, etc [39]. Non-linearity in models such as plasticity in materials, contact formulations, and large deformations introduce challenges when validating results. The reason being analytical solutions or hand-calculations taking these effects into account are hard to obtain. To overcome this, experiments can be conducted, and the results can be compared. Experimental testing on full-scale ship collision would be extremely expensive and therefore scaled tests on typical members are performed to validate numerical methods, as shown in chapter 2.1. This is also done in NPRA's ship collision report K12 [34] to validate results from Abaqus. K12 also states that the standard DNVGL-RP-208, Determination of structural capacity by non-linear finite element analysis methods recommends using isotropic hardening and the Bressan-Williams-Hill instability criteria. In addition, LS-DYNA has been particularly widely used for collision simulations on marine and offshore structures in the past years and is widely validated on behalf of its use, and this is also evident from the literature review in chapter 2.1.

In addition to validating the model, verification of results is of great importance. A common way to verify the model and the results in complex models are using checklists with questions. Some questions could be [40]:

- Geometry—do key model dimensions agree with the actual part dimensions?

- Does the FE model mass and CG compare well with the actual part?

- Are the material properties correct and are they properly associated to model regions?

- Are element properties like shell thickness or beam properties correct and properly associated to model regions?

- Is the mesh sufficiently refined to produce the required accuracy?

- Are the applied loads and constraints correct—location, magnitude and direction?

- Are the element formulations consistent with the application?

- Are assemblies properly connected?

- Does the model pass free thermal expansion and rigid body motion checks?

- Have FE code errors and warning messages been reviewed and reconciled?

- Are the deformations and stresses believable—magnitude and direction? Do they compare well with hand calculations or similar analysis?

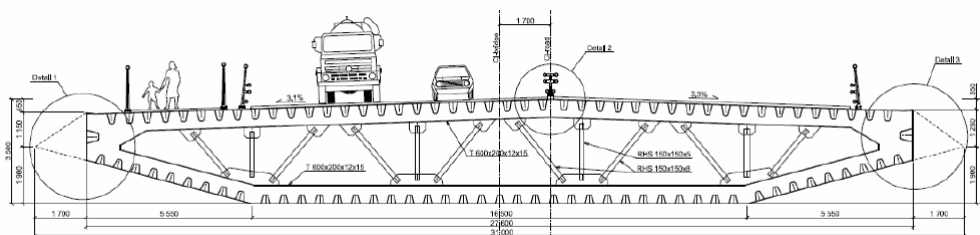- Are stresses continuous across elements?

Chapter 3

Bridge Parameters and Materials

To determine the response of the bridge, two models were used. One local model in LS-DYNA simulating the impact of one shipping container to obtain contact forces, local damage and energy dissipation. This model was developed with a 20 ft standard shipping container from Sha et al. [10], and a recent model of the updated bridge section supplied by the NPRA, these were put together to investigate different collision scenarios in order to obtain the highest contact force. Accurate modeling of the structural shape, geometrical dimension, and constitutive relationship is essential for numerical collision simulations [10]. When the force-displacement curves were obtained, a global model consisting of mainly line elements was built from scratch in Orcaflex according to the latest available drawings from NPRA to investigate the global response due to the contact force. Line elements in Orcaflex can be considered what is generally referred to as beam elements. The force-displacement curve obtained in the local analysis was applied as a load on the bridge girder in the global model. In the following chapter, the bridge sections, shipping container, tension cables, pontoons, columns, mooring lines, and the tower will be presented along with the material properties specified. The calculations of section properties are presented in Appendix B. The chapter is divided into the parameters used for the local and global analysis separately.

3.1 Local Analysis Bridge Parameters

3.1.1 Girder

The girder cross-section is 27 m in width and 4 m in height. The girder outer plate thickness is 14 mm in the top and bottom panels, and 12 mm in the side walls. The girder panels are strengthened by 8 mm thick hat-type stiffeners. The height of the hat stiffener supporting the top flange is 285 mm and the flange width is 150 mm. The flange width and stiffener height for side and bottom panels are 230 and 350 mm respectively. In the bottom flange, there are also L-type stiffeners with a thickness of 11 mm and a height of 280 mm. The top flange width and thickness are 50 mm and 30 mm respectively. The girder has an integrated design throughout the whole cross-section. The edge plates are supported by diaphragms with 4 m spacing that are connected on the top and bottom plates. The heights of the diaphragms supporting the bottom and the top panels are 600 mm and 1000 mm respectively. The diaphragm flange width is 280 mm. The diaphragms are supported by vertical trusses with a circular hollow cross-section. The trusses have a thickness of 10 mm and a diameter of 220 mm.

Figure 3.1: Bridge cross section [41]

The girder is modeled with the same steel or aluminium quality for all parts. During the investigation of aluminum properties, the same bridge geometry was also used. According to [42] aluminium of grade 6005A-T6 is intended used for the Langenuen crossing on E39 and has for that reason been chosen for this project as well. According to the data-sheet [43] the yield stress depends on the profiles and varies between 225-200 MPa. To be conservative, the yield stress was taken as 205 MPa when modeling.

| Material	Density ρ	E-modulus	Poissons ratio ν	Yield stress σ_y	ϵ_{fail}
S420	7850 kg/m^3	206 GPa	0.3	420 N/mm^2	0.20
Alu 6005A-T6	2700 kg/m^3	70 GPa	0.3	205 N/mm^2	0.08

Table 3.1: Material properties for the bridge girder [34]

Impacting container

The shipping container on the bridge deck in the impact analysis has been developed by Sha et al. [10] and is developed based on a 20-ft standard shipping container which measures 5.97 m in length, 2.43 m in width, and 2.82 m in depth. The frame structure of the shipping container consists of top and bottom rails, corner posts, and fittings, transverse and longitudinal beams. The corrugated front and side panels, top, and bottom floors were also modeled and steel properties were set to S355 steel. The container is shown in figure 3.2. The floor beams in the container were modeled with an increased artificial density such that the weight of the container floor was 34.4 tons. This was to simulate a fright-filled container.

Steel quality	Density ρ	E-modulus	Poissons ratio ν	Yield stress σ_y	ϵ_{fail}
S355	7890 kg/m^3	210 GPa	0.3	355 N/mm^2	0.27

Table 3.2: Material properties for the shipping container
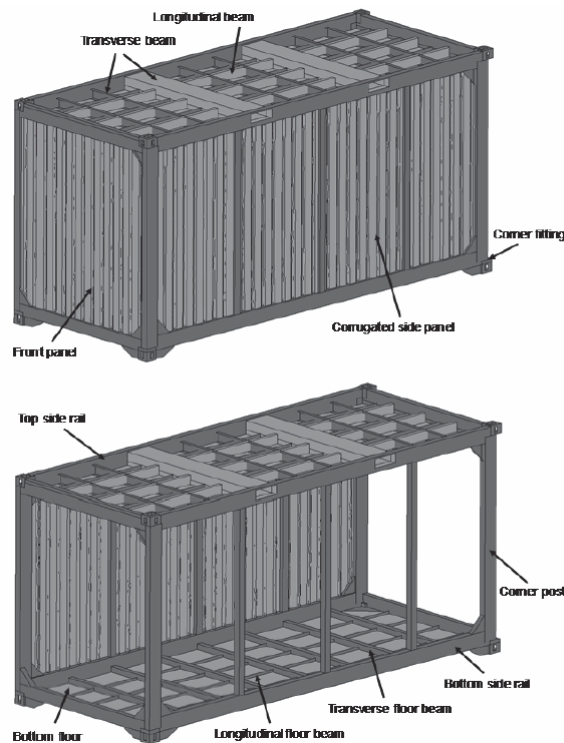
Figure 3.2: Shipping container [10]

3.2   Global Analysis Bridge Parameters

In this chapter, the parameters used to create the global model are presented. As local fracture was observed in the aluminium bridge girders, it has been chosen to conduct the global analysis with the parameters for a steel girder.
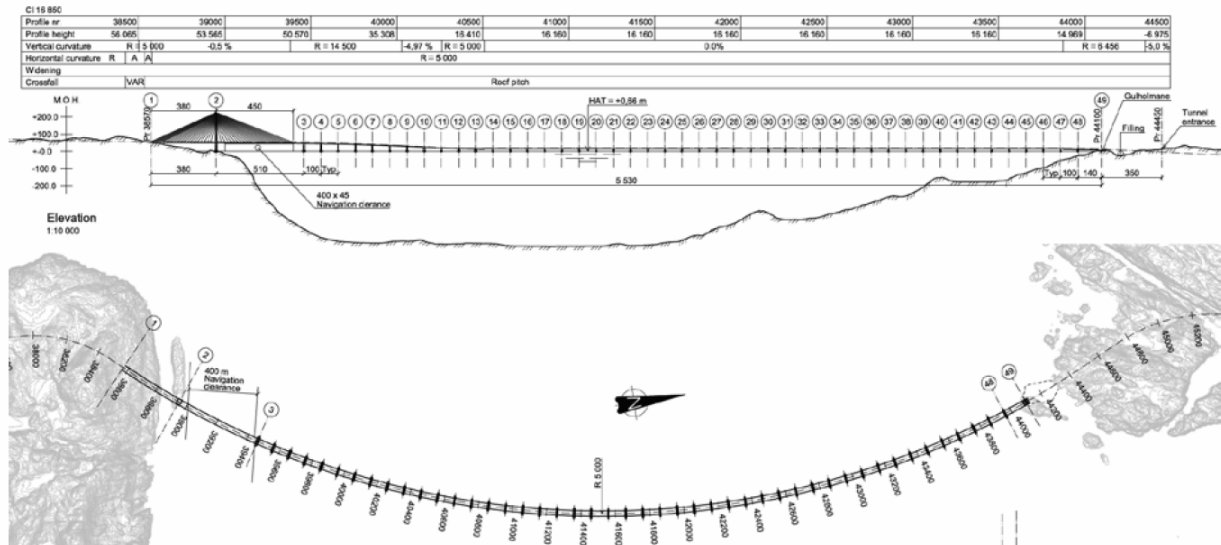

Figure 3.3: Overview of the bridge [44]

3.2.1   Geometry

General geometry

The end-anchored floating bridge across Bjørnafjorden is split into the following major structural elements (sub-systems):

- Bridge girder (carriage way)

- Pontoons

- Columns (between pontoons and bridge girder)

- Abutment South (south support of bridge)

- Cable-stayed bridge (tower, cables)

- Abutment North (north support of bridge at Gulholmen)

- Filling and approach bridge North of Gulholmen

An overview of the end-anchored bridge is shown in figure 3.3 and can also be found in report K12 [45]. The structural parts will now be thoroughly described in the following sub-chapters.

3.2.2 Girder

The bridge girder is split into three different parts. That is the cable-stayed bridge from axis 1 to 3, the high bridge from axis 3-13, and the low bridge from axis 13-49 in figure 3.3. Different cross-sections are decided upon and the main difference is the thickness of the stiffening plates as well as the first 4 spans which is a concrete girder. Cross-sectional parameters are presented in figure 3.5 below and are from NPRA's report Preferred solution, K12 Appendix F global analyses - modeling and assumptions [46]. The calculation of the stiffness constants is presented in Appendix B along with the locations of the various cross-sections. In the global model in Orcaflex, the bridge was modeled as line objects and divided into the span types presented in figure 3.5.
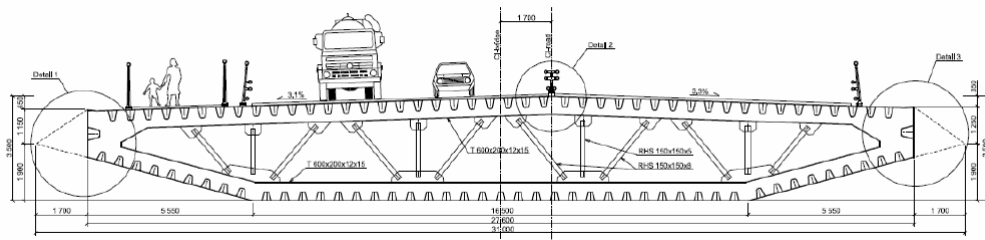

Figure 3.4: Bridge cross section [41]

|	M	Iy	Iz	J	Ax	Ly	Lz	VCGt
	[tonne/m]	[m^4]	[m^4]	[m^4]	[m^2]	[m]	[m]	[m]
K12_S1_02	19	3.668	110.4	11.349	1.779	27	4	1.989
K12_S2_00	19	3.785	121.83	12.01	1.8829	27	4	2.041
K12_T1_00	19	3.311	98.583	10.105	1.521	27	4	1.878
K12_F2_00	19	2.781	89.597	9.4228	1.331	27	4	1.763
K12_F1_05	19	2.569	84.698	8.6111	1.2699	27	4	1.682
K12_H1_02	19	2.534	89.531	6.629	1.297	27	3.5	1.463
K12_H2_02	19	3.64	123.34	9.663	1.797	27	3.5	1.633
C1	79.1	40.5	2138	135.4	27.951	29	3.5	1.463
Kxx_B1	19	5.32	170	18.2	2.09	27	4	1.989
Kxx_B2	20.52	5.95	226	20	2.28	27	4	1.989
Kxx_B3	25.16	7.7	314	24.3	2.86	27	4	1.989
Kxx_B4	29	9.74	423	28.5	3.34	27	4	1.989
Kxx_B5	30.12	10.06	461	29.7	3.48	27	4	1.989

Figure 3.5: Bridge cross-sectional properties [46]

3.2.3   Tower

The 220-meter A-shaped tower is shown in figure 3.6 and is modeled using line objects
in Orcaflex. The stiffness properties were taken from NPRA's report Preferred solution,
K12 Appendix L - Design of cable-stayed bridge [47] and the cross-sectional stiffness
was calculated per meter length. These calculations are presented in Appendix B. The
stiffness properties were used for the section at the cross-beam interface at the mid-height
of the tower as a simplification and are shown in table 3.3 below. The piers in the towers
were modeled as fixed in the top and bottom. The shape of the tower is optimal in terms
of ship collision because it is able to accommodate large forces in the transverse direction,
it is also stated that the ULS demand is equally important [47]. The bearing between
the girder and the tower was modeled as a constraint fixed in the z-direction and free in
all other directions.

Axial Stiffness	Bending stiffness strong	Bending stiffness weak	Weight / m
127.7 E4 kN	21.8 E6 kNm^2	10.8 E6 kNm^2	88 ton / m

Table 3.3: Cross sectional properties for bridge tower
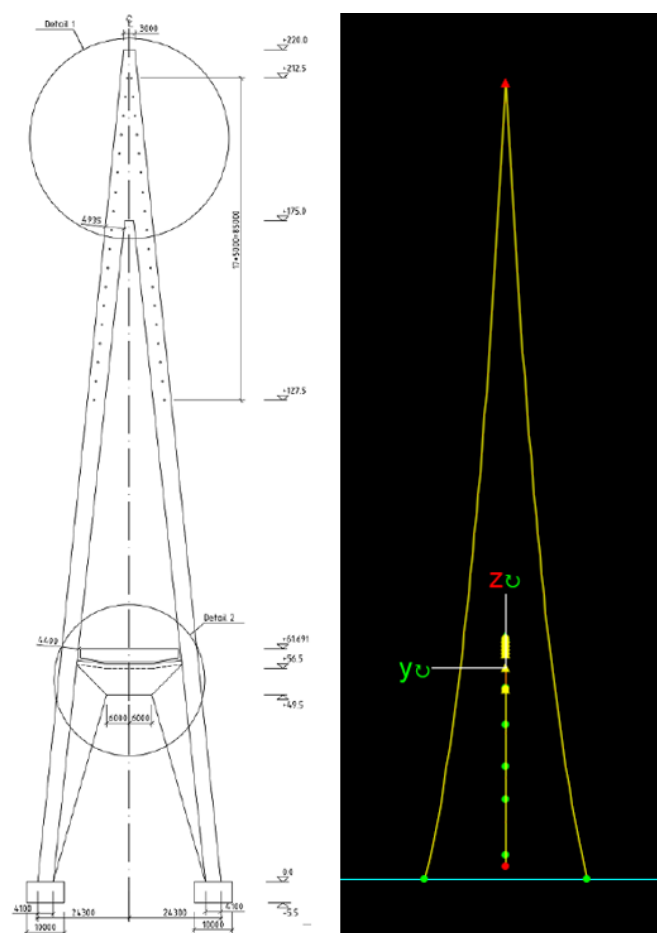
Figure 3.6: Illustration of concrete tower [44] and as modelled in Orcaflex.

3.2.4 Tension cables

The tension cables were modeled as line objects in Orcaflex connected between the towers and the bridge girder in the cable-stayed part. The sizes of the cables depend on the distance from the tower. The breaking loads were used as allowable tension. In addition, the pretension in the cables was added as a tensile force along the cable in the local coordinate system. The parameters were gathered from report Preferred solution, K12, Appendix A - Drawings Binder [44].

The cable properties for the main- and side span are shown in figure 3.7 below. Between axis 1C - 1E, the spacing of the cables was taken as 10m, and otherwise 20m as specified in [44]. The spacing in the vertical direction on the concrete tower was 5m.

		Side span																	
Cable no		18	17	16	15	14	13	12	11	10	9	8	7	6	5	4	3	2	1
Length	m	292	281	270	258	247	236	225	214	203	192	181	170	150	132	114	97	81	69
Breaking load	MN	17,0	17,0	17,0	17,0	17,0	17,0	15,3	15,3	15,3	15,3	12,0	12,0	12,0	10,3	10,3	8,6	8,6	8,6
Linear weight	kg/m	71,83	71,83	71,83	71,83	71,83	71,83	64,76	64,76	64,76	64,76	50,63	50,63	50,63	43,57	43,57	36,50	36,50	36,50

Main span																		
1	2	3	4	5	6	7	8	9	10	11	12	13	14	15	16	17	18
69	81	97	114	132	150	170	189	209	229	249	269	289	309	329	350	370	390
8,6	8,6	8,6	10,3	12,0	12,0	15,3	15,3	15,3	15,3	17,0	17,0	18,7	18,7	18,7	18,7	18,7	18,7
36,50	36,50	36,50	43,57	50,63	50,63	64,76	64,76	64,76	64,76	71,83	71,83	78,89	78,89	78,89	78,89	78,89	78,89

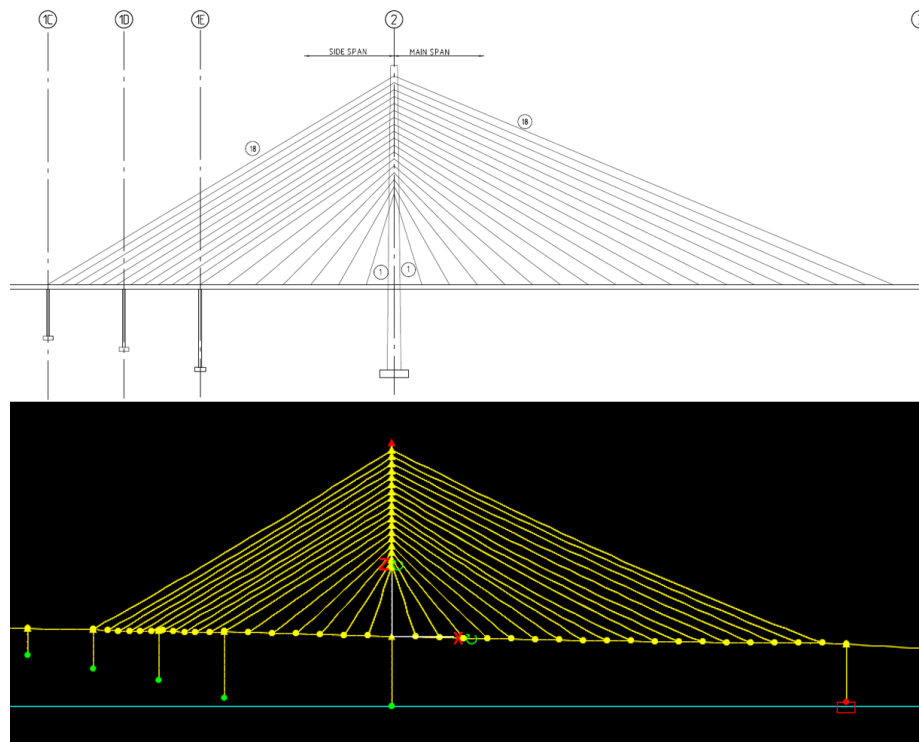**Figure 3.7:** Properties of tension cables [44].

**Figure 3.8:** Illustration of tension cables [44] and as modelled in Orcaflex.

3.2.5   Pontoons

Pontoons were modeled in Orcaflex for global analysis using vessel objects. Data was used from NPRA's report Preferred solution, K12 Appendix F - Global analysis, modeling and assumptions [46]. The circtangular pontoon was simplified into a rectangle with the properties described in table 3.4. The mass and moment of inertia were changed to account for ballast in the pontoons, supplied from my supervisor. The pontoon is shown in Figure 3.9. In addition, added mass and damping for sway, heave roll, and pitch were included for the pontoons as only these were documented in the report [46]. The pontoons were modeled as free vessels, except for the moored pontoons modeled as anchored vessels.

Pontoon Type	Moored	Conventional	Pontoon A3
Length	53m	53m	53m
Width	14.9m	14.9m	14,9m
Height	7.5m	5.0m	5.0m
Mass	4170t	1860t	2700t
Displaced volume	5566 m^3	3710 m^3	5200 m^3
I_{xx}	415 E3 t m^2	252 E3 t m^2	1.24 E6 t m^2
I_{yy}	995.7 E3 t m^2	439.3 E3 t m^2	77.6 E3 t m^2
I_{zz}	1054 E6 t m^2	470.3 E3 t m^2	756 E3 t m^2
Center of Gravity	-2.0m	-0.75m	-0.75m

Table 3.4: Material properties for pontoons
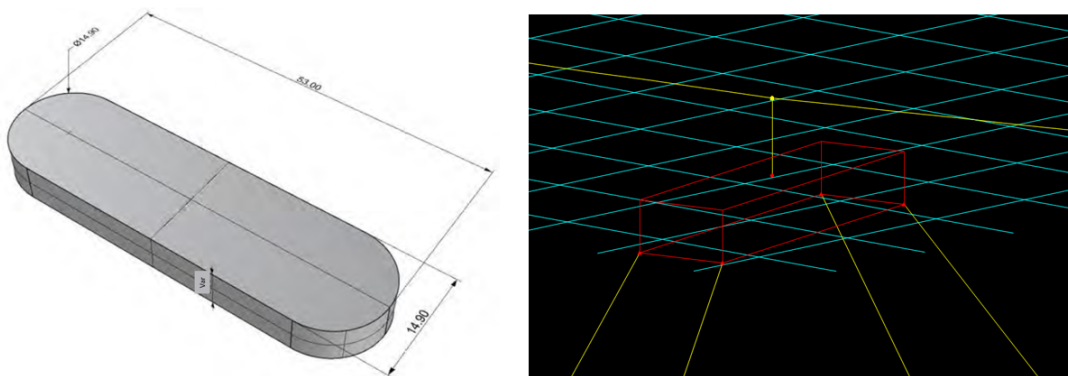
Figure 3.9: Pontoon geometry [46] and pontoon as modelled in Orcaflex

3.2.6 Columns

Columns were also modeled in Orcaflex for the global analysis as line objects. Data was used from NPRA's report Preferred solution, K12 - Appendix A Drawings binder [44], where the area, moment of inertia, polar moment of inertia was calculated to obtain the cross-sectional parameters. The calculations were simplified taking only the thickness of the inner and outer steel plates in the column into account. The parameters are described in table 3.5 below and are calculated per meter column. The calculations are presented in Appendix B. The axial stiffness input for Orcaflex is ExA , bending stiffness is ExI and torsional stiffness is GxJ. Three column types has been modeled, steel columns for the high bridge, steel columns for the low bridge, and concrete columns. Columns are modeled as fixed to the ground or to a pontoon, and at the top, they are connected to the end span of their respective bridge girder.

	Axial	Bending (x-x),(y-y)	Torsion	Weight
High Bridge	423.8 E6 kN	241.9 E7 kNm^2	186.6 E7 kNm^2	15.84 ton/m
Low Bridge	168.0 E6 kN	840.0 E6 kNm^2	550.8 E6 kNm^2	7.85 ton/m
Concrete	357.1 E6 kN	190.0 E7 , 669.6 E5 kNm^2	167.9 E6 kNm^2	31.80 ton/m

Table 3.5: Cross sectional properties for columns
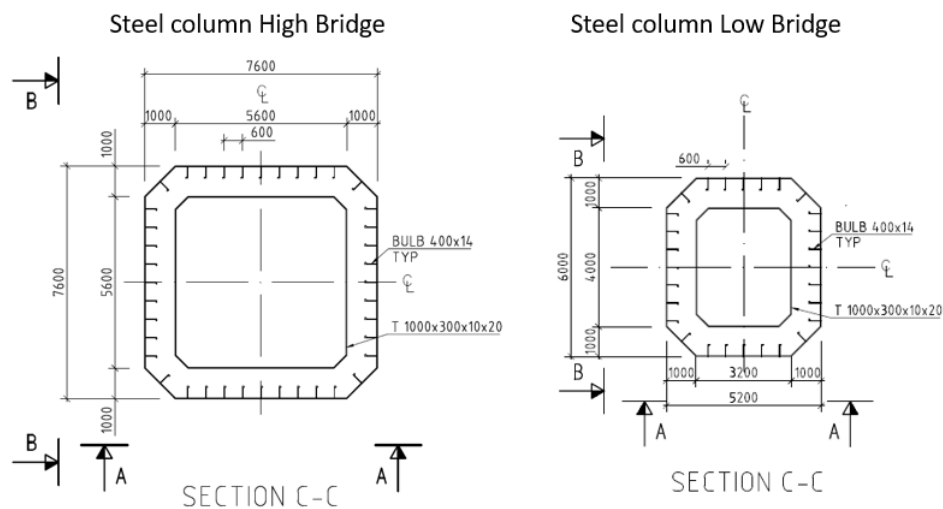
Figure 3.10: Column geometry [44]

3.2.7 Mooring Lines

Mooring lines were included in the global model in Orcaflex, based on NPRA's report Preferred solution, K12 Appendix M - Mooring system [45]. The lines were modeled as line objects with a given allowable tension from Table 3.6 below. It shows the allowable tension in the cables and is based on Table 5.5 ALS extreme line loads in [45]. The mooring lines were connected to the pontoons and anchored to the seafloor at the bottom. In addition, the pre-tension in the mooring lines was included and was obtained from [44].

Line nr.	Line break	Pretension	Line nr.	Line break	Pretension
1	3.0 MN	1.98 MN	7	3.3 MN	2.54 MN
2	3.1 MN	2.0 MN	8	3.6 MN	2.63 MN
3	3.9 MN	2.08 MN	9	3.1 MN	2.17 MN
4	3.7 MN	1.93 MN	10	2.2 MN	1.69 MN
5	3.3 MN	2.59 MN	11	4.3 MN	2.09 MN
6	3.0 MN	2.28 MN	12	4.3 MN	2.04 MN

Table 3.6: Mooring line properties
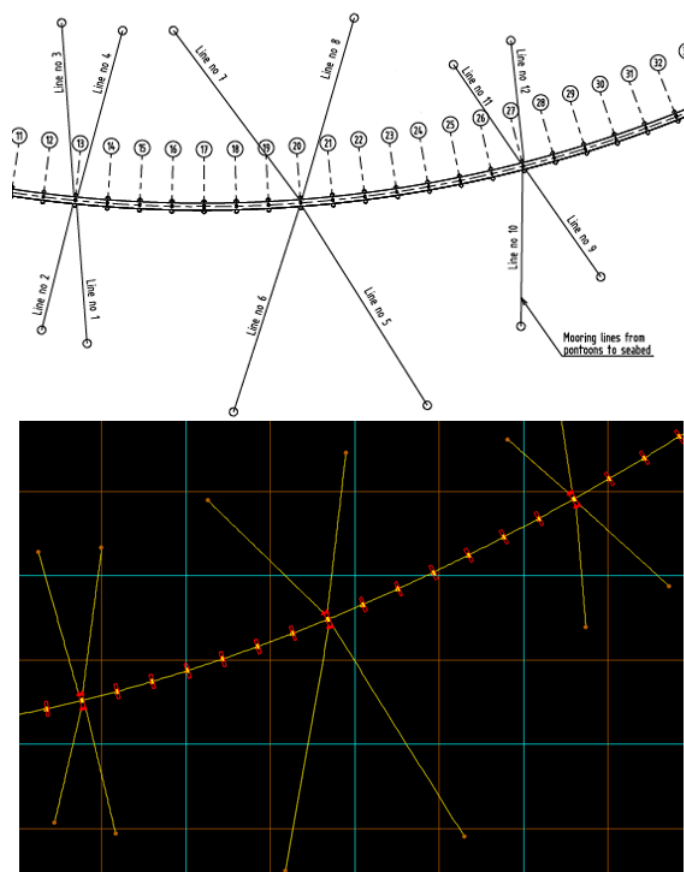
Figure 3.11: Illustration of mooring lines [44] and as modelled in Orcaflex.

Chapter 4

FEM-Model setup

4.1 Local analysis on bridge girder

Girder

The girder has been modeled using shell elements for all sub-structures such as plates, stiffeners, diaphragms, and reinforcement beams. All parts in the bridge girder were modeled using shell elements. To reduce computational efforts, 7 m of the total 27 m width of the cross-section was modeled in the numerical simulations as seen in figure 4.1 The steel girder and the aluminium girder have the same geometric design as shown in figure 4.2. The connected material models are MAT24, the same as presented in subsection 2.2.9. The steel section was modeled with S420 steel parameters according to table 3.1 and the same applies to the aluminium girder. The shell elements are meshed with an approximate size of 8x8 cm^2 in the finest region, figure 4.1 shows the mesh. The internal contact in the girder was defined using automatic single surface. The contact between the girder and the container was defined using automatic surface to surface, with the girder as the master and container as slave.

8 points from the plastic strain vs stress curve have been added to the material model in accordance with the manual description for MAT24 in LS-DYNA. The stress vs strain curve was developed from available curves from Eurocode 9 - Design of aluminium structures [48]. In addition, a dynamic increase factor (DIF) was added to scale the yield stress for corresponding strain-rate values. This is further explained in chapter 4.1.2 The curves are showed in Figure 4.4 and were used for all materials respectively.
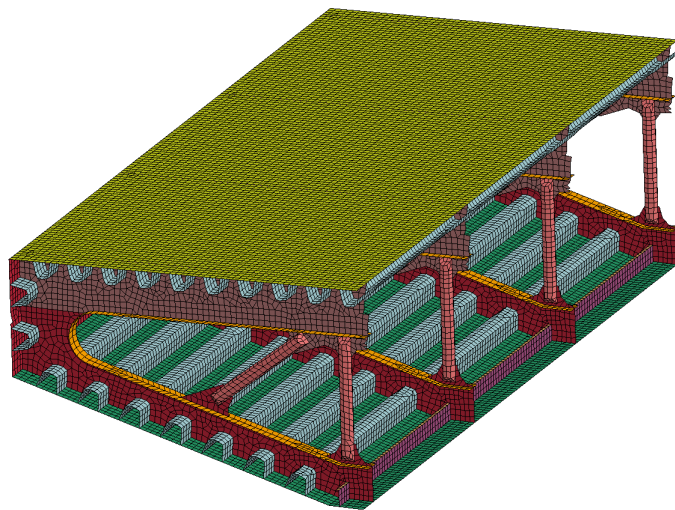
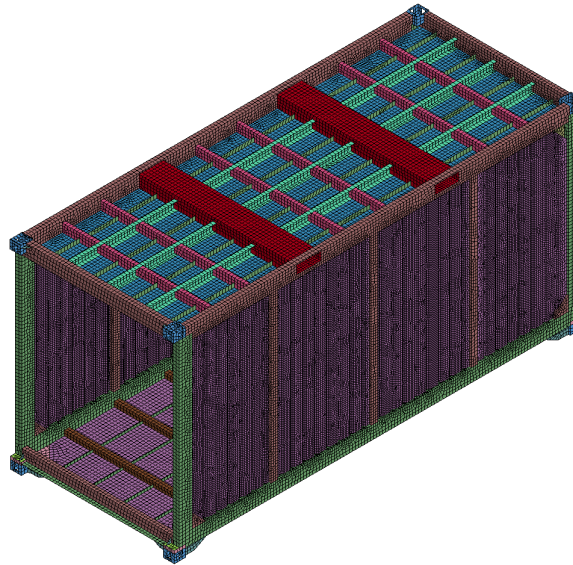**Figure 4.1:** Girder with FE-mesh
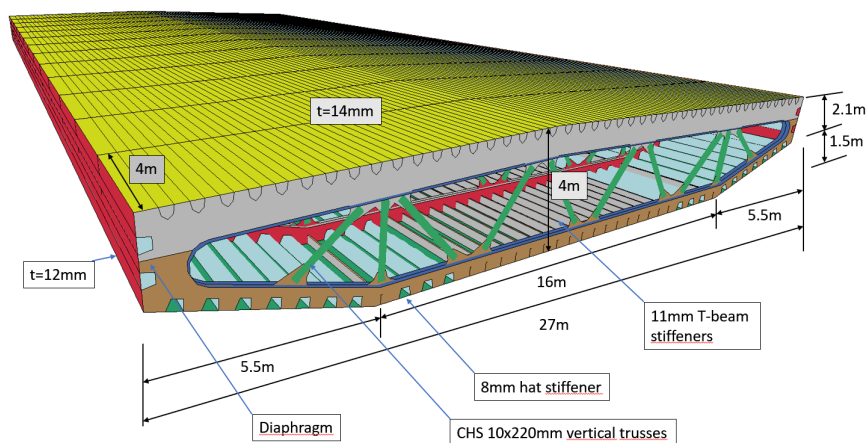
Figure 4.2: Representation of FE-Model of the bridge Girder

The boundary conditions for the bridge girder were defined by fixing all nodes on the edge of the diaphragms at each ends.
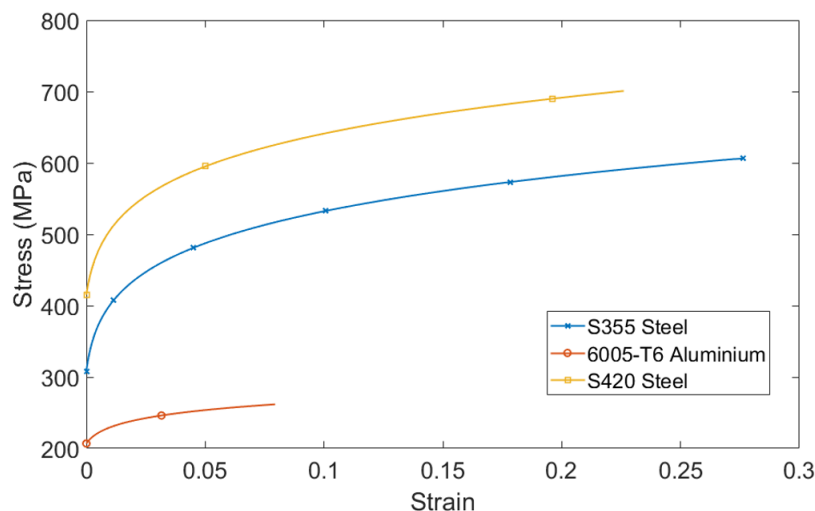
Shipping Container

Shell elements were used for the modeling of the whole shipping container and are shown in figure 4.3. The material model utilized was MAT24, the assigned material properties for S355 steel were defined according to table 3.2. The size of shell elements is approximately 5x5 cm^2, and the mesh is shown in figure 4.3 below. Internal contact in the container was defined using an automatic single surface.

8 points from the plastic strain vs stress curve have been added to the material model in accordance with the manual description for MAT24 in LS-DYNA. The stress vs strain curve was developed from available curves from [48]. In addition, a dynamic increase factor (DIF) was added to scale the yield stress for corresponding strain-rate values. This is further explained in chapter 4.1.2. Curves are showed in Figure 4.4 and were used for all materials respectively.

Figure 4.3: Container with FE-mesh

The boundary conditions on the shipping container were set by defining the initial velocity to the part set for the shipping container. The initial velocity was set to 10 m/s, corresponding to approximately 20 knots. This is at the boundary between normal sailing speed and slow sailing [49], which can be considered conservative, as the location is in a fjord, where ships normally travel at reduced speeds. When giving an object initial velocity instead of a prescribed motion in LS-DYNA, the velocity is not constant but will reduce on impact, this has also been further discussed in Chapter 6.1.

Figure 4.4: Stress vs strain curves used for FE- analysis.

4.1.1 Impact scenarios

According to a similar study, simulation of shipping container impact with bridge girders by Sha et al. [10], containers at 90-degree impact angle cause the largest impact force, this is due to increased bending resistance from the vertical and transverse beams on the container top and floor. However, a 90-degree impact is also the most unlikely scenario, as this would mean a sideways ship impact. Angled impacts gave the lowest impact force but were similar to the 0-degree impact. To further investigate, simulations of impact at 90, 45 and 0 degrees at different collision heights have been performed. Two different impact locations were investigated, container mid-wall and collision of the floor. The simulations were conducted for one girder with steel parameters, and one girder with aluminium parameters, but both girders have the same geometry. The different cases are displayed below in figure 4.5 - 4.7 and also in table 4.1

| Case Name	Impact angle	Impact height	Velocity
A00 bot	0 degrees	Bottom floor	10 m/s
A00 mid	0 degrees	Midwall	10 m/s
A45 bot	45 degrees	Bottom floor	10 m/s
A45 mid	45 degrees	Midwall	10 m/s
A90 bot	90 degrees	Bottom floor	10 m/s
A90 mid	90 degrees	Midwall	10 m/s

Table 4.1: Case description

A00: 0 degree impact
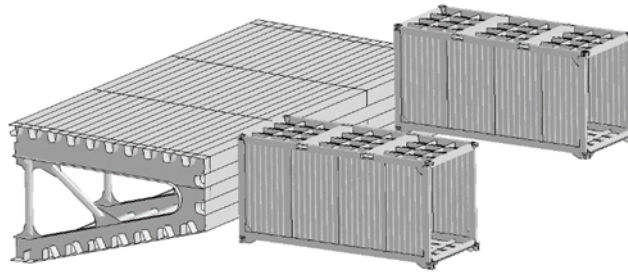
Figure 4.5: Container Impact at 0 degree angle. To the left A00 mid. To the right: A00 bot

A45: 45 degree impact
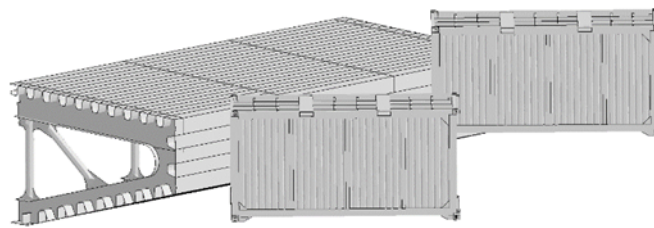
Figure 4.6: Container Impact at 45 degree angle. To the left A45 mid. To the right: A45 bot

A90: 90 degree impact
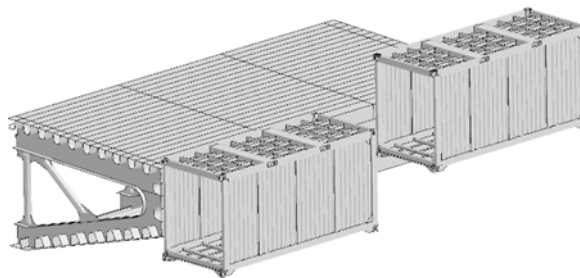
Figure 4.7: Container Impact at 90 degree angle. To the left A90 mid. To the right: A90 bot

4.1.2   Strain Rate sensitivity

The strain rate effect has been well studied for steel structures related to ship collision accidents. It is shown that strain rate can increase the yield stress of steel materials under a high loading rate. However, the fracture strain will also reduce at the same time. For aluminium, the effect of strain rate varies depending on the type and content of the alloyed material. In this study, numerical simulations were first conducted to explore the strain rate effect of 6005-T6 aluminium in ship collision simulations. To account for the strain rate, the dynamic increase factor (DIF) was used to scale the stress-strain relationship at the corresponding strain rate. The results with strain rate are compared with the benchmark case without DIF using the stress-stress curves from Figure 2.10. DIF used in this study was obtained from Zhu et al. [50] for S355 and S420 steel and Mohotti et al. [22] for aluminium. The DIF curve for S355 steel which is used for the shipping container is steeper than those used for the 6005-T6 aluminium and S420 steel.

Figures 4.8 - 4.10 shows the comparison of force-displacement curves with and without strain rate for different impact scenarios. For A90-bot cases, it is observed that including strain rate results in slightly early fracture compared with the base case. For other impact scenarios, strain rate almost has no effect on the force-deformation curve. However, the strain rate is nevertheless considered for all materials in the simulations presented in chapter 6.

| Case Name	With DIF	Without DIF	Relative Increase
A00 bot	3.95 MN	3.92 MN	0.76%
A00 mid	5.05 MN	5.05 MN	0%
A45 bot	2.00 MN	1.95 MN	2.5%
A45 mid	2.06 MN	2.02 MN	1.94 %
A90 bot	9.28 MN	9.27 MN	0 %
A90 mid	8.56 MN	8.56 MN	0 %

Table 4.2: Maximum contact forces in the aluminium bridge girder with and without strain-rate parameters.
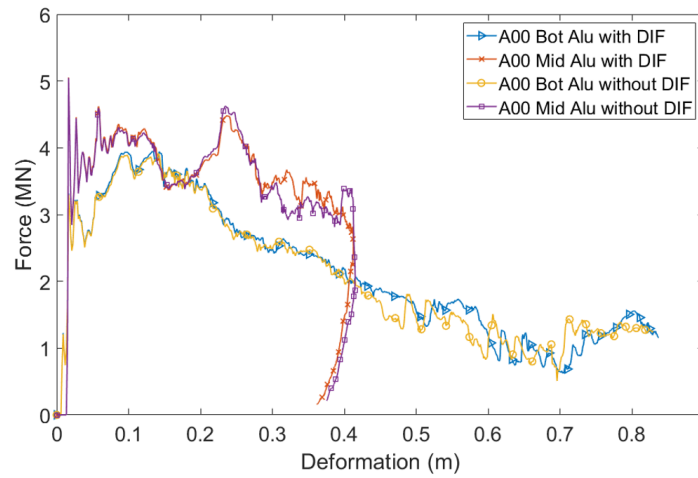
Figure 4.8: Force-displacement curves for A00 with and without strain rate
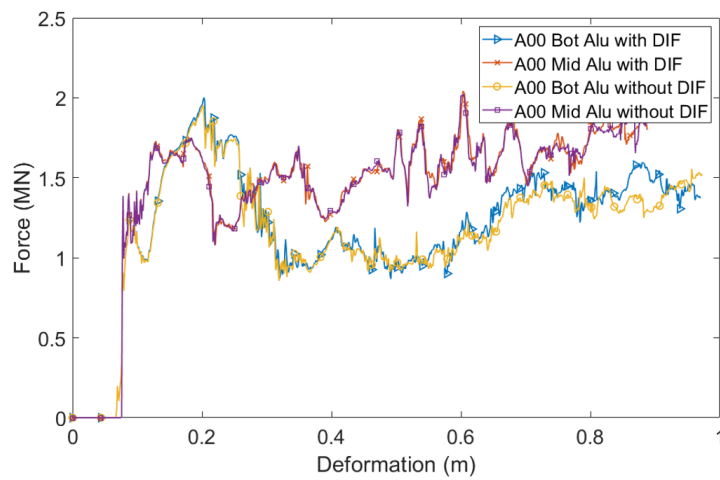
Figure 4.9: Force-displacement curves for A45 with and without strain rate
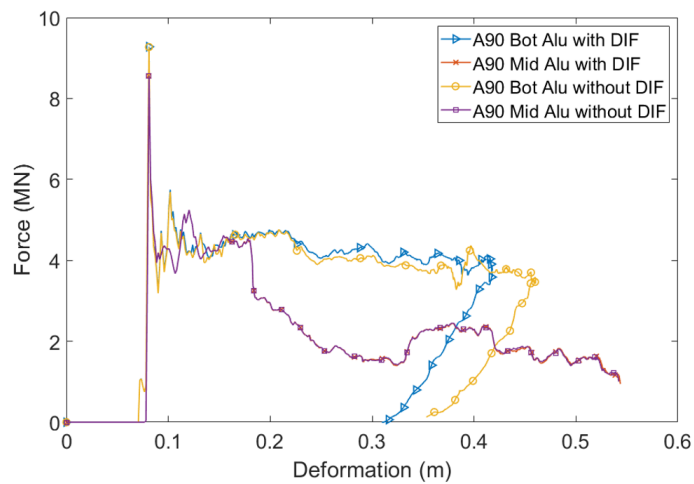
Figure 4.10: Force-displacement curves for A90 with and without strain rate

4.2   Global analysis on entire floating bridge

In the global analysis, the force-displacement relationship from the shipping container impact obtained from the local analysis has been modeled as a spring stiffness that generates contact with a girder element in the global model. The force-displacement relationship from the shipping container impact has been used in order to account for the strain-energy dissipation in the containers, impulse duration, and the peak force. The detailed procedure of modeling the structural parts has been explained in chapter 3.2. Each end of the bridge is modeled as fixed connections. In this part of the work, six springs alongside each other, represent the impact of 6 shipping containers at once. The spring stiffness is the obtained force-displacement curves obtained from LS-DYNA. This was done by applying a constraint with only one degree of freedom in the same direction as the impact that was investigated. The constraint is applied onto a mass-less 6D-buoy in order to generate contact in Orcaflex. In addition, an elastic solid is modeled inside the girder in order to generate contact between the constraint and girder. The constraint was assigned with translational stiffness in kN / m, here the force vs. deformation relationship from the shipping container impact was assigned. An illustration is showed in figure 4.14. The buoy with container stiffness properties was given the same dimensions as the shipping container and was then put in motion of 10 m/s by attaching them to a vessel. The vessel had no contact parameters that would interfere with the girder, pontoons, or columns. The location of the impact was taken on the high bridge at the fifth span between axis 7 and 8. Approximately in the middle of a cable-stayed part of the bridge and the first moored pontoon.
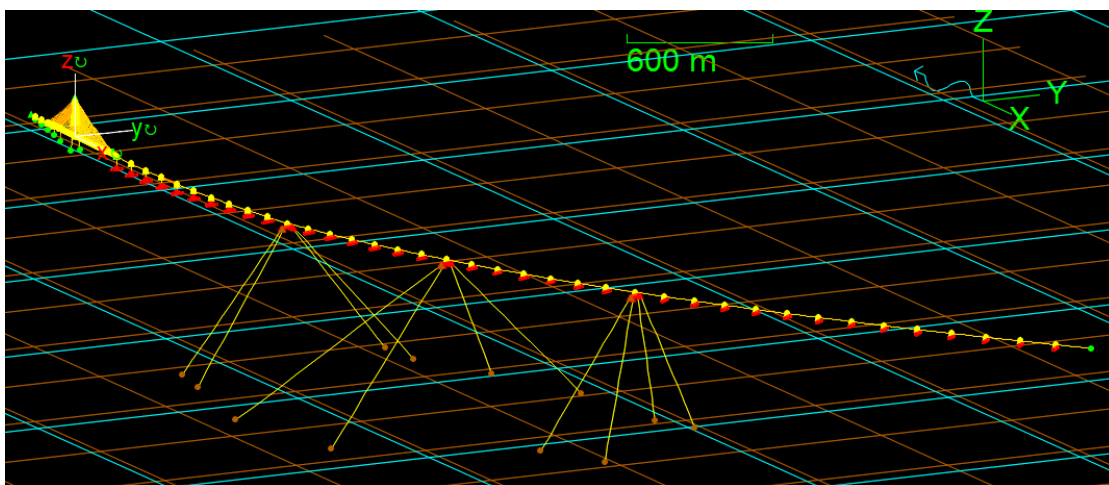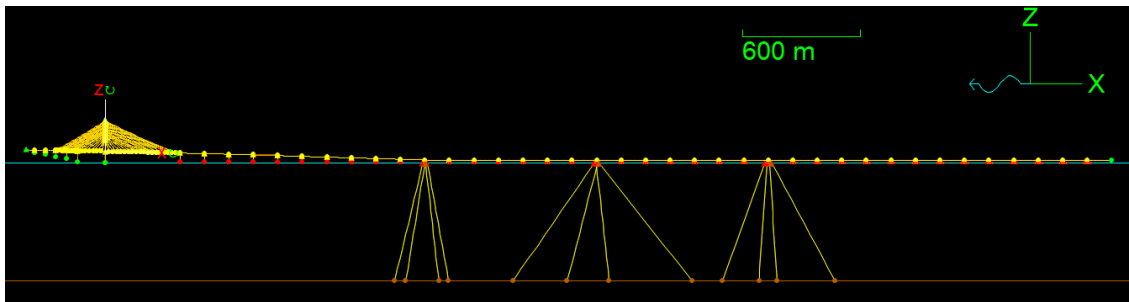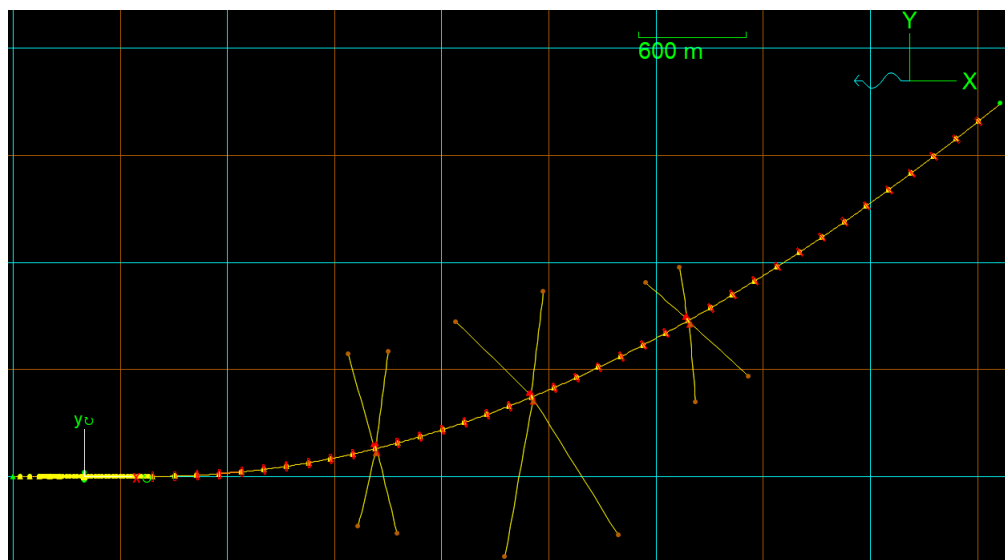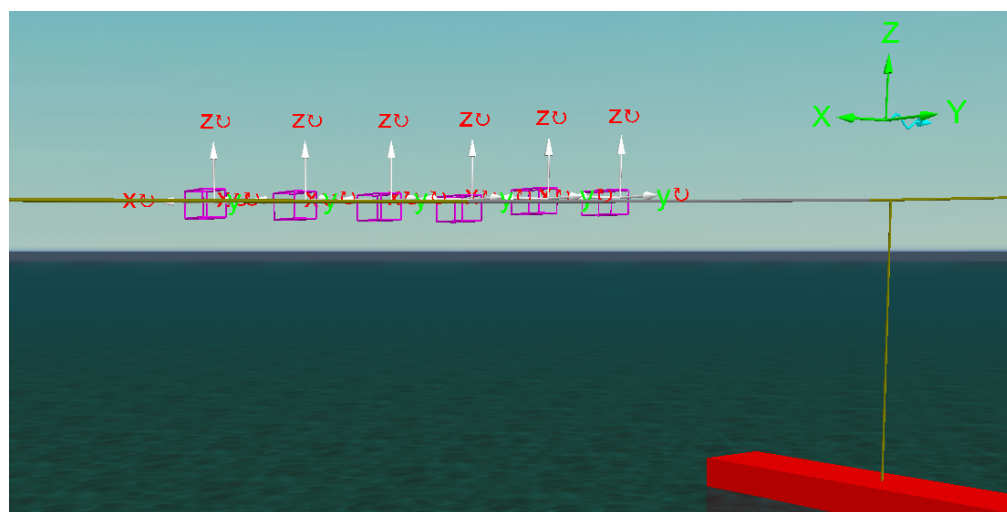

Figure 4.11: 3D View of the Global Orcaflex Model

**Figure 4.12:** Elevation view of the Global Orcaflex Model

Figure 4.13: Plan view of the Global Orcaflex Model

**Figure 4.14:** Illustration of the impacting containers in Orcaflex in shaded graphics mode

The local analysis resulted in a local fracture on the aluminum girder. Due to this, only the force-displacement relationship for the steel girder was investigated for the global

model, the force vs displacement relationship is presented in figure 4.15. Consequently, the material parameters calculated were also for steel girders. Since a 90 degree impact at 10 m/s might not be the most likely collision scenario, the second-highest impact relationship was chosen to be investigated. This was case A00 Mid Steel. The collision was simulated at the high bridge, the cross-section analyzed in the local analysis, at the fourth span from the cable-stayed bridge. This will be approximately in the middle between the cable-stay tower and the first moored pontoon. The collision is illustrated in figure 4.16.
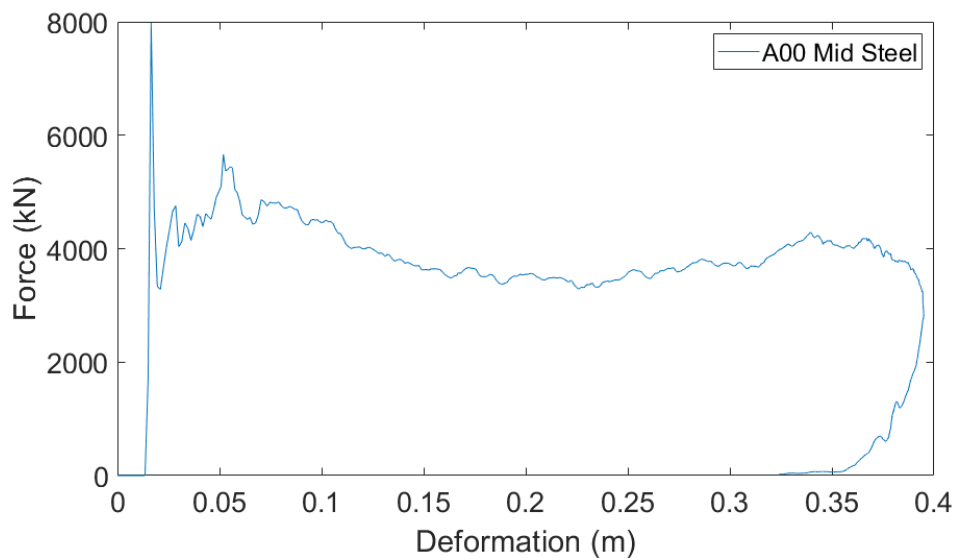
Figure 4.15: Force vs displacement relationship for containers in global analysis.

It is important to state that this curve is based on the initial velocity that showed a speed reduction for one single container. When stacking several containers, a different curve may be used, in addition, if there is cargo inside, this can change the force-displacement curve. This has been further discussed in chapter 6.2
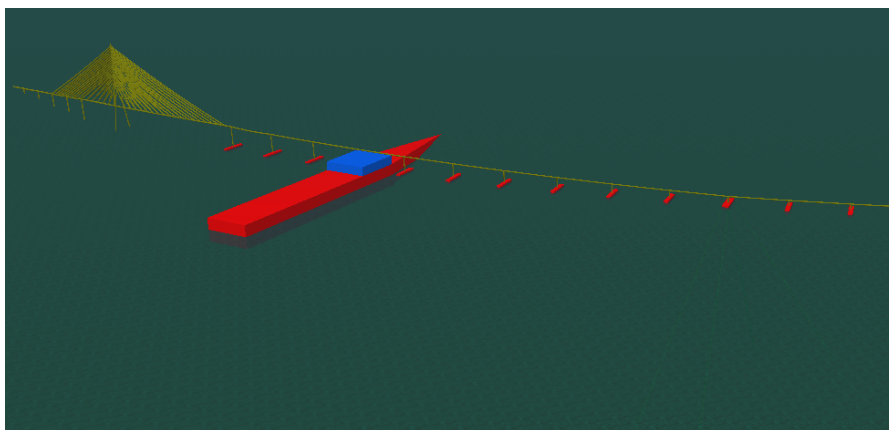
Figure 4.16: illustration of chosen collision scenario.The blue square is an illustration of a containerdeck

4.2.1 Assessment of Mode Shapes

In order to determine if the global model is close to the one developed by the consultants, a modal analysis was carried out in Orcaflex. This is also important if the model is going to be used for further dynamic analysis and model verification. The results are presented in table 4.3 and deviate from the mode shapes documented in [46]. Some of the frequencies seem to be around the same frequency. However, there are several discrepancies. The main reason could be the difference in stiffness parameters as these were hand calculated. Differences in mass and added mass also play a large role [51], and some modification of pontoon masses was carried out. Besides that, the modeling and calculation of cables, columns, and towers have also been simplified as stated in chapter 4.

Mode	Eigen-Period Reference	Eigen-Period Obtained
Mode 1	56.1 s	31.5 s
Mode 2	43.7 s	27.4 s
Mode 3	31.1 s	23.4 s
Mode 4	21.5 s	17.2 s
Mode 5	16.9 s	16.9 s
Mode 6	13.4 s	16.8 s
Mode 7	12.7 s	16.6
Mode 8	10.3 s	15.3 s
Mode 9	9.3 s	15.1 s
Mode 10	8.4 s	14.0 s

Table 4.3: Eigenmode comparison between model in NPRA reports [46] and the presented model

Chapter 5

Analysis Results

In the following chapter results from the cases presented in chapter 4 will be presented.

5.1 Local Analysis

For the local analysis, container impact simulations were conducted for both the aluminium and steel bridge girders. The impact force, structure deformation, and energy dissipation were compared between the girders with the two different materials. The displacement was tracked as the displacement of one node on the far end of the contact area of the shipping container. The initial distance between girder and container was 0.02m and was included in the displacement. This small distance was assumed to be non-significant to the indentation of the shipping container as it showed to be between 0.3-0.75m. The displacement of the sidewall of the bridge girder is summarized for the bottom cases in Table 4, as the bottom cases yielded the largest displacements.

5.1.1 Force - Displacement Curves

The force-displacement curves for shipping container impact with steel and aluminium bridge girders are shown in Figures 5.1 - 5.3 for three impact angles.

It can be observed that relatively vertical impact location has a significant effect on the impact response for all impact angles regardless of girder material. For mid-wall impacts, the instantaneous peak force upon impact is higher for the steel bridge girder than the aluminium girder as the steel girder induces larger deformations in the container than the aluminium girder. After the initial contact, the force-displacement curves are in the same range for both steel and aluminium bridge girders. This is because the structural

54

damage is mainly in the shipping container as shown in Figure 5.4. Limited damage occurs in the bridge girder regardless of the girder material. This suggests that for the mid-impacts, the material properties of the girder play a minor role as long as the girder has a higher strength than the container.

For the bottom impact cases, the first peak of impact force is still higher when the container collides with the steel girder than with the aluminium girder. After that, the force-displacement curves for steel and aluminium bridge girders show large derivations which are different from mid-wall impact cases. When impacting with the steel bridge girder, the first plateau in the force-displacement curves is larger than those of the aluminium bridge girder. This is because the steel bridge girder has higher strength and induces larger deformation in the container. Meanwhile, the span of the plateau in the force-displacement curve is shorter for the steel girder compared with the aluminium girder due to lower ductility.

For 0- and 90-degree middle impact cases, the shape of the force-displacement curves are quite similar. In these cases, the force level is determined by the bending and membrane of the two corner posts in the container as shown in Figure 5.4. For 45-degree cases, only one corner post was involved in the deformation process. For 0- and 45-degree bottom impact cases, the container corners penetrate the vertical side panel of the aluminium girder and thus result in a reduction of the impact force. For 90-degree impact, two girder diaphragms were engaged due to a large contact area with the container side panels. Thus, no fracture was observed in this case but the aluminium girder endures large deformation in the side panel. Table 5.1 shows that the maximum impact force of the steel girder is always larger than the aluminium girder for all impact scenarios. The deformation in the steel bridge girder is however smaller than that of the aluminium girder for bottom impact cases as shown in table 5.2. Girder deformations for middle impact cases are very small and thus are not listed in the table. In all cases, the relative displacement in the aluminium girder is larger than for the steel girder, and the magnitude of the contact forces seem to be related to the girder displacement.
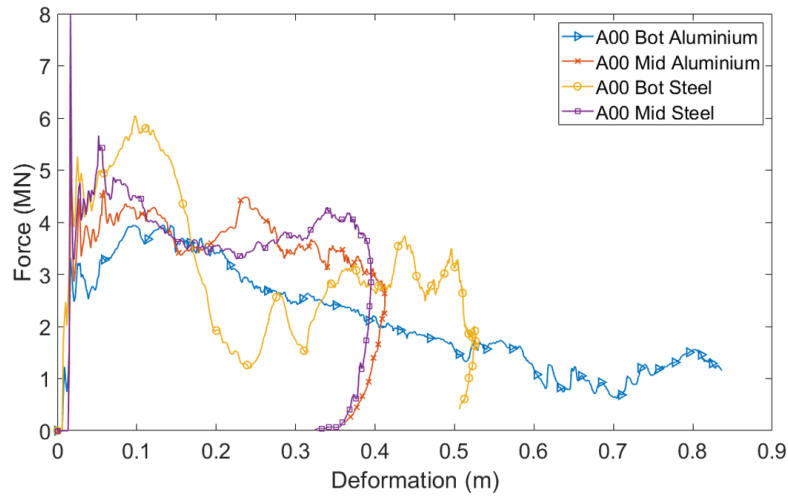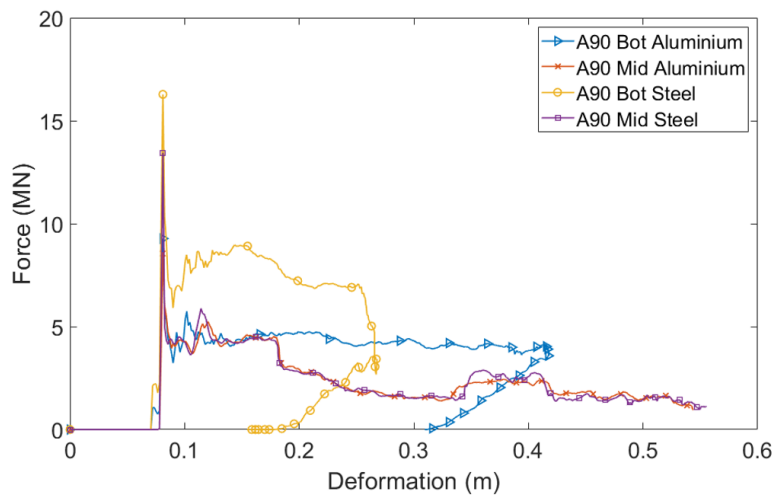
Figure 5.1: Force-displacement curves for A00 impact
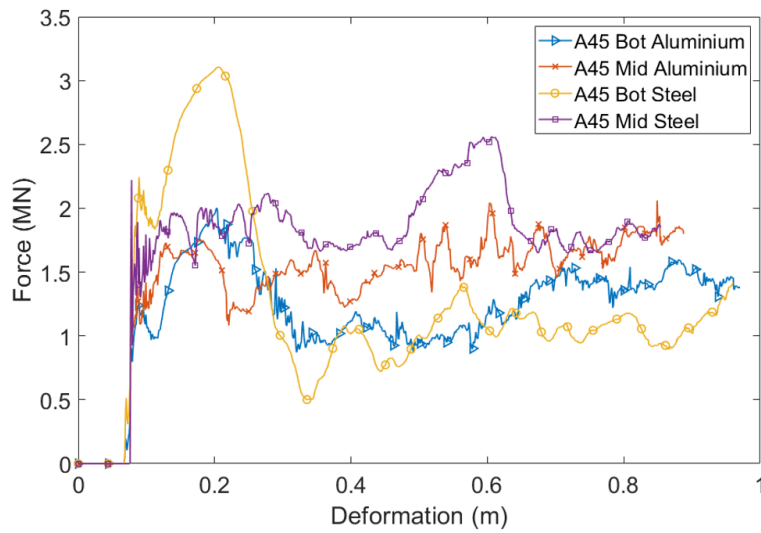
Figure 5.2: Force-displacement curves for A45 impact

Figure 5.3: Force-displacement curves for A90 impact

Case	Contact Force Steel Girder	Contact Force Aluminium Girder
A00 Bot	6.04 MN	3.95 MN
A00 Mid	7.98 MN	5.05 MN
A45 Bot	3.10 MN	2.00 MN
A45 Mid	2.56 MN	2.06 MN
A90 Bot	16.28 MN	9.28 MN
A90 Mid	13.45 MN	8.56 MN

Table 5.1: Maximum contact forces (MN)

Case	Steel Girder Deformation	Aluminium Girder Deformation
A00 bot	0.101m	0.91m
A45 bot	0.12m	0.64m
A90 bot	0.14	0.42

**Table 5.2:** Summary of deformations in bridge girder

5.1.2 Structural deformation and damage

The vertical impact location causes large variations in the stress distribution in the bridge girder and deformation of the containers. In all cases, the shipping container impact leads to plastic deformation in the aluminium and steel girder. Localized fracture occurs in the girder vertical plates and/or stiffeners on the inside of the girder panel for the aluminium girder. These stiffeners also seem to take high stress due to bending, especially from the bottom impacts. This because the density of the container floor is increased to account for the weight of the cargo inside the container. The floor beams contacts directly crushed against the girder side panel and induce a larger contact force in the impact region for all angles. For middle impact cases, the forces are transferred onto the diaphragms, which also fail locally in most cases as shown in Figures 5.8 - 5.10.

When impacting with the steel bridge girder, high stress still occurs at the impact zone in the bridge girder. The steel bridge girder shows the same deformation pattern as the aluminium bridge girder. However, the area and severity of the deformed region are much smaller compared with the aluminium bridge girder. Moreover, no fracture was observed in the steel bridge girder. This is because the high-strength steel used in the steel bridge girder has much higher yield stress than the aluminium material. The stress contour of the steel bridge girder in various impact scenarios is shown in Figures 5.5 - 5.7.
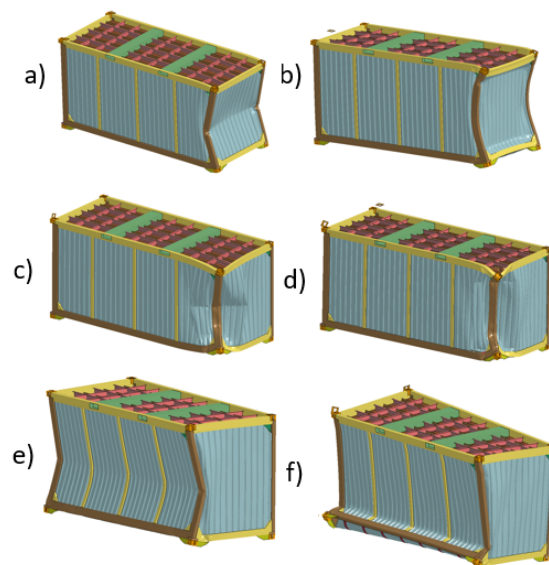

Figure 5.4: Figure 12. Deformed shipping containers. a) A00 Bot b) A00 Mid c) A45 Bot d) A45 Mid e) A90 Bot f) A90 Mid.
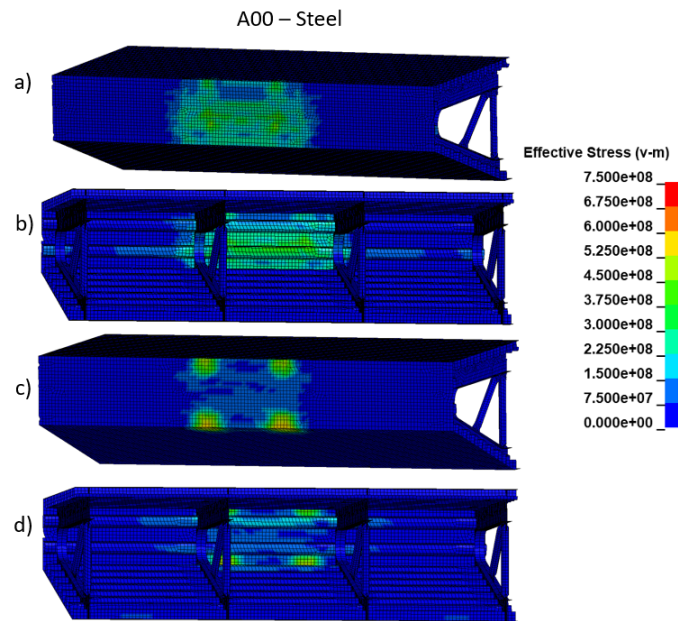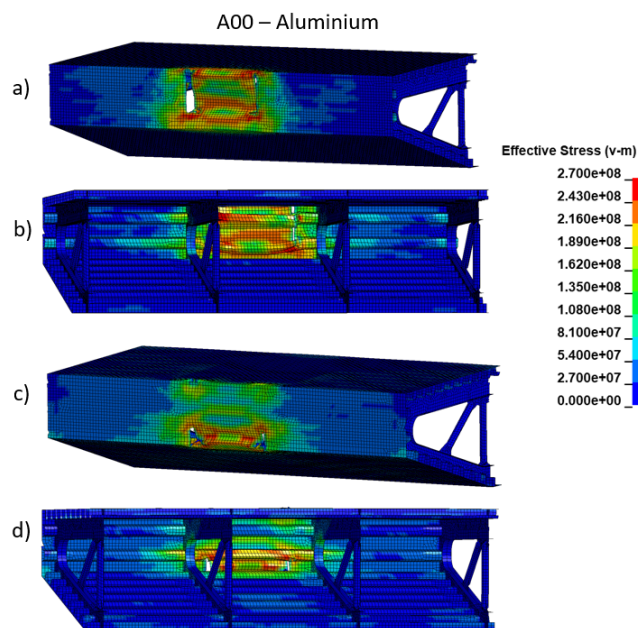
Figure 5.5: Stress contour on bridge girder, impact A00 with steel girder
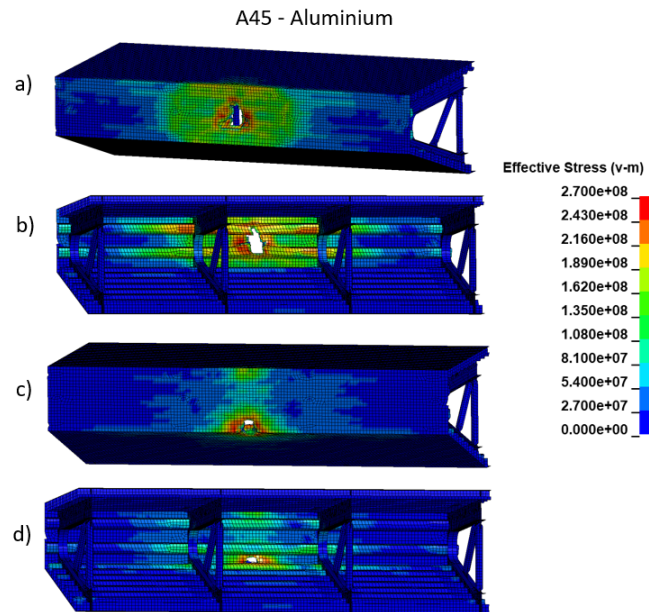a) A00 Bot b) A00 Bot Inside Girder c) A00 Mid d) A00 Mid Inside Girder
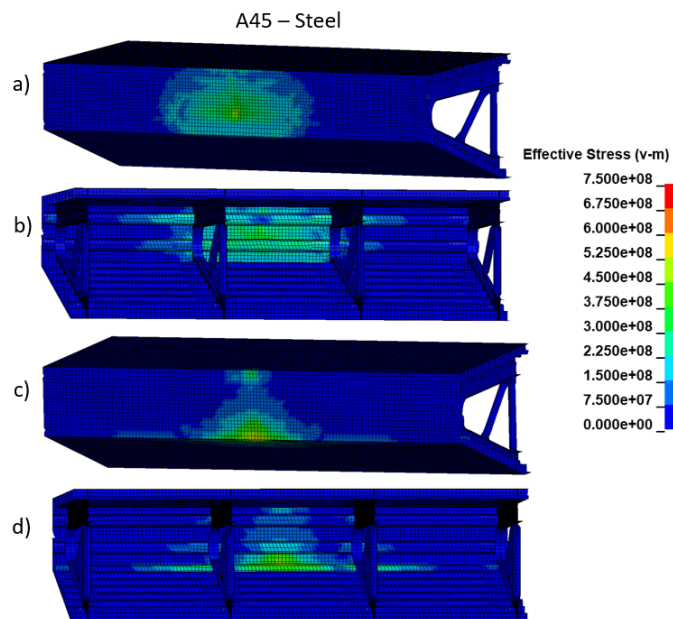
Figure 5.6: Stress contour on bridge girder, impact A45 with steel girder
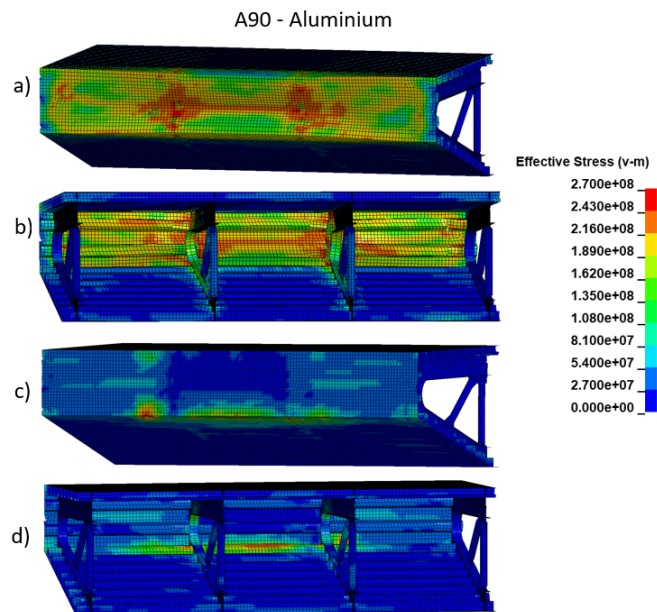a) A45 Bot b) A45 Bot Inside Girder c) A45 Mid d) A45 Mid Inside Girder
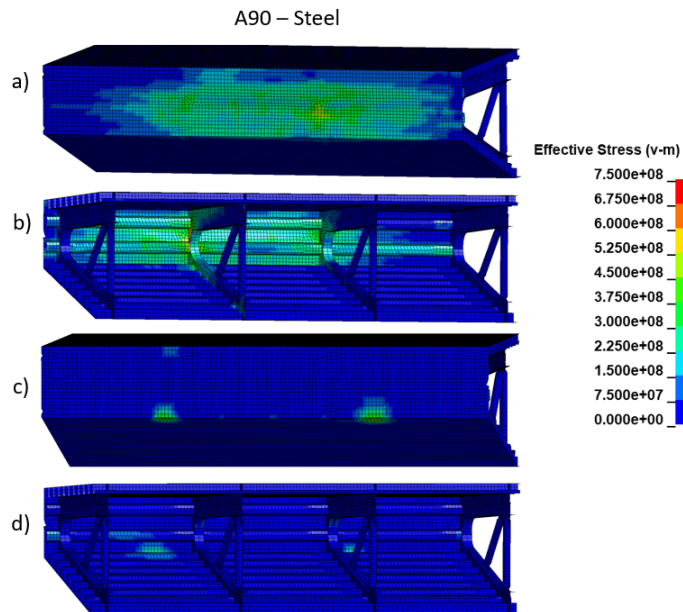
Figure 5.7: Stress contour on bridge girder, impact A90 with steel girder
a) A90 Bot b) A90 Bot Inside Girder c) A90 Mid d) A90 Mid Inside Girder

Figure 5.8: Stress contour on bridge girder, impact A00 with aluminium girder
a) A00 Bot b) A00 Bot Inside Girder c) A00 Mid d) A00 Mid Inside Girder

Figure 5.9: Stress contour on bridge girder, impact A45 with aluminium girder
a) A45 Bot b) A45 Bot Inside Girder c) A45 Mid d) A45 Mid Inside Girder

Figure 5.10: Stress contour on bridge girder, impact A90 with aluminium girder
a) A90 Bot b) A90 Bot Inside Girder c) A90 Mid d) A90 Mid Inside Girder

5.1.3   Energy dissipation

The energy dissipation of the shipping container in all collision scenarios is listed in Table 5.3. In all cases, the initial kinetic energy of the impacting container is 1.72 MJ. The container dissipates 32 % -81 % of the total impact energy when impacting with the aluminium bridge girder. The container has a low energy dissipation ratio for 45- and 90-degree bottom impact cases. For the 45-degree bottom impact case, the container corner fitting penetrates the girder side panel and results in large damage to the bridge girder. Similarly, the container induces plastic deformation over a large region in the 90-degree bottom impact case. For impact with the steel bridge girder, the shipping container can absorb around 80 % of the total energy in several cases. For other cases, the container dissipates more than 50 % of the total impact energy in all cases except for the 45-degree bottom case where 47 % of the total energy is absorbed by the container. It is therefore reasonable to assume a rigid girder when performing preliminary design of steel bridge girders against shipping container impact.

Case	Initial Kinetic Energy	Internal Energy	Rel. Energy Dissipation
A00 Bot Alu.	1.72 MJ	0.98 MJ	57 %
A00 Mid Alu.	1.72 MJ	0.95 MJ	55 %
A45 Mid Alu.	1.72 MJ	0.50 MJ	29 %
A45 Bot Alu.	1.72 MJ	0.71 MJ	41%
A90 Bot Alu.	1.72 MJ	0.55 MJ	32 %
A90 Mid Alu.	1.72 MJ	1.31 MJ	76 %
A00 Bot Steel	1.72 MJ	1.40 MJ	81 %
A00 Mid Steel	1.72 MJ	1.38 MJ	80 %
A45 Mid Steel	1.72 MJ	0.80 MJ	47 %
A45 Bot Steel	1.72 MJ	1.02 MJ	59 %
A90 Bot Steel	1.72 MJ	1.09 MJ	63 %
A90 Mid Steel	1.72 MJ	1.35 MJ	78 %

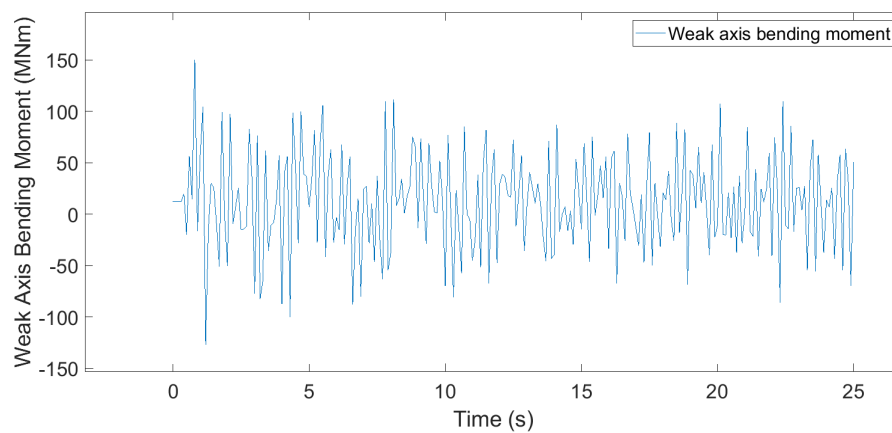**Table 5.3:** Energy dissipation in shipping containers.

5.2 Global Analysis

In this section the results from the global analysis is presented.

5.2.1 Section Moments
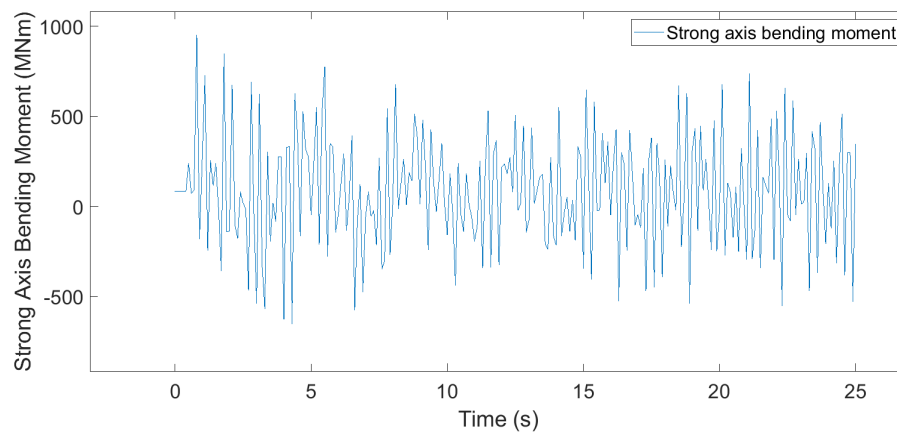
Figure 5.11: Strong Axis Bending Moment on High Bridge Span 5
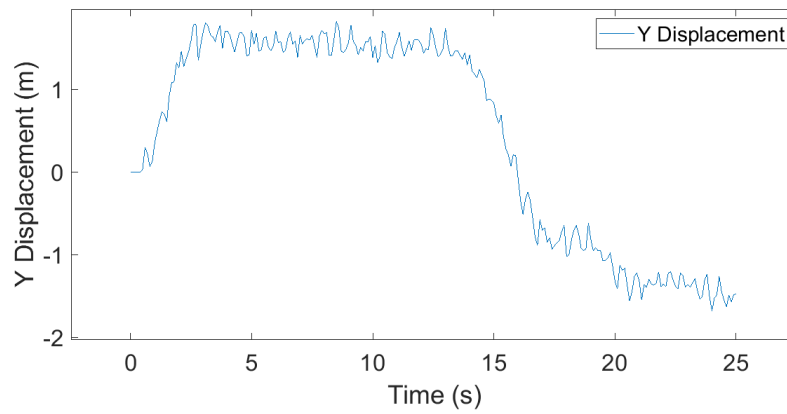

Figure 5.12: Weak Axis Bending Moment on High Bridge Span 5

Bending moment about the strong and weak axis at the impact location is presented in figure 5.11 and 5.12 respectively. Maximum values are presented in table 5.4. They showed that the six containers giving the impact results in significant moments on the bridge girder.

5.2.2   Displacement and Motions

Figure 5.13: Global Displacement on High Bridge Span 5
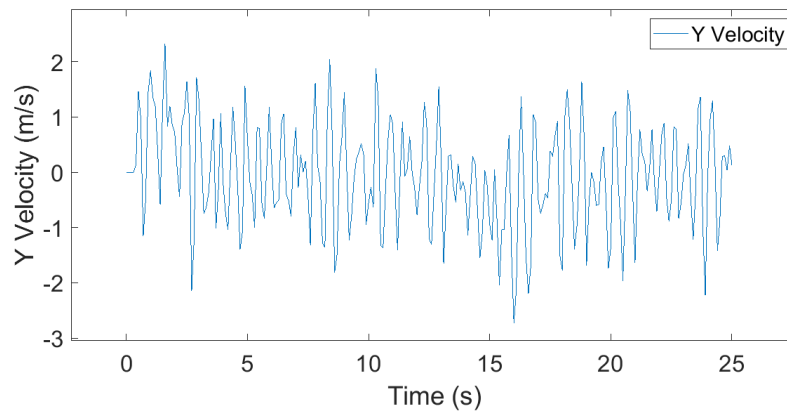
Figure 5.14: Global Velocity on High Bridge Span 5

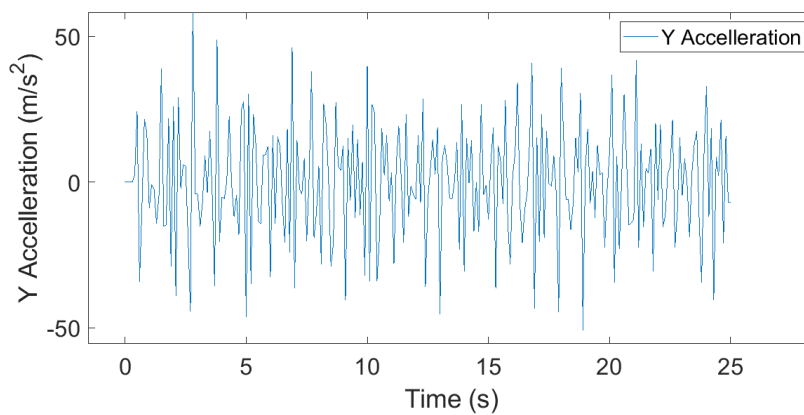**Figure 5.15:** Global Acceleration on High Bridge Span 5

	Maximum Values in Global Analysis
Axial Force	121.9 MN
Shear Force Strong	237.90 MN
Shear Force Weak	546.8 MN
Bending Moment Strong	946.1 MNm
Bending Moment Weak	150.3 MNm
Displacement	1.83 m
Velocity	2.69 m/s
Acceleration	62.83 m/s^2

Table 5.4: Summary of maximum values from global analysis

Girder displacement in the direction of impact (y-direction) is shown in figure 5.13. Similarly, the velocity and acceleration is also presented in the direction of impact in figure 5.14 and 5.15 respectively. The displacement and motions show a rapid acceleration of the girder, however, the velocity and displacement are rather low. This might be due to a rather short impact time. However, it can be observed that the impulse from the containers sets the girder in motion upon the impact and that the damping is rather low. The period in the girder velocity and acceleration is approximately 1.0s. This is not in the same range as the eigenperiod's in the reference report or from the developed model, which is good because it limits the possibility of dynamic amplification and resonance in the structure from wind, wave, and base excitation as seen in figure 5.16 below. The period for the displacement was further evaluated for a longer analysis time then displayed in figure 5.13, to check the period and is not shown in the results. The period was calculated to 31s. This period is close to the period of the first eigenmode in table 4.3. This indicates that dynamic amplification from wind and waves might occur post-impact.
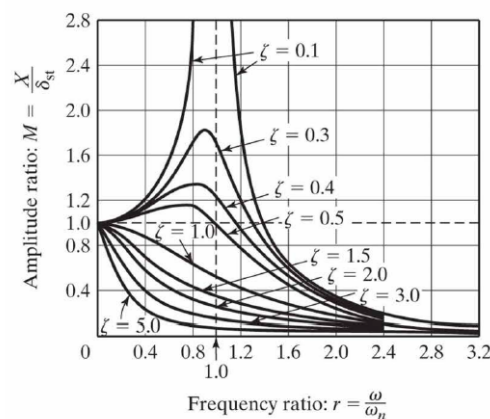
Figure 5.16: Dynamic Amplification factors for general 1 DOF systems [32].

Chapter 6

Discussions and Conclusions

6.1 Local Analysis

Contact force is highly dependent on container rigidity and impact location. It follows from the results that when an impacting object is less deformable, the contact forces increase. This is linked to crashworthiness. To design for ship collision, crashworthy design in terms of deformable bodies is hard to achieve. As neither structure should deform easily as that would compromise the global stability of both a ship and a bridge girder. This goes for shipping containers as well, as they are a means of protecting the cargo during transport. From the mid impacts, material in the bridge girder is less decisive due to large deformations in the shipping container. In this impact scenario, the rigidity of the container is lower than bridge girders constructed in either aluminium or steel. The bottom impacts however indicate that when forces are directly transferred, the aluminum girder deforms a lot more, this was expected due to the lower E-modulus and yield stress.

As mentioned in the introduction it has been shown in previous studies that it is possible to meet all the relevant design criteria for the bridge, including global stability, local stability, fatigue, ultimate global stress levels, and serviceability deflections [42]. However, the results from this study raise questions about the accident limit state. Aluminum girders might have to be used for suspension bridges where the water to bridge deck height eliminates the possibility of any ship collision. Investigation of thicker plates or different designs to optimize for the local damage has not been done and might yield different results. In addition, it should also be noted that this force level considers only one container on the ship deck. For example, with a ship width of 25 m, it is easy to parallel place six rows of containers on the ship deck. This amounts the maximum impact force to around 60 MN for the aluminium girder and 96 MN for the steel girder

if the highest contact force applies, which is substantial to bridge girders. Stacking and interlocking of containers might also change the force-displacement relationship observed. Moreover, such high-impact forces should therefore not be ignored during the design of bridge superstructures where the possibility of a collision is present. In the case of the E39 Bjørnafjorden crossing, the floating part of the bridge will have a low water clearance, such that drifting ships in this area will not stay clear of the bridge girder or pontoons. The force considered can also be even larger, the containers were given initial velocity and simulations showed rapid deceleration and even a little "bounceback" at the end. Large inertia of a container ship would cause a slower deceleration than obtained in this study. This would probably lead to further crushing of the shipping containers, higher contact force, energy dissipation, and damage.

Simulations showed from 32% to 81% energy dissipation in the shipping containers, this means that a rigid container assumption would be non-conservative in terms of energy dissipation In addition, the containers in the simulation are empty inside, but the loading on the floor beams are considered. In the case of rigid cargo, such as cars, engines, building materials, raw rocks etc. The contact force will likely increase. In a design situation, shipping container impact to impact with or without deckhouse impact will likely generate lower impact force as opposed to a bow collision where the entire mass of the ship with cargo is considered.

Further work should investigate global failure and response due to shipping container impacts. Investigations with freight filled container for impacts with the constant or slow deceleration of the velocity is also recommended as well as impact with several stacked containers. According to NPRA hand-book N400 states that local collapse is acceptable, provided the global stability can be maintained to prevent total collapse. For the bridge girder, this means that the bridge girder can be damaged causing a reduced stiffness if the bridge can sustain a post-impact phase according to NS-EN 1991-1-7.

6.2 Global Analysis

The global response of the bridge due to shipping container impact has been studied in this part by building an FE-model from scratch based on the available drawings and reports from NPRA. The model is a simplification of the one described in NPRA's report. One case with a head-on collision has been considered in the first span of the south side of the bridge. The analysis showed a maximum bending moment of 946 MNm and a shear force of 238 MN. Comparing the values obtained in the model with NPRA's report on ship collision [51] the bending moment and displacement are in a lower order of magnitude in this model than for the investigated ship collision in the NPRA report [51], although

the total impulse was assumed to be a bit larger. In this model, a moment of 946 MNm is observed, compared to a maximum of around 2 GNm in the report. The impulse load is 20 MN in the NPRA report and 6x8MN in the studied model. Similarly, the maximum displacement is around 20 meters in the report, compared to 1.09 m in the model. This might suggest that several containers on a line with "smaller" force-displacement values than a ship collision do not "sum up" to the same order of magnitude of a ship collision. In addition, the impact in the NPRA report and this thesis are in different locations on the bridge. Also, the force-deformation relationship in figure 4.15 has a peak at 8 MN, but the average contact force lies around 4 MN. This might yield less of an impact force than initially assumed, but it does not entirely explain the discrepancy in the results.

Caution should also be taken in the choice of the force-displacement curve for the shipping containers. The curve used is for one container, with only initial velocity impacting the girder. The effect from stacking and interlocking as well as inertia forces from the container ship itself is not taken into account and might yield an entirely different force-displacement curve, that would change the results as mentioned in chapter 6.1 above.

It should also be noted that the modeled bridge is a simplification of the one used in the NPRA's reports and the modal analysis does correlate satisfactorily with the reference. However, it was hard to pinpoint any obvious errors in the modeling, and further detailing of cross-sections, columns, tension cables, and mooring lines were carried out in greater detail than initially planned. However, there were still simplifications of the model and along with hand-calculation of stiffness properties, discrepancies might occur. In addition, modification of pontoon mass and added mass is also expected to affect the eigenmodes [51] and has not been studied and modified in detail. However, significant learning outcome regarding bridge construction and finite element modeling was obtained in this is part of the work. In order to work further with this global model, a proper modal analysis is recommended, in order to verify that the model is indeed accurate.

6.3 Conclusion

6.3.1 Local Analysis

Numerical simulations of loaded shipping containers impacting steel and aluminium bridge girder with various angles have been performed as a local analysis by building an FE-model in LS-DYNA:

1. A comparison between impact with and without DIF for yield stress at certain strain rates has been performed. The comparison showed that the strain rate has a minor effect for 6005-T6 Aluminium in collision simulation. This matches the conclusion of [20].

2. The results show reduced contact force compared to a steel girder due to increased deformation and initiation of fracture in the aluminium girder, which leads to higher energy dissipation. Stress development in the aluminium girder is large, and local failure is observed for all cases to various degrees.

3. In the cases where the middle of the shipping container impacts and deformations are large, the material type seems to play a minor role. This is because the middle impact cases involve a larger area in the girder which redistribute the impact force.

4. The shipping containers generally dissipate the majority of the kinetic energy when impact by the steel bridge girder. The energy dissipation varies when impacting the aluminium girder due to the fracture in the girder.

6.3.2 Global Analysis

The force-displacement relationship for a head-on collision for a steel girder and container, namely A00 Mid collision has been used to simulate an impact from 6 containers side by side on a global model.

3The global Orcaflex model was built from scratch, based on the available drawings and reports from NPRA. The results show significant development of axial and shear force as well as bending moment. No failure was observed. The dynamic response showed to be quite slow, and a small displacement of 1.09 meters was observed. This was a lot smaller than in the already existing NPRA's reports on ship collision studies. The period for velocity and acceleration did not imply resonance behavior from wind and wave load frequencies. However, the displacement/bridge motion implies a risk of dynamic amplification from wind av waves post-impact. The

modal analysis did not correlate satisfactorily with the already existing NPRA's report. Presumably due to lack of modification of pontoon masses, added masses as well as simplifications in the modeling process which challenges the validity of the results in this part of the work.

6.4 Recommendation on further work

Investigations with freight filled container for impacts with the constant or slow deceleration of the velocity has been recommended as well as impact with several stacked containers. According to the NPRA handbook N400 states that local collapse is acceptable, provided the global stability can be maintained to prevent total collapse. For the bridge girder, this means that the bridge girder can be damaged causing a reduced stiffness if the bridge can sustain a post-impact phase according to NS-EN 1991-1-7. Analysis with the reduced stiffness properties is an interesting project that is an entirely different project in itself. Further could also include a 100-year environmental loading condition, this could be done in the built Orcaflex model and should also be conducted as the period of the free vibrations post-impact showed to be close to the first eigenmode.

In addition, analysis of the other structural parts such as columns, pontoons, and the tower for either environmental or accidental loads would also be recommended along with further development of the global model, reducing the number of simplifications. In addition, the global shipping container impact analysis was conducted for the steel girder because there was a local failure in the aluminium girder. It could also be interesting to see the response of global analysis for shipping container impact on the aluminium girder.

List of Figures

List of Tables

Bibliography

[1] S. Vegvesen, "Fergefri e39," Available at "https://www.vegvesen.no/vegprosjekter/ferjefriE39" (2021/01/05).

[2] ——, "Ferjefri e39- presentasjon fagseminar," Available at "https://www.vegvesen.no/_attachment/2399116/binary/1275152?fast_title=Presentasjon" (2018/06/16).

[3] ——, "Fjordkrysning bjørnafjorden," Available at "https://www.vegvesen.no/Europaveg/e39stordos/fjordkryssing-bjornafjorden" (2020/09/10).

[4] S. Lewis, "The 10 longest floating bridges in the world," Available at "https://www.enr.com/articles/44013-the-10-longest-floating-bridges-in-the-world" (2018/02/20).

[5] M. M. Lwin, *Floating Bridges*. Boca Raton, Florida, USA: CRC Press LLC, 2000.

[6] S. Tattoni, "Pontoon bridges," Milano, Italy, 2016.

[7] P. O. Øiseth, "Floating suspension bridges," Available at "https://www.ntnu.edu/kt/research/dynamics/research/long-span/floating-suspension" (2021/01/07).

[8] P. A. Rønnquist, "Submerged floating tube bridges," Available at "https://www.ntnu.edu/kt/research/dynamics/research/long-span/submerged-floating-tube" (2021/01/07).

[9] Railsystem.net, "Submerged floating tunnel," Available at "http://www.railsystem.net/submerged-floating-tunnel/" (2015).

[10] Z. L. C. D. Yanyan Sha, Jørgen Amdahl, "Simulation of shipping container impact with bridge girders," 16 November 2020.

[11] K. L. Yanyan Sha, Jørgen Amdahl, "Design of steel bridge girders against ship forecastle collisions," 18 June 2019.

[12] J. A. Yanyan Sha, "Local and global responses of a floating bridge under ship–girder collisions," 2019.

[13] Z. C. Xuan Guo, Chen Zhang, "Dynamic performance and damage evaluation of a scoured double-pylon cable-stayed bridge under ship impact," 2020.

[14] H. F. Tian Li, "Numerical simulation for progressive collapse of continuous girder bridge subjected to ship impact," 2014.

[15] S. H. N. J. K. P. J. K. S. Y. H. K. Bo Gyeong Jung, Sung Woo Jo, "Experimental and numerical studies on nonlinear impact response of deck structures subjected to dropped objects," 2016.

[16] D. K. P. B. G. J. X. H. J. K. P. Ki Jong Kim, Jong Hwan Lee, "An experimental and numerical study on nonlinear impact responses of steel-plated structures in an arctic environment," 2016.

[17] O. S. Hagbart S.Alsos, Jørgen Amdahl, "On the resistance to penetration of stiffened plates, part ii: Numerical analysis," 2009.

[18] N. G. A. Deb, M. Raguraman and V. Madhu, "Numerical simulation of projectile impact on mild steel armour plates using ls-dyna: Part i: Validation," 2008.

[19] O. H. M. L. S. Dey, T. Børvik, "On the influence of constitutive relation in projectile impact of steel plates," 2007.

[20] C. G. S. B. Liu, R. Villavicencio, "Shear and tensile failure of thin aluminium plates struck by cylindrical and spherical indenters," 2015.

[21] C. G. S. R. Villavicencio, L. Sutherland, "Numerical simulation of transversely impacted, clamped circular aluminium plates," 2010.

[22] T. N. J. L. P. M. D. R. Damith Mohotti, Muneeb Ali, "Out-of-plane impact resistance of aluminium plates subjected to low velocity impacts," Victoria - Australia, 2013.

[23] M. P. R. W. Robert Cook, David Malkus, *Concepts and applications of finite element analysis*, fourth edition ed.   University of Wisconsin - Madison: John Wiley Sons, INC, 2001.

[24] O. S. H. Jisheng Qin, Bjørn Holmedal, "A combined isotropic, kinematic and distortional hardening model for aluminum and steels under complex strain-path changes," Available at "https://ntnuopen.ntnu.no/ntnu-xmlui/bitstream/handle/11250/2491299/Cristin+storage.pdf?sequence=1".

[25] "Ls-dyna keywords user manual volume 1," Livermore Software Technology Corporation, California, User Manual, 2017.

[26] LSTC, "Hourglass (hg) modes," Available at "https://ftp.lstc.com/anonymous/outgoing/support/FAQ_docs/hourglass.pdf" (2021/02/08).

[27] DynamoreGmbH, "Time integration, equation of motion," Available at "https://www.dynasupport.com/tutorial/ls-dyna-users-guide/time-integration" (2021/01/13).

[28] Dynasupport, "Mass scaling," Available at "https://www.dynasupport.com/howtos/general/mass-scaling" (2021/02/15).

[29] DynamoreGmbH, "How contact works," Available at "https://www.dynasupport.com/tutorial/contact-modeling-in-ls-dyna/how-contact-works" (2021/01/13).

[30] N.-H. Kim, "Finite element analysis of contact problem," Available at "https://mae.ufl.edu/nkim/egm6352/Chap5.pdf" (2021/01/13).

[31] DynamoreGmbH, "Contact types," Available at "https://www.dynasupport.com/tutorial/contact-modeling-in-ls-dyna/contact-types" (2021/01/13).

[32] S. S. Rao, *Mechanical Vibrations*, fifth edition ed. University of Miami -Florida: Pearson, 2011.

[33] D. R. William Callister, *Materials science and Engineering*, ninth edition ed. Wiley Sons Asia: Wiley, 2014.

[34] N. Dr.Ing Olav Olsen, "K12 – ship impact, bridge girder," Available at "https://vegvesen.brage.unit.no/vegvesen-xmlui/bitstream/handle/11250/2660284/SBJ-33-C5-OON-22-RE-015-0%20K12%20-%20Ship%20impact%2c%20Bridge%20girder.pdf?sequence=1&isAllowed=y" (2019/08/15).

[35] "Ls-dyna keywords user manual volume 2," Livermore Software Technology Corporation, California, User Manual, 2017.

[36] J. A. M Storheim, "On the sensitivity to work hardening and strainrate effects in nonlinear fem analysis of ship collisions," 2017.

[37] "Eurocode 1 - actions on structures - part 1-7: General actions - accidental actions," European Committee for Standardization, Brussels, Standard, Jul. 2006.

[38] "Norsok standard n-003:2016 actions and effects," Norwegian Oil and Gas Association and The Federation of Norwegian Industries, Oslo, Standard, 2016.

[39] T. Abbey, "Verification vs. validation in relation to fea," Available at "https://www.digitalengineering247.com/article/verification-vs-validation/" (2015/03/15).

[40] N. M. Veikos, "Verifying your finite element analysis results," Available at "https://www.engineering.com/story/verifying-your-finite-element-analysis-results" (2018/01/25).

[41] A. Dr.Ing Olav Olsen, Norconsult, "K7- bjørnafjorden end-anchored floating bridge summary report," Available at "https://www.vegvesen.no/Europaveg/e39stordos/fjordkryssing-bjornafjorden/rapportar/_attachment/2336225?_ts=164174237c8&fast_title=K7+Bj%C3%B8rnafjorden+endeforankra+flytebru.pdf" (2019/08/15).

[42] Hydro, Leirvik, NTNU, DR.Olav Olsen, "Langenuen suspension bridge aluminium bridge girder alternative," Available at "https://www.shapesbyhydro.com/globalassets/shapes/material-properties/langenuen-suspension-bridge-aluminium-girder-alternative.pdf" (2021/02/15).

[43] Nedal-Aluminium, "Alloy data sheet en-aw 6005a," Available at "https://www.nedal.com/wp-content/uploads/2017/11/Nedal-alloy-Datasheet-EN-AW-6005A.pdf".

[44] AAS-Jakobsen, COWI, Multiconsult, "Preferred solution, k12 - appendix a drawings binder," Available at "https://vegvesen.brage.unit.no/vegvesen-xmlui/handle/11250/2660039" (2021/02/15).

[45] ——, "Preferred solution, k12 – appendix m - mooring system," Available at "https://vegvesen.brage.unit.no/vegvesen-xmlui/handle/11250/2659829" (2021/02/15).

[46] ——, "Preferred solution, k12 – appendix f global analyses - modelling and assumptions," Available at "https://vegvesen.brage.unit.no/vegvesen-xmlui/handle/11250/2660044" (2021/02/15).

[47] ——, "Preferred solution, k12 – appendix l - design of cable stayed bridge and abutments," Available at "https://vegvesen.brage.unit.no/vegvesen-xmlui/handle/11250/2660004" (2021/02/15).

[48] "Eurocode 9 - : Design of aluminium structures," European Committee for Standardization, Standard, Jul. 2007.

[49] J.-P. Rodrigue, "Fuel consumption by containership size and speed," Available at "https://transportgeography.org/contents/chapter4/transportation-and-energy/fuel_consumption_containerships/" (2020).

[50] S. Z. Yong Zhu, Hua Yang, "Dynamic mechanical behavior and constitutive models of s890 high-strength steel at intermediate and high strain rates," 2020.

[51] AAS-Jakobsen, COWI, Multiconsult, "Preferred solution, k12 – appendix j - ship collision - part 1," Available at "https://vegvesen.brage.unit.no/vegvesen-xmlui/handle/11250/2660035" (2021/02/15).

Appendix A

Response of aluminium bridge girders subjected to shipping container impacts

S.M. Dyrkolbotn & Y. Sha
Department of Mechanical and Structural Engineering and Materials Science, University of Stavanger, Stavanger, Norway.

Z. Liu
Aker Solutions AS, Trondheim, Norway.

ABSTRACT: Novel aluminium bridge decks have recently been proposed as an alternative to traditional steel bridge decks. Aluminium structures can meet all design criteria for bridges and have the advantages of low density and high corrosion resistance compared with steel structures. Regardless of bridge girder material, one critical issue in design is to ensure the safety of bridge girders under accidental ship superstructure collisions. Such collision accidents can occur in earthquake or tsunami inundation, due to ship maneuvering errors or mechanical failures. The bridge girder strength against ship collision load should be carefully checked to avoid large local damage in the impacted region and further degradation of global bridge safety. Some initial studies have been conducted for ship deckhouse and forecastle impacts with bridge girders. However, bridge decks are also under the impact of stacked shipping containers on the container ships. Considering the lower elastic modulus and ductility of aluminium material compared with steel, aluminium bridge girders may be more vulnerable to collision loads. This study aims to numerically investigate the local structural response of aluminium bridge girders under shipping container impacts. Finite element models of an aluminium bridge deck of a suspension bridge and a 20 ft standard shipping container are developed in LS-DYNA. The strain rate effect of aluminium girder under container impact is first discussed. The impact force, structural damage and energy dissipation during the collision are compared between aluminium and steel bridge girders. The effects of impact angle and vertical location are also discussed.

1 INTRODUCTION

The Norwegian Public Roads Administration (NPRA) is planning to improve the coastal highway E39, guided by the national transportation plan issued in 2017. The overlying objective is to cut the travel time from Kristiansand to Trondheim by half. Along the route, eight fjords that are currently operated with ferry connections will be replaced by bridges or tunnels. As the fjords are wide and deep, floating bridges or submerged floating tunnels must be constructed. The first floating bridge will be built in Bjørnafjorden and the concept as shown in Figure 1 is proposed for this fjord. Traditionally, the bridge decks of large span bridges are mainly constructed with steel. Recently, novel aluminium bridge decks have been proposed for the floating bridge. It has been shown that an aluminium bridge deck can satisfy the structural requirements for highway suspension bridges by NPRA (2020), meanwhile have the advantages of low density and high corrosion resistance compared with steel structures.

Figure 1. Proposed concept for Bjørnafjorden crossing.

In the past years, an increasing number of impact accidents due to over height ship superstructures and cargos have been reported. Several studies have been performed on ship superstructure and shipping container collision with steel and reinforced concrete bridge decks by Sha and Amdahl (2019, 2020). For aluminium bridge decks, the dynamic response subjected to accidental collisions has not been well documented. The local damage in the aluminium may be more severe than that in steel decks due to low elastic modulus, yield stress, and ductility. Liu et al

(2012) and Villavicencio et al (2012) investigated the response of stiffened aluminium plates subjected to rigid indenter impacts. It is found good agreement of the experimental testing and non-linear finite element models in LS-DYNA with appropriate contact modelling and material models when analysing aluminium structures.

Moreover, the relatively lighter aluminium decks will also endure larger global motions under impacts. This study aims to conduct numerical investigations on the dynamic response of aluminium bridge girders subjected to shipping container impacts. Only local structural damage is reported in this study. The global response of the whole floating bridge is currently under investigation and will be reported in further study.

In this study, finite element (FE) models of an aluminium bridge girder and a 20ft standard shipping container are developed. Several numerical impact simulations are performed to investigate the effect of strain rate, impact angle, and impact location. The difference in impact response between steel and aluminium decks are also discussed.

2 FINITE ELEMENT MODELS

2.1 Bridge Girder

The finite element model of a bridge girder section is shown in Figures 2. It is a typical steel girder design for large span bridges. The girder cross-section is 27 m in width and 4 m in height. The girder outer plate thickness is 14 mm in the top and bottom panels, and 12 mm in the sidewalls. The girder panels are strengthened by 8 mm thick hat type stiffeners. The height of the hat stiffener supporting the top flange is 285 mm and the flange width is 150 mm. The flange width and stiffener height for side and bottom panels are 230 and 350 mm respectively. In the bottom flange, there are also L-type stiffeners with a thickness of 11 mm and a height of 280 mm. The top flange width and thickness are 50 mm and 30 mm respectively. The girder has an integrated design throughout the whole cross-section. The edge plates are supported by diaphragms with 4 m spacing that are connected on the top and bottom plates. The heights of the diaphragms supporting the bottom and the top panels are 600 mm and 1000 mm respectively. The diaphragm flange width is 280 mm. The diaphragms are supported by vertical trusses with a circular hollow cross-section. The trusses have a thickness of 10 mm and a diameter of 220 mm. All parts in the bridge girder were modelled using shell elements. The mesh size of the bridge girder is 100 mm. To reduce computational efforts, 7 m of the total 27 m width of the cross-section was modelled in the numerical simulations as seen in Figure 5. The steel girder and the

aluminium girder have the same geometric design as shown in Figure 2.
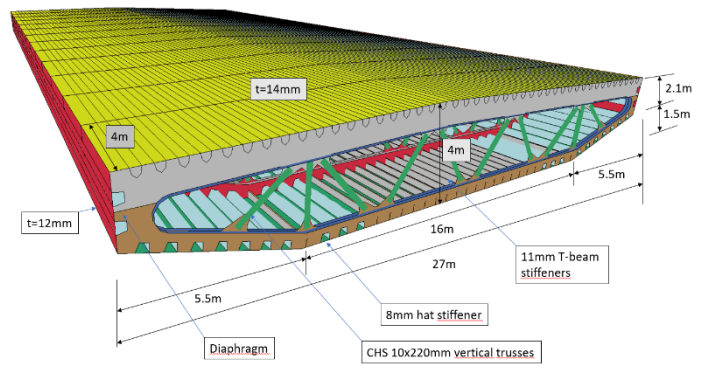
Figure 2. FE model of the bridge girder.

2.2 Shipping container

The FE model of the shipping container was obtained from Sha et al. (2020) based on a standard 20-ft shipping container and is shown in Figure 5. The dimensions are 5.97 m in length, 2.43 m width and 2.82 m depth. The frame structure is made of top and bottom rails, corner posts and fittings, and transverse and longitudinal beams. In addition, there are corrugated front and side panels as well as floors on the top and bottom. The entire container was meshed with shell elements. The minimum mesh size is 20 mm in the shipping container. Details of the model can be referred to Sha et al. (2020).
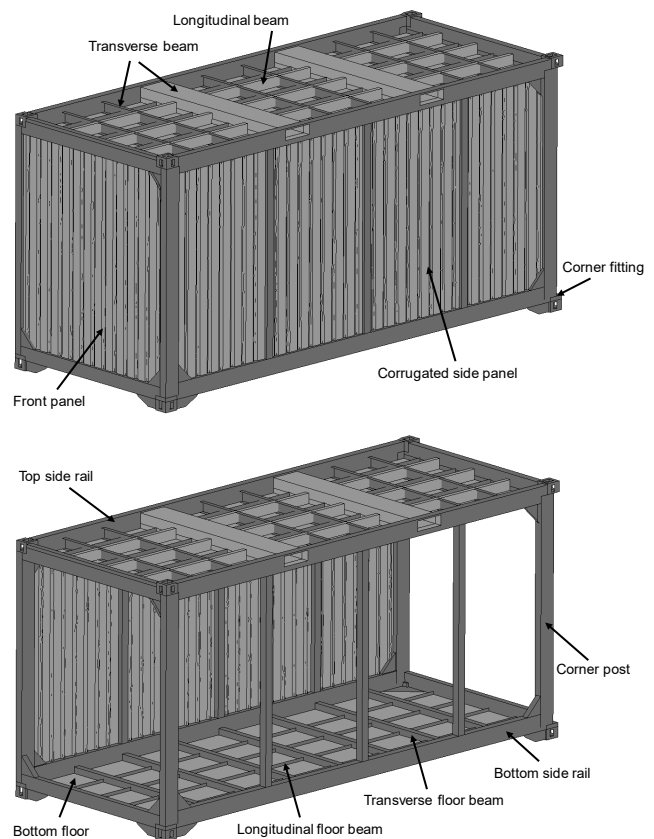
Figure 3. Finite element model of standard 20-ft. Shipping container (Sha et al. 2020).

2.3 Material and contact modelling

The material parameters of the aluminium bridge girder are described in Table 1. The aluminium alloy 6005A-T6 is the same as the aluminium material used in the Languenuen aluminium bridge concept (NPRA 2020). The material model MAT_ PIECEWISE_ LINEAR_ PLASTICITY (MAT24) in LS-DYNA was used to model the aluminium material. The stress-strain curve of the aluminium material is shown in Figure 4 (Standard 2007). A fracture strain of 0.08 was used in the simulation. In addition, the strain rate effect is considered by using the dynamic increase factor (DIF) to scale the yield stress for corresponding strain-rate values. This is further explained in Section 3.2. The heat-affected zone was not considered in the study as the bridge girder section will be extruded without welding in the longitudinal direction. The same modelling technique was used for the steel bridge girder with grade S420. The steel in the shipping container is S355 steel which was also modelled with the material model MAT24. To simulate the freight inside the containers, the floor beams were given an artificial density such that the total weight of the shipping container was 34.4 ton. All material parameters are listed in Table 1.

The interaction between the bridge girder and the shipping container is considered by using the contact function in LS-DYNA. The keyword CONTACT_AUTOMATIC_SURFACE_TO_SURFACE was used. The internal parts in the girder and container such as stiffeners, transverse beams, panels, floors and corner posts might also deform significantly. These interactions were included using CONTACT _AUTOMATIC _SINGLE_SURFACE. The dynamic and static friction coefficients were set to 0.3

Table 1. Material properties for steel and aluminium

Material	Yield Stress (MPa)	Failure strain	Elastic Modulus (GPa)	Density (kg/m³)
6005-T6 Aluminium	205	0.08	70	2700
S420 Steel	420	0.20	210	7850
S355 Steel	355	0.27	210	7850
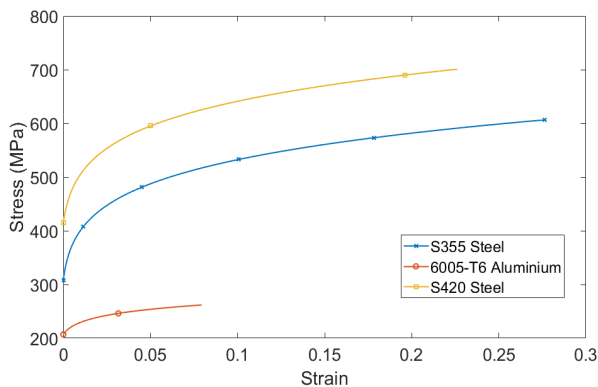
Figure 4. Stress-strain curves for steel and aluminium

3 NUMERICAL SIMULATIONS

3.1 Simulation setup

In the simulation, the container was given an initial velocity of 10 m/s at three different angles, i.e. 0, 45 and 90 degrees which are named Case A00, A45 and A90 respectively. In addition, two impact height was considered where the middle wall and bottom floor impacts against the bridge girder and they are referred to mid and bot cases. The six simulation cases are listed in Table 2 and the two impact locations are illustrated in Figure 5. In all simulations, the impact velocity is 10 m/s.

Table 2. Case Description

Case	Impact Angle	Impact Location
A00_Bot	0	Bottom floor
A00_Mid	0	Mid-wall
A45_Bot	45	Bottom floor
A45_Mid	45	Mid-wall
A90_Mid	90	Bottom floor
A90_Bot	90	Mid-wall
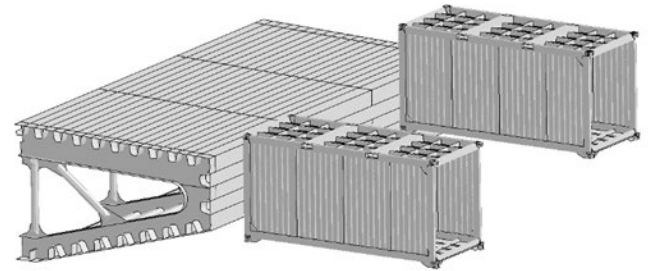
Figure 5. Illustration of two impact scenarios. To the left: A00_Mid. To the right: A00_Bot.

3.2 Strain rate effect

The strain rate effect has been extensively studied for steel structures in ship collision accidents. It is well recognized that strain rate can increase the yield stress of steel materials under a high loading rate. However, the fracture strain will also reduce at the same time. For aluminium, the effect of strain rate varies depending on the type and content of the alloyed material. In this study, numerical simulations were first conducted to explore the strain rate effect of 6005-T6 aluminium in ship collision simulations. To account for the strain rate, dynamic increase factor (DIF) was used to scale the stress-strain relationship at the corresponding strain rate. The results with strain rate are compared with the benchmark case without DIF using the stress-stress curves from Figure 4. DIF used in this study was obtained from Zhu et al. 2020 for S355 and S420 steel and Mohotti et al. 2013 for aluminium. The DIF curve for S355 steel which is used for the shipping container is steeper than those used for the 6005-T6 aluminium and S420 steel.

Figures 6-8 show the comparison of force-displacement curves with and without strain rate for different

impact scenarios. For A90-bot cases, it is observed that including strain rate results in slightly early fracture compared with the base case. For other impact scenarios, strain rate almost has no effect on the force-deformation curve. However, the strain rate is nevertheless considered for all materials in the simulations presented in Section 4.
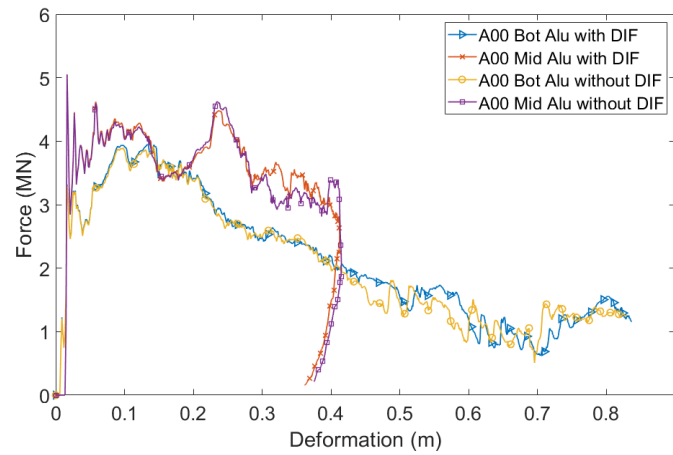
Figure 6. Force-displacement curves for A00 with and without strain rate.
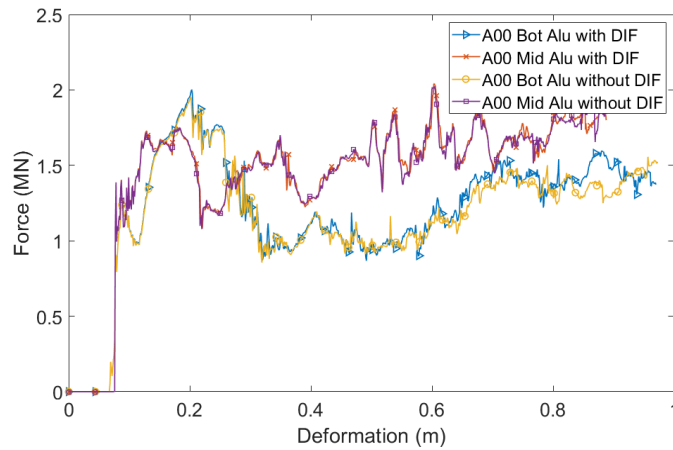
Figure 7. Force-displacement curves for A45 with and without strain rate.
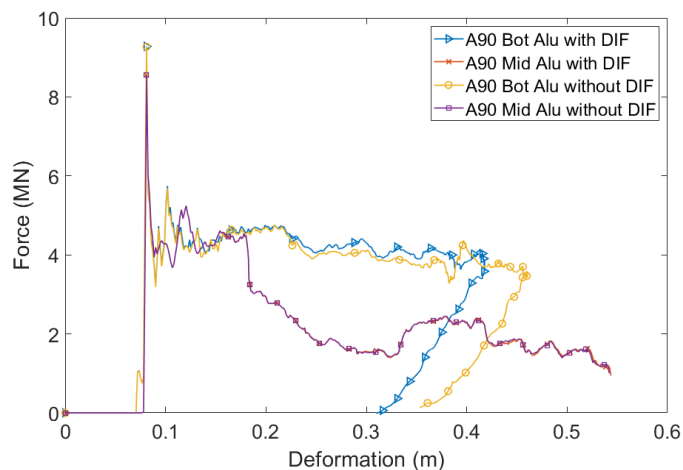
Figure 8. Force-displacement curves for A90 with and without strain rate.

4 COMPARISON OF ALUMINIUM AND STEEL BRIDGE GIRDERS

Container impact simulations were conducted for both the aluminium and steel bridge girders. The impact force, structure deformation, and energy dissipation were compared between the girders with the two different materials.

4.1 Force-displacement curve

The force-displacement curves for shipping container impact with steel and aluminium bridge girders are first compared in Figures 9-11 for three impact angles. It can be observed that relatively vertical impact location has a significant effect on the impact response for all impact angles regardless of girder material. For mid-wall impacts, the instantaneous peak force upon impact is higher for the steel bridge girder than the aluminium girder as the steel girder induces larger deformations in the container than the aluminium girder. After the initial contact, the force-displacement curves are in the same range for both steel and aluminium bridge girders. This is because the structural damage is mainly in the shipping container as shown in Figure 12. Very limited damage occurs in the bridge girder regardless of the girder material. This suggests that for the mid-impacts, the material properties of the girder play a minor role as long as the girder has a higher strength than the container.

For the bottom impact cases, the first peak of impact force is still higher when the container collides with the steel girder than with the aluminium girder. After that, the force-displacement curves for steel and aluminium bridge girders show large derivations which are different from mid-wall impact cases. When impacting with the steel bridge girder, the first plateaux in the force-displacement curves are larger than those of the aluminium bridge girder. This is because the steel bridge girder has higher strength and induces larger deformation in the container. Meanwhile, the span of the plateau in the force-displacement curve is shorter for the steel girder compared with the aluminium girder due to lower ductility.

For 0- and 90-degree middle impact cases, the shape of the force-displacement curves are quite similar. In these cases, the force level is determined by the bending and membrane of the two corner posts in the container as shown in Figure 12. For 45-degree cases, only one corner post was involved in the deformation process. For 0- and 45-degree bottom impact cases, the container corners penetrate the vertical side panel of the aluminium girder and thus result in a reduction of the impact force. For 90-degree impact, two girder diaphragms were engaged due to a large contact area with the container side panels. Thus, no fracture was observed in this case but the aluminium girder endures large deformation in the side panel. Table 3 shows that the maximum impact force of steel girder is always larger than the aluminium girder for all impact scenarios. The deformation in the steel bridge

girder is however smaller than that of the aluminium girder for bottom impact cases as shown in Table 4. Girder deformations for middle impact cases are very small and thus are not listed in the table.

Table 3. Maximum impact forces (MN).

Case	Steel Girder	Aluminium Girder
A00_Bot	6.0	4.0
A00_Mid	8.0	5.1
A45_Bot	3.1	2.0
A45_Mid	2.6	2.1
A90_Bot	16.3	9.3
A90_Mid	13.5	8.6

Figure 9. Force-displacement curves for A00.
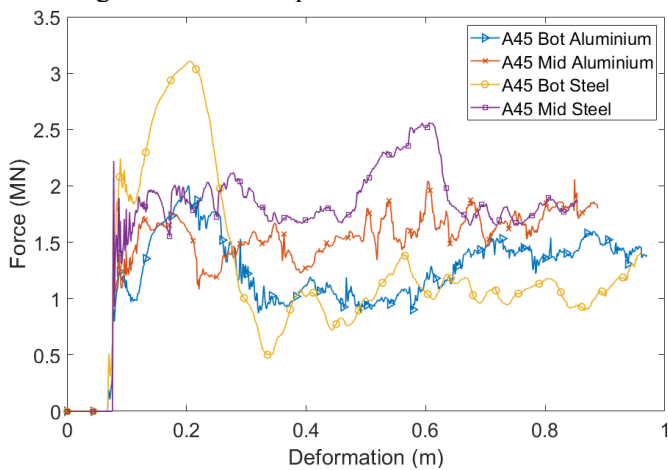
Figure 10. Force-displacement curves for A45.
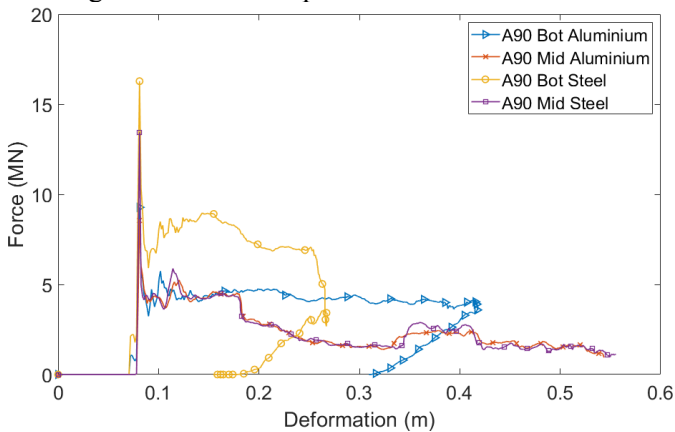
Figure 11. Force-displacement curves for A90.

Table 4. Girder deformations (m)

Case	Steel Girder	Aluminium Girder
A00_Bot	0.10	0.91
A45_Bot	0.12	0.64
A90_Bot	0.14	0.42

4.2 *Structural deformation and damage*

The vertical impact location causes large variations in the stress distribution in the bridge girder and deformation of the containers. In all cases, the shipping container impact leads to plastic deformation in the aluminium girder. Localized fracture occurs in the girder vertical plates and/or stiffeners on the inside of the girder panel. These stiffeners also seem to take high stress due to bending, especially from the bottom impacts. This because the density of the container floor is increased to account for the weight of the cargo inside the container. The floor beams contacts directly crushed against the girder side panel and induce larger contact force in the impact region for all angles. For middle impact cases, the forces are transferred onto the diaphragms, which also fail locally in most cases as shown in Figures 13-15.

Figure 12. Deformed shipping containers when impacting aluminium gider. (a) A00_Bot, (b) A00_mid, (c) A45_Bot, (d) A45_Mid, (e) A90_bot, and (f) A90_mid.
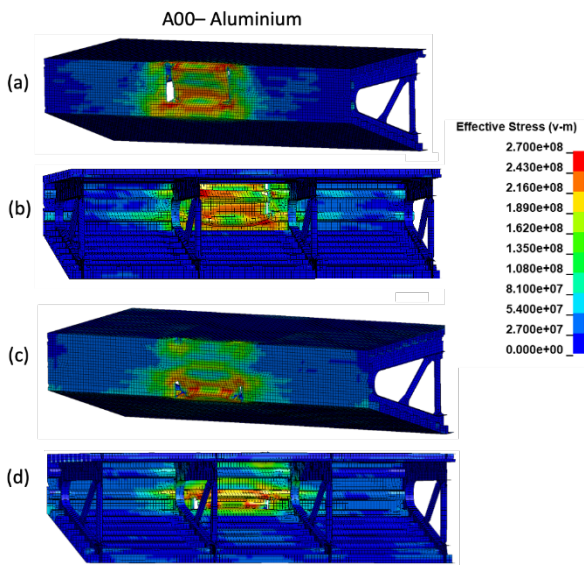
Figure 13. Stress contours of the aluminium bridge girder. (a) A00_Bot, (b) A00_Bot inside girder, (c) A00_Mid, and (d) A00_Mid inside girder.
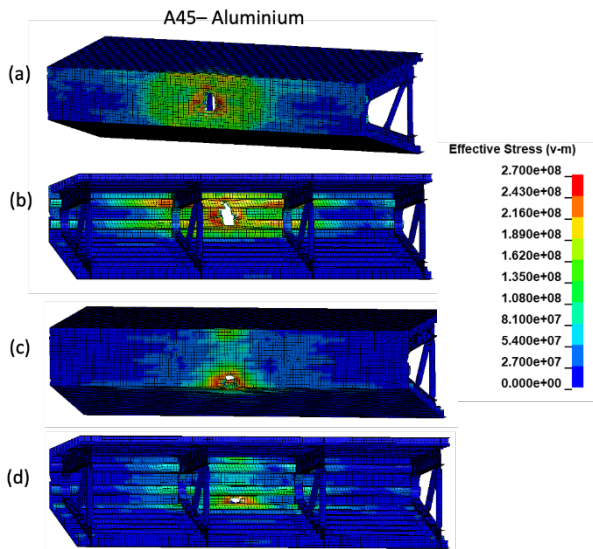
Figure 14. Stress contours of the aluminium bridge girder. (a) A45_Bot, (b) A45_Bot inside girder, (c) A45_Mid, and (d) A45_Mid inside girder.
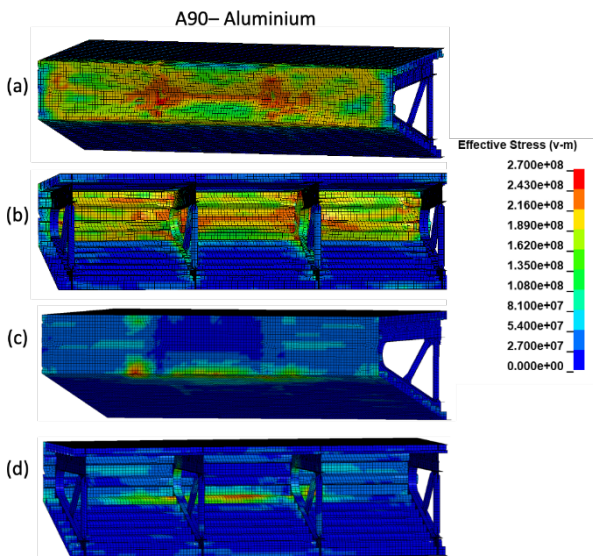
Figure 15. Stress contours of the aluminium bridge girder. (a) A90_Bot, (b) A90_Bot inside girder, (c) A90_Mid, and (d) A90_Mid inside girder.

When impacting with the steel bridge girder, high stress still occurs at the impact zone in the bridge girder. The steel bridge girder shows the same deformation pattern as the aluminium bridge girder. However, the area and severity of the deformed region are much smaller compared with the aluminium bridge girder. Moreover, no fracture was observed in the steel bridge girder. This is because the high strength steel used in the steel bridge girder has much higher yield stress than the aluminium material. The stress contour of the steel bridge girder in various impact scenarios is shown in Figures 16-18.
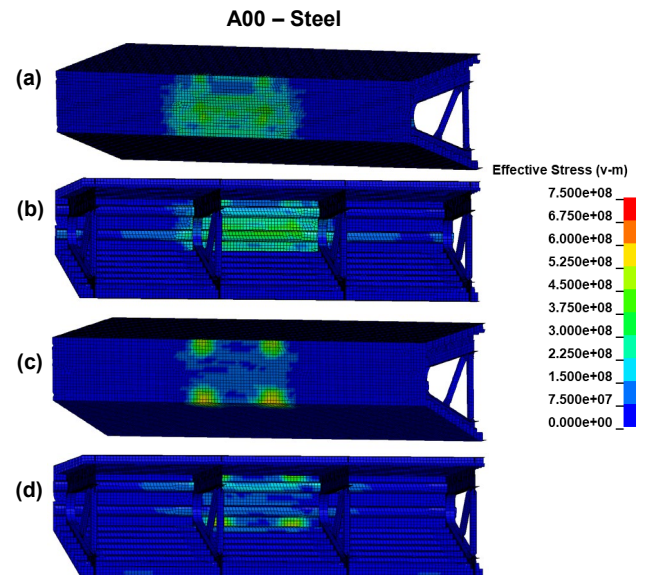
Figure 16. Stress contours of the steel bridge girder. (a) A00_Bot, (b) A00_Bot inside girder, (c) A00_Mid, and (d) A00_Mid inside girder.
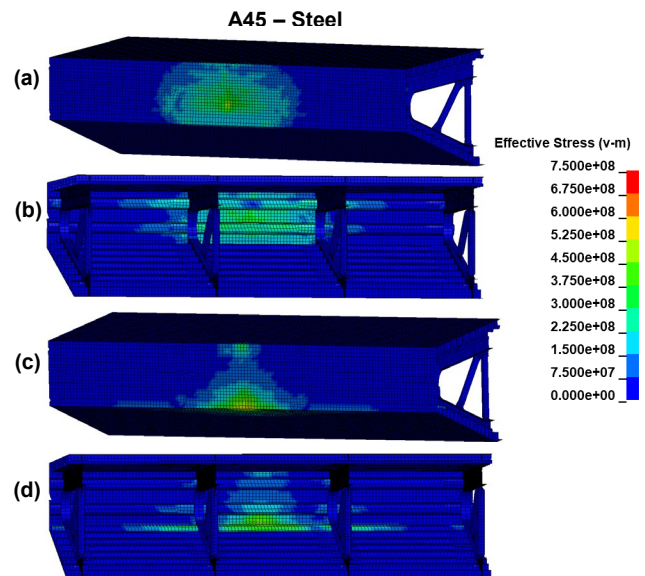
Figure 17. Stress contours of the steel bridge girder. (a) A45_Bot, (b) A45_Bot inside girder, (c) A45_Mid, and (d) A45_Mid inside girder.

A90 – Steel

(a)

(b)

(c)

(d)

Effective Stress (v-m)

7.500e+08
6.750e+08
6.000e+08
5.250e+08
4.500e+08
3.750e+08
3.000e+08
2.250e+08
1.500e+08
7.500e+07
0.000e+00
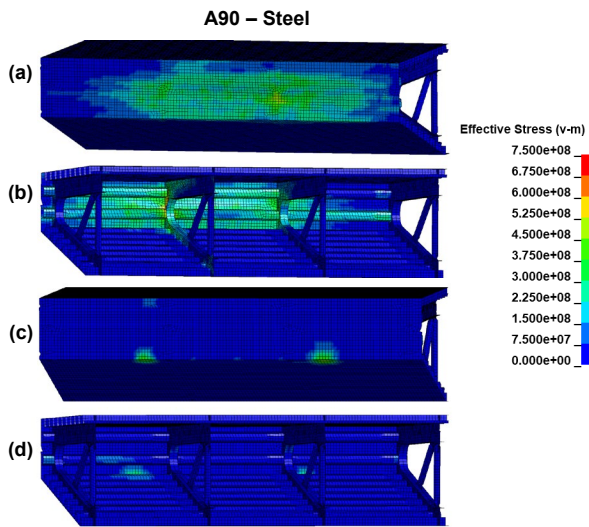
Figure 18. Stress contours of the steel bridge girder. (a) A90_Bot, (b) A90_Bot inside girder, (c) A90_Mid, and (d) A90_Mid inside girder.

4.3 *Energy dissipation*

The energy dissipations of the shipping container in all collision scenarios are listed in Table 6. In all cases, the initial kinetic energy of the impacting container is 1.72 MJ. The container dissipates 29%-81% of the total impact energy when impacting with the aluminium bridge girder. The container has a low energy dissipation ratio for 45- and 90-degree bottom impact cases. For the 45-degree bottom impact case, the container corner fitting penetrates the girder side panel and results in large damage to the bridge girder. Similarly, the container induces plastic deformation over a large region in the 90-degree bottom impact case. For impact with the steel bridge girder, the shipping container can absorb around 80% of the total energy in several cases. For other cases, the container dissipates more than 50% of the total impact energy in all cases except for the 45-degree bottom case where 47% of the total energy is absorbed by the container. It is therefore reasonable to assume a rigid girder when performing preliminary design of steel bridge girders against shipping container impact.

Table 6. Shipping container energy.

	Case	Initial Kinetic Energy(MJ)	Internal energy (MJ)	Ratio
Aluminium	A00_Bot	1.72	0.98	57%
	A00_Mid	1.72	0.95	55%
	A45_Bot	1.72	0.50	29%
	A45_Mid	1.72	0.71	41%
	A90_Bot	1.72	0.55	32%
	A90_Mid	1.72	1.31	76%
Steel	A00_Bot	1.72	1.40	81%
	A00_Mid	1.72	1.38	80%
	A45_Bot	1.72	0.80	47%
	A45_Mid	1.72	1.02	59%
	A90_Bot	1.72	1.09	63%
	A90_Mid	1.72	1.35	78%

5 DISCUSSIONS

The impact force is highly dependent on the container strength and impact location. The impact force is generally higher when impacting against the steel bridge girder than colling with the aluminium bridge girder. However, the response varies depending on the impact scenario for the aluminium bridge girder. Middle impact cases result in a relatively smaller damage in the bridge girder. This attributes to the support of the diaphragm and consequently a larger contact area. Bottom impact cases lead to larger damage in the bridge girders as the container bottom structure crushes on the girder side panel. The bottom impacts indicate that when forces are directly transferred, the aluminium girder deforms more significantly, which is expected due to the lower elastic modulus and yield stress.

Previous study indicates that it is feasible to meet the relevant design criteria for the bridge, including global stability, local stability, fatigue, ultimate global stress levels, and serviceability deflections. However, the results from this study raise questions about the accident limit state design. Aluminium girders might have to be used for suspension bridges where the water to bridge deck height eliminates the possibility of any ship collision. Investigation of thicker plates or different designs to optimize for the local damage has not been done. In addition, it should also be noted that this force level considers only one container on the ship deck. For example, with a ship width of 25 m, it is easy to parallelly place six rows of containers on the ship deck. This amounts the maximum impact force to around 30 MN, which may be critical for bridge girders. Such a high impact force should therefore not be ignored during the design of bridge superstructures where container ships are operating and are at the same height as the bridge deck. In the case of the E39 Bjørnafjorden crossing, the floating part of the bridge will have a low water clearance, such that drifting ships in this area will not stay clear of the bridge girder or pontoons. In the simulation, the containers were given an initial velocity and the simulation results showed rapid deceleration and, in some cases, rebound at the end. Large inertia of a container ship would cause a slower deceleration than obtained in this study.

In the simulations, the container is empty inside, but the loading on the floor beams is considered. In the case of rigid cargo, such as cars, engines, building materials, raw rocks etc., the contact force will likely increase. In a design situation, considering an impact with shipping container impact with or without deckhouse impact will likely generate lower impact force compared to a bow collision where the entire mass of the ship with cargo is considered.

Further work should investigate global bridge response under shipping container impacts. Investigations with freight-filled containers for impacts with a constant or slow deceleration of the velocity is also recommended. According to NPRA handbook N400 (2019), it is stated that local collapse is acceptable, provided the global stability can be maintained to prevent total collapse. For the bridge girder, this means that the bridge girder can have some local damage with reduced strength as long as the bridge can sustain a post-impact phase according to NS-EN 1991-1-7.

6 CONCLUSIONS

Numerical simulations of loaded shipping containers impacting an aluminium bridge girder with various angles have been performed.

1. A comparison between impact with and without considering strain rate of the aluminium material has been performed. The comparison showed that the strain rate has a minor effect for 6005-T6 Aluminium in container-girder collision simulations.
2. The results show reduced contact compared to a steel girder due to increased deformation and initiation of fracture in the aluminium girder, which leads to higher energy dissipation. Stress development in the aluminium girder is large, and local failure is observed for all cases in various degree.
3. In the cases where the middle of the shipping container impacts and deformations are large, the material type seems to play a minor role. This is because the middle impact cases involve a larger area in the girder which redistribute the impact force.
4. The shipping containers generally dissipate the majority of the kinetic energy when impact by the steel bridge girder. The energy dissipation varies when impacting with the aluminium girder due to the fracture in the girder.

REFERENCES

Standard, B. (2007). "Eurocode 9-Design of aluminium structures."

Liu, B., et al. (2015). "Shear and tensile failure of thin aluminium plates struck by cylindrical and spherical indenters." Ships and Offshore Structures **10**(1): 45-58.

Mohotti, D., et al. (2013). "Out-of-plane impact resistance of aluminium plates subjected to low velocity impacts." Materials & Design **50**: 413-426.

NPRA (2012). "K12 - Ship Impact, Bridge Girder Bjørnafjorden crossing ".

NPRA (2020). Langenuen Suspension Bridge Aluminium Bridge Girder Alternative: 102.

Sha, Y., et al. (2019). "Local and Global Responses of a Floating Bridge Under Ship–Girder Collisions." Journal of Offshore Mechanics and Arctic Engineering **141**(3).

Sha, Y., et al. (2019). "Design of steel bridge girders against ship forecastle collisions." Engineering Structures **196**: 109277.

Sha, Y., et al. (2020). Simulation of Shipping Container Impact with Bridge Girders. The 30th International Ocean and Polar Engineering Conference, International Society of Offshore and Polar Engineers.

Villavicencio, R., et al. (2012). "Numerical simulation of transversely impacted, clamped circular aluminium plates." Ships and Offshore Structures **7**(1): 31-45.

Zhu, Y., et al. (2020). "Dynamic Mechanical Behavior and Constitutive Models of S890 High-Strength Steel at Intermediate and High Strain Rates." Journal of Materials Engineering and Performance **29**(10): 6727-6739.

Appendix B

Calculation of cross sectional parameters for bridge girders

Cable Stayed Bridge	Axis 1E-3					
	E	206000000	kPa	1000(N/m2)		
		2,06E+11	Pa	N/m2		
	A		mm2			
		1,797	m2			
Axial Stiffness	E*A	3,70182E+11	N			
		370182000	kN			
	Ixx	123,34	m4	Iyy	3,64	m4
	E*Ixx	2,5408E+13	N*m2	E*Iyy	7,4984E+11	N*m2
Bending stiffness		**25408040000**	kN*m2		**749840000**	kN*m2
	G	81000000	kPa			
		81000000000	Pa	(N/m2)		
	J		mm4			
		9,663	m4			
Torsional stiffness	G*J	7,82703E+11	N*m2			
		782703000	kN*m2			

Concrete Girder C1	Axis 1A-1E					
	E	36283	Mpa	1000(N/m2)		
		36283000	Pa	N/m2		
	A		mm2			
		27,951	m2			
Axial Stiffness	E*A	1014146133	N			
		1014146,133	kN			
	Ixx	2138	m4	Iyy	40,5	m4
	E*Ixx	77573054000	N*m2	E*Iyy	1469461500	N*m2
Bending stiffness		**77573054**	kN*m2		**1469461,5**	kN*m2
	G	15117916,67	kPa			
		15117916667	Pa	(N/m2)		
	J		mm4			
		135,4	m4			
Torsional stiffness	G*J	2,04697E+12	N*m2			
		2046965917	kN*m2			

High Bridge	K12_S1_01					
	E	206000000	kPa	1000(N/m2)		
		2,06E+11	Pa	N/m2		
	A		mm2			
		1,8829	m2			
Axial Stiffness	E*A	3,87877E+11	N			
		387877400	kN			
	Ixx	121,83	m4	Iyy	3,785	m4
	E*Ixx	2,5097E+13	N*m2	E*Iyy	7,7971E+11	N*m2
Bending stiffness		**25096980000**	kN*m2		**779710000**	kN*m2

	G	81000000	kPa	
		81000000000	Pa	(N/m2)
	J		mm4	
		12,01	m4	
Torsional stiffness	G*J	9,7281E+11	N*m2	
		972810000	kN*m2	

Low Bridge

	E	206000000	kPa	1000(N/m2)		
		2,06E+11	Pa	N/m2		
	A		mm2			
		1,2699	m2			
Axial Stiffness	E*A	2,61599E+11	N			
		261599400	kN			
	Ixx	84,698	m4	Iyy	2,569	m4
	E*Ixx	1,74478E+13	N*m2	E*Iyy	5,29214E+11	N*m2
Bending stiffness		**17447788000**	kN*m2		**529214000**	kN*m2
	G	81000000	kPa			
		81000000000	Pa	(N/m2)		
	J		mm4			
		8,6111	m4			
Torsional stiffness	G*J	6,97499E+11	N*m2			
		697499100	kN*m2			

Kxxx H1

	E	206000000	kPa	1000(N/m2)		
		2,06E+11	Pa	N/m2		
	A		mm2			
		1,346	m2			
Axial Stiffness	E*A	2,77276E+11	N			
		277276000	kN			
	Ixx	97,879997	m4	Iyy	2,592	m4
	E*Ixx	2,01633E+13	N*m2	E*Iyy	5,33952E+11	N*m2
Bending stiffness		**20163279382**	kN*m2		**533952000**	kN*m2
	G	81000000	kPa			
		81000000000	Pa	(N/m2)		
	J		mm4			
		6,3870001	m4			
Torsional stiffness	G*J	5,17347E+11	N*m2			
		517347008,1	kN*m2			

Kxxx H2

	E	206000000	kPa	1000(N/m2)		
		2,06E+11	Pa	N/m2		
	A		mm2			
		1,753	m2			
Axial Stiffness	E*A	3,61118E+11	N			
		361118000	kN			
	Ixx	126,7	m4	Iyy	3,51	m4

	E*Ixx	2,61002E+13 N*m2		E*Iyy	7,2306E+11 N*m2
Bending stiffness		**26100200000** kN*m2			**723060000** kN*m2

	G	81000000 kPa		
		81000000000 Pa	(N/m2)	
	J	mm4		
		9,69 m4		
Torsional stiffness	G*J	7,8489E+11 N*m2		
		784890000 kN*m2		

K12 H1 02

	E	206000000 kPa	1000(N/m2)
		2,06E+11 Pa	N/m2
	A	mm2	
		1,297 m2	
Axial Stiffness	E*A	2,67182E+11 N	
		267182000 kN	

	Ixx	89,53 m4		Iyy	2,53 m4
	E*Ixx	1,84432E+13 N*m2		E*Iyy	5,2118E+11 N*m2
Bending stiffness		**18443180000** kN*m2			**521180000** kN*m2

	G	81000000 kPa		
		81000000000 Pa	(N/m2)	
	J	mm4		
		6,69 m4		
Torsional stiffness	G*J	5,4189E+11 N*m2		
		541890000 kN*m2		

K12 T1 00

	E	206000000 kPa	1000(N/m2)
		2,06E+11 Pa	N/m2
	A	mm2	
		1,521 m2	
Axial Stiffness	E*A	3,13326E+11 N	
		313326000 kN	

	Ixx	98,583 m4		Iyy	3,311 m4
	E*Ixx	2,03081E+13 N*m2		E*Iyy	6,82066E+11 N*m2
Bending stiffness		**20308098000** kN*m2			**682066000** kN*m2

	G	81000000 kPa		
		81000000000 Pa	(N/m2)	
	J	mm4		
		10,105 m4		
Torsional stiffness	G*J	8,18505E+11 N*m2		
		818505000 kN*m2		

Kxx B1

	E	206000000 kPa	1000(N/m2)
		2,06E+11 Pa	N/m2
	A	mm2	
		2,09 m2	
Axial Stiffness	E*A	4,3054E+11 N	
		430540000 kN	

	Ixx	314 m4		Iyy	5,32 m4
	E*Ixx	6,4684E+13 N*m2		E*Iyy	1,09592E+12 N*m2
Bending stiffness		**64684000000** kN*m2			**1095920000** kN*m2
	G	81000000 kPa			
		81000000000 Pa	(N/m2)		
	J	mm4			
		18,2 m4			
Torsional stiffness	G*J	1,4742E+12 N*m2			
		1474200000 kN*m2			

Kxx B2

	E	206000000 kPa	1000(N/m2)		
		2,06E+11 Pa	N/m2		
	A	mm2			
		2,28 m2			
Axial Stiffness	E*A	4,6968E+11 N			
		469680000 kN			
	Ixx	226 m4		Iyy	5,92 m4
	E*Ixx	4,6556E+13 N*m2		E*Iyy	1,21952E+12 N*m2
Bending stiffness		**46556000000** kN*m2			**1219520000** kN*m2
	G	81000000 kPa			
		81000000000 Pa	(N/m2)		
	J	mm4			
		20 m4			
Torsional stiffness	G*J	1,62E+12 N*m2			
		1620000000 kN*m2			

Kxx B3

	E	206000000 kPa	1000(N/m2)		
		2,06E+11 Pa	N/m2		
	A	mm2			
		2,86 m2			
Axial Stiffness	E*A	5,8916E+11 N			
		589160000 kN			
	Ixx	314 m4		Iyy	7,7 m4
	E*Ixx	6,4684E+13 N*m2		E*Iyy	1,5862E+12 N*m2
Bending stiffness		**64684000000** kN*m2			**1586200000** kN*m2
	G	81000000 kPa			
		81000000000 Pa	(N/m2)		
	J	mm4			
		24,3 m4			
Torsional stiffness	G*J	1,9683E+12 N*m2			
		1968300000 kN*m2			

Kxx B4

	E	206000000 kPa	1000(N/m2)		
		2,06E+11 Pa	N/m2		
	A	mm2			
		3,34 m2			
Axial Stiffness	E*A	6,8804E+11 N			
		688040000 kN			

	Ixx	423 m4	Iyy	9,74 m4

	E*Ixx	8,7138E+13 N*m2	E*Iyy	2,00644E+12 N*m2
Bending stiffness		**87138000000** kN*m2		**2006440000** kN*m2

	G	81000000 kPa		
		81000000000 Pa	(N/m2)	
	J	mm4		
		28 m4		
Torsional stiffness	G*J	2,268E+12 N*m2		
		2268000000 kN*m2		

Kxx B4

	E	206000000 kPa	1000(N/m2)	
		2,06E+11 Pa	N/m2	
	A	mm2		
		3,48 m2		
Axial Stiffness	E*A	7,1688E+11 N		
		716880000 kN		

	Ixx	461 m4	Iyy	10,07 m4

	E*Ixx	9,4966E+13 N*m2	E*Iyy	2,07442E+12 N*m2
Bending stiffness		**94966000000** kN*m2		**2074420000** kN*m2

	G	81000000 kPa		
		81000000000 Pa	(N/m2)	
	J	mm4		
		29,7 m4		
Torsional stiffness	G*J	2,4057E+12 N*m2		
		2405700000 kN*m2		

Table 2-1 Key sectional properties for K12_07.

	M	Iy	Iz	J	Ax	Ly	Lz	VCGt
	[tonne/m]	[m^4]	[m^4]	[m^4]	[m^2]	[m]	[m]	[m]
K12_S1_02	19	3.668	110.4	11.349	1.779	27	4	1.989
K12_S2_00	19	3.785	121.83	12.01	1.8829	27	4	2.041
K12_T1_00	19	3.311	98.583	10.105	1.521	27	4	1.878
K12_F2_00	19	2.781	89.597	9.4228	1.331	27	4	1.763
K12_F1_05	19	2.569	84.698	8.6111	1.2699	27	4	1.682
K12_H1_02	19	2.534	89.531	6.629	1.297	27	3.5	1.463
K12_H2_02	19	3.64	123.34	9.663	1.797	27	3.5	1.633
C1	79.1	40.5	2138	135.4	27.951	29	3.5	1.463
Kxx_B1	19	5.32	170	18.2	2.09	27	4	1.989
Kxx_B2	20.52	5.95	226	20	2.28	27	4	1.989
Kxx_B3	25.16	7.7	314	24.3	2.86	27	4	1.989
Kxx_B4	29	9.74	423	28.5	3.34	27	4	1.989
Kxx_B5	30.12	10.06	461	29.7	3.48	27	4	1.989

More details on the concept development and choices are found in [3, 8].
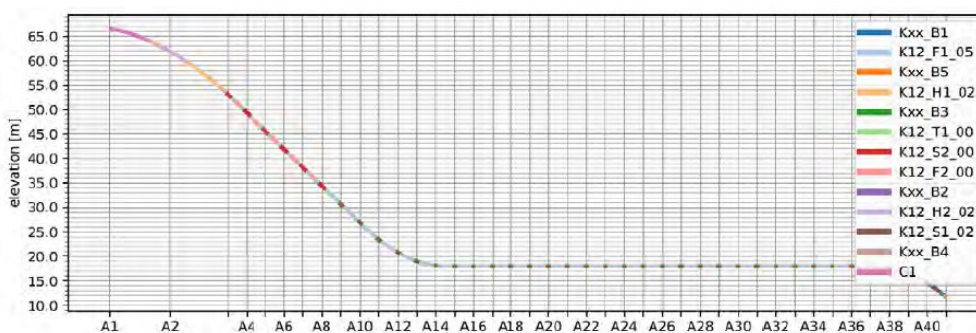
Calculation of cross-sectional parameters for columns used in Global Orcaflex Model:

Steel column High

E	210000000	kPa	1000(N/m2)
	2,1E+11	Pa	N/m2
A	2018240	mm2	
	2,01824	m2	
Axial Stiffness E*A	4,2383E+11	N	
	423830400	**kN**	
Ixxyy	1,15225E+13	mm4	
	11,52248832	m4	
Bending stiffn E*I	2,41972E+12	N*m2	
	2419722547	**kN*m2**	
G	81000000	kPa	
	81000000000	Pa	(N/m2)
J	2,3045E+13	mm4	(simplified as 80mm thick rhs)
	23,04497664	m4	
Torsional stiffi G*J	1,86664E+12	N*m2	
	1866643108	**kN*m2**	
p	7850	kg/m3	
	7,85	ton/m3	
Weight/m p*A	15,843184	ton/m	

Concrete Column

E	210000000	kPa			
	2,98E+10	Pa			
A		mm2			
	12	m2			
Axial Stiffness E*A	3,5712E+11	N			
	357120000	**kN**			
Ixx		mm4	Iyy		mm4
	64	m4		2,25	m4
Bending stiffn E*I	1,90E+12	N*m2	E*I	6,70E+10	N*m2
	1,90E+09	**kN*m2**		**66960000**	**kN*m2**
G		kPa			
	21000000000	Pa			
J		mm4			
	7,9949999	m4			
Torsional stiffi G*J	1,67895E+11	N*m2			
	167894997,9	**kN*m2**	1000(N/m2)		
			N/m2		

	p	2650.3999	kg/m3
		2,65	ton/m3

Weight/m	p*A		31,8 ton/m

Steel column Low

	E	210000000 kPa	
		2,1E+11 Pa	(N/m2)
	A	mm2	(simplified as 80mm thick rhs)
		0,8 m2	

Axial Stiffness E*A	1,68E+11 N
	168000000 kN

	Ixxyy	mm4
		4 m4

Bending stiffn E*I	8,4E+11 N*m2
	840000000 kN*m2

	G	81000000 kPa
		81000000000 Pa
	J	mm4
		6,8 m4

Torsional stiff G*J	5,508E+11 N*m2
	550800000 kN*m2

p	7850 kg/m3
	7,85 ton/m3

Calculation of cross sectional parameters for cable - tower

	E	36283	kPa	1000(N/m2)
		36283000	Pa	N/m2
	A	35200000	mm2	
		35,2	m2	
Axial Stiffne	E*A	1,28E+09	N	
		1277162	kN	

	Ixx	2,98E+14		Iyy	6,01E+14	
	Ixx	2,98E+02	m4	Iyy	6,01E+02	m4

	E*Ixx	1,08E+10	N*m2	E*Iyy	2,18E+10	N*m2
Bending stiffness		**10812334**	kN*m2		**21806083**	kN*m2

	G	15117917	kPa	
		1,51E+10	Pa	(N/m2)
	J		mm4	
			m4	
Torsional st	G*J	0	N*m2	
		0	kN*m2	
				Assumed 2e9

p		2500	kg/m3
p*Ac			
Weight		88000	kg/m
		88	ton/m

Tower legs at cross beam interface

Title	309 Z=52 x*y=8.82*4.28	
Ac	3.52E+07	mm2
Ix	2.98E+14	mm4
Iy	6.01E+14	mm4
As	5.84E+05	mm2
rho	1.7 %	
	2ø32c200	two layers
Elevation	52	m

Project	Bjørnafjorden phase 5
Date	25.06.2019
By	Petter Buckholm
Models	K12_06 (ULS/ALS)
	C.S. a,b,c, all wind.dir.
	(results dated 24.06.2019)
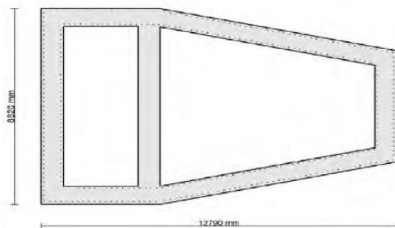
Calculation of pontoon parameters

Moment of inertia tensor

Conventional Pontoon		
Ixx	38750	ton*m2
Iyy	439270	ton*m2
Izz	470270	ton*m2

Moored Pontoon	
Ixx	97734,375
Iyy	995674,375
Izz	1054315
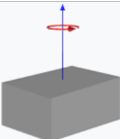
Pontoon parameters			
Conventional pontoon		Moored Pontoon	
m (tonne)	1860	m (tonne)=	4170
height (m)	15	height (m)	15
depth (m)	5	depth (m)	7,5
width(m)	53	width(m)	53

Added Mass based on A3

Conventional Pontoon	
Rel. Dif. Betwe	0,68888889
Heave	7231,08756
Surge	3405,68756
Sway	1870,15422

Moored Pontoon	
Rel. Dif. Betwe	1,54444444
Heave	16211,6318
Surge	7635,33178
Sway	4192,76511

Solid cuboid of width *w*, height *h*, depth *d*, and mass *m*		$I = \begin{bmatrix} \frac{1}{12}m(h^2+d^2) & 0 & 0 \\ 0 & \frac{1}{12}m(w^2+d^2) & 0 \\ 0 & 0 & \frac{1}{12}m(w^2+h^2) \end{bmatrix}$